EFFECTS OF PHASE-ANGLE BETWEEN THE FRETTING AND THE BULK FATIGUE LOADS ON THE LIFE OF THE AL7050 T7451 AND ASTM 743 CA6NM

UNIVERSIDADE DE BRASILIA

FACULDADE DE TECNOLOGIA

DEPARTAMENTO DE ENGENHARIA MECANICA

UNIVERSIDADE DE BRASILIA

Faculdade de Tecnologia

Departamento de Engenharia Mecânica

UNIVERSIDADE DE BRASÍLIA
FACULDADE DE TECNOLOGIA
DEPARTAMENTO DE ENGENHARIA MECÂNICA

EFFECTS OF PHASE ANGLE BETWEEN THE FRETTING LOAD AND THE BULK LOAD ON THE LIFE OF THE AL7050 T7451 AND ASTM 743 CA6NM

AUTOR:

THOMAS GAILLIEGUE

ORIENTADOR: THIAGO DOCA
COORIENTADOR: JOSÉ ALEXANDER ARAÚJO

TESE DE DOUTORADO EM CIÊNCIAS MECÂNICAS

PUBLICAÇÃO:

BRASÍLIA-DF: SETEMBRO – 2018

UNIVERSITY OF BRASÍLIA
FACULTY OF TECHNOLOGY
DEPARTAMENT OF MECHANICAL ENGINEERING

EFFECTS OF PHASE ANGLE BETWEEN THE FRETTING LOAD AND THE BULK LOAD ON THE LIFE OF THE AL7050 T7451 AND ASTM 743 CA6NM

THOMAS GAILLIEGUE

A thesis submitted to University of Brasília in partial fulfilment of the requirements of the degree of Doctor in mechanical engineering.

APPROVED BY:

_____
Prof. Dr. Thiago Doca. (Presidente da banca) (UnB) (Orientador)

_____
Prof. Dr. Luciana Sgarbi Rossino (FATEC Sorocaba) (Examinador externo)

_____
Prof. Dr. Luis Augusto Veloso (UnB) (Examinador externo)

_____
Prof. Dr.Jorge Luiz Almeida Ferreira (UnB) (Examinador interno)

Brasília/DF, 10 de Setembro de 2018

FICHA CATALOGRÁFICA

THOMAS GAILLIEGUE

EFFECTS OF PHASE ANGLE BETWEEN THE FRETTING LOAD AND THE BULK LOAD
ON THE LIFE OF THE AL7050 T7451 AND ASTM 743 CA6NM
xiii, 111 p., 210 x 297 mm (ENM/FT/UnB, Doutor, Ciências Mecânicas, 2018).

Dissertação de Doutorado – Universidade de Brasília. Faculdade de Tecnologia.

Departamento de Engenharia Mecânica.

1. Fadiga por *fretting*	2. Ângulo de fase
3. Estimativa de vida	4. Abordagem de plano crítico
5. Teoria da distância crítica	
I. ENM/FT/UnB	II. ENM.DT-55/17

CESSÃO DE DIREITOS

AUTOR: Thomas Gailliegue.

TÍTULO: Effects of phase angle between the fretting and the bulk load on the life of the
Al7050 T7451 and ASTM 743 CA6NM - [Distrito Federal] 2018.

GRAU: Doutor   ANO: 2018

_____
Thomas Gailliegue
thomas.gailliegue@hotmail.fr

Acknowledgments

Firstly, I would like to express my sincerest gratitude to José Alexander Araújo and Alix de Pannemaecker for the opportunity to do this PhD in Brazil.

I also would like to thank the professors Jorge Luiz Almeida Ferreira and José Alexander Araújo, as well as Remy Kalombo Badibanga, for helping me to deal with the Brazilian bureaucracy at my arrival.

I gratefully acknowledge the professors Thiago Doca and José Alexander Araújo for their supervision and assistance throughout the study. I also would like to thank Marcus Vinícius Costa Sá and the professor Fabio Castro for additional contributions to the work.

My gratitude to Marcos Silva and Miguel Garcia for their essential help with material machining and laboratory equipment.

A thought for technical or moral support of my colleagues Remy, Mauricio, Barbara, Anthony, Vitor, Gabriel and José.

Very special thanks to my parents Sylvain and Laurence for being there since the beginning and for their unconditional support and love whatever is the distance between us. I am also grateful for the presence of my sister Lea and my brothers Thibault and Etienne in my life, and very proud of the persons they are.

A great thank to Gley Barbosa. Her attention, kindness and patience during redaction were very welcome. May we enjoy life and overcome obstacles together.

I also would like to take this opportunity to thank; for the great experience and shared time; Fabien, Bruno, Julien, Denis, Yannick, Gaetan, Romain, Hugo, Ben, Flo, Mickael, Migayrou, Florence, Hammid, Bari, Iqbal, Jean-François, Alix, Dany, Sofia, Marcelo and Jeferson.

Abstract

This work presents a study of the fretting fatigue process when introducing a phase angle between the fretting and the bulk load. The objective is to investigate the effect of such phase angle on the fatigue life and fracture mechanics of two alloys: the 7050 T7451 aluminum alloy and the ASTM 743 CA6NM stainless steel. Experiments and numerical analysis are performed in four loading conditions: in phase (Φ=0°), as reference, and three phase angles (Φ=45°, Φ=90° and Φ=135°).

Experimental tests were conducted at the material testing laboratory of the Department of Mechanical Engineering - University of Brasilia, using a bi-axial system with independent control of each load. The problem is modeled using the commercial Finite Element package Abaqus© CAE. Simulations were carried-out to calculate stress fields produced by the different loading configurations. Life estimations were attempted applying three different stress based multiaxial criteria (Smith-Watson-Topper, Fatemi-Socie and the Modified Wöhler Curve Method) at a critical point located at the edge of the contact and under the surface. The distance from the surface has been evaluated with two formulations, the first one was based on static and dynamic material parameters and the second one based on experimental and numerical results obtained on V-notched specimens.

It has been shown in this study that the phase angle parameter strongly influences the fatigue life. A phase angle of Φ=90° can double the fatigue life of materials, while delays of 45° and 135° reduce specimen's duration. Nevertheless, unexpected high lives were obtained for the condition Φ=45°, while testing Al7050. Stresses and failure analyzes also revealed that the phase angle plays an essential role in the crack nucleation location. Indeed, cracks initiate always at one edge of the contact for Φ=0° and Φ=45°, and at the opposite one for Φ=135°. Concerning the phase angle Φ=90°, it is impossible to predict in advance at which edge the failure occurs. Furthermore, two methods giving accurate life estimations were identified. It is possible to predict the life of such loading conditions applying the Fatemi-Socie criterion at a distance calibrated with experimental/numerical results obtained on V-notched specimens or applying the Modified Wöhler Curve Method at a distance calculated with the static and dynamic material parameters.

Contents

List of figures

List of tables

Nomenclature

Latin

A — Composite compliance

A_{FS}, A_{SWT}, A_{σ}, A_{τ}, b_{FS}, b_{SWT}, b_{σ}, b_{τ} — Material parameter to calibrate power law

a — Semi size of the contact zone — [mm]

a_i — Semi halves of rectangular Hull

B — Bulk load or Fatigue load for model — [kN]

C — Cauchy singular equation

c — Semi size of the slip zone at one edge of the stick zone — [mm]

c' — Reversed slip zone — [mm]

c_{α} — Crack angle — [°]

c_w — Propagation length — [mm]

E — Young's modulus — [GPa]

E_{eq} — Equivalent Young's modulus in contact mechanic — [GPa]

e — Offset induced by fatigue load — [mm]

e' — Reversed offset — [mm]

f — Friction coefficient

$g(x)$ — Relative displacement in x

G — Modulus of rigidity — [GPa]

$h(x)$ — Relative displacement in y

K_c — Material fracture toughness — [MPa.m$^{1/2}$]

L — Critical distance — [mm]

L_{σ} — Critical distance obtained with tension-compression loadings — [mm]

L_{τ} — Critical distance obtained with torsional loadings — [mm]

L_S — Critical distance calculated for static case — [mm]

L_{N0} — Critical distance calculated for the fatigue limit — [mm]

L_{min} — Critical distance obtained for the minimal value of ΔK_{th} — [mm]

L_{max}	Critical distance obtained for the maximalvalue of ΔK_{th}	[mm]
$\boldsymbol{n}$	Normal vector	
N	Number of cycles to failure	
N_a	Number of cycles appropriate for the Modified Wohler Curve diagram	
N_{exp}	Experimental number of cycles to failure	
N_{est}	Life estimation	
$N_{estMWMC}$	Life estimation with Modified Wohler Curve method	
N_{estSWT}	Life estimation with Smith-Watson-Tooper criterion	
N_{estFS}	Life estimation with Fatemi-Socie criterion	
P	Normal pressure	[kN]
P_0	Peak pressure	[MPa]
$p(x)$	Normal pressure distribution	[MPa]
Q	Fretting load	[kN]
$q(x)$	Shear traction distribution	[MPa]
$q'(x)$	Perturbation of the shear traction distribution	[MPa]
$q''(x)$	corrective term for the shear traction distribution	[MPa]
R	Radius of the cylindrical part	[mm]
r	radial coordinate (polar coordinate)	
$\boldsymbol{t}$	Stress vector	
$\boldsymbol{T}$	Stress tensor	

Greek

β	Dundur's parameter	
Δ	Material plan	
ΔK_{th}	Stress factor intensity threshold	[MPa.m$^{1/2}$]
ε_{rr} , $\varepsilon_{\theta\theta}$	Displacement tensor components	
δ	Relative displacement	
θ	angle coordinate (polar coordinate)	[°]
ѳ	Orientation angle of a material plane	[°]
κ_t	Inverse slope for MWC diagram	

v	Poisson's coefficient	
ξ	Integration variable	
ρ	Stress ratio	
σ	Normal component of stress vector	
σ_{xx}	Normal stress in x,	[MPa]
σ_{xx}^{n}	normal component calculated for normal load	[MPa]
σ_{xx}^{t}	Normal component calculated for tangential load	[MPa]
σ_B	Normal component calculated for bulk load	[MPa]
σ_{yy}	Direct component of the stress tensor in the y direction	[MPa]
σ_{zz}	Direct component of the stress tensor in the z direction	[MPa]
σ_{nmax}	Maximum normal stress acting during one cycle,	[MPa]
σ_{namp}	Normal stress amplitude of one loading cycle,	[MPa]
σ_{eff}	Effective stress,	[MPa]
σ_{-1}	Fatigue limit for fully reversed uniaxial loading	[MPa]
τ	Shear component of stress vector	
τ_{xy}	Shear stress of the stress tensor	[MPa]
τ_a	Shear stress amplitude occurring during one cycle	[MPa]
$\tau_{a,ref}$	Shear stress amplitude reference for MWCM	[MPa]
τ_{amax}	Maximum shear stress amplitude in between every material plane	[MPa]
τ_{-1}	Fatigue limit for fully reversed torsional loading	[MPa]
Φ	Phase angle	[°]
φ	Rotative angle used for MRH	[°]
ϕ	Penetration angle of a material plane	[°]
ψ	Potential function	
ω_τ	weight of torsional loading for the critical distance calibration	
ω_σ	weight of uniaxial loading for the critical distance calibration	

Acronyms

MRH   Maximum Rectangular Hull Method

SEM   Scanning Electron Microscope

MWCM   Modified Wöhler Curve Method

SWT   Smith-Watson-Topper criterion

FS   Fatemi-Socie criterion

Chapter 1. Introduction

In this first chapter, the context and objectives of the study are defined. A short literature review of fretting fatigue studies going from the discovery of the phenomenon to the current works is presented.

1.1 Context of the study

Fretting phenomenon occurs at the interface of two contacting bodies under cyclic loading. It generally refers to the process of surface damage leading to corrosion pitting, surface wear by debris formation or fatigue cracking. This phenomenon occurs in many machines and engineering structures where vibrating elements are in contact with each other, like bearing, railway rails, riveted joints, blade/disc assembly of rotating machines or conductor cable (Fig.1.1). The interest in life estimation of these industrial mechanical systems considerably increased fretting fatigue research in the last decades.
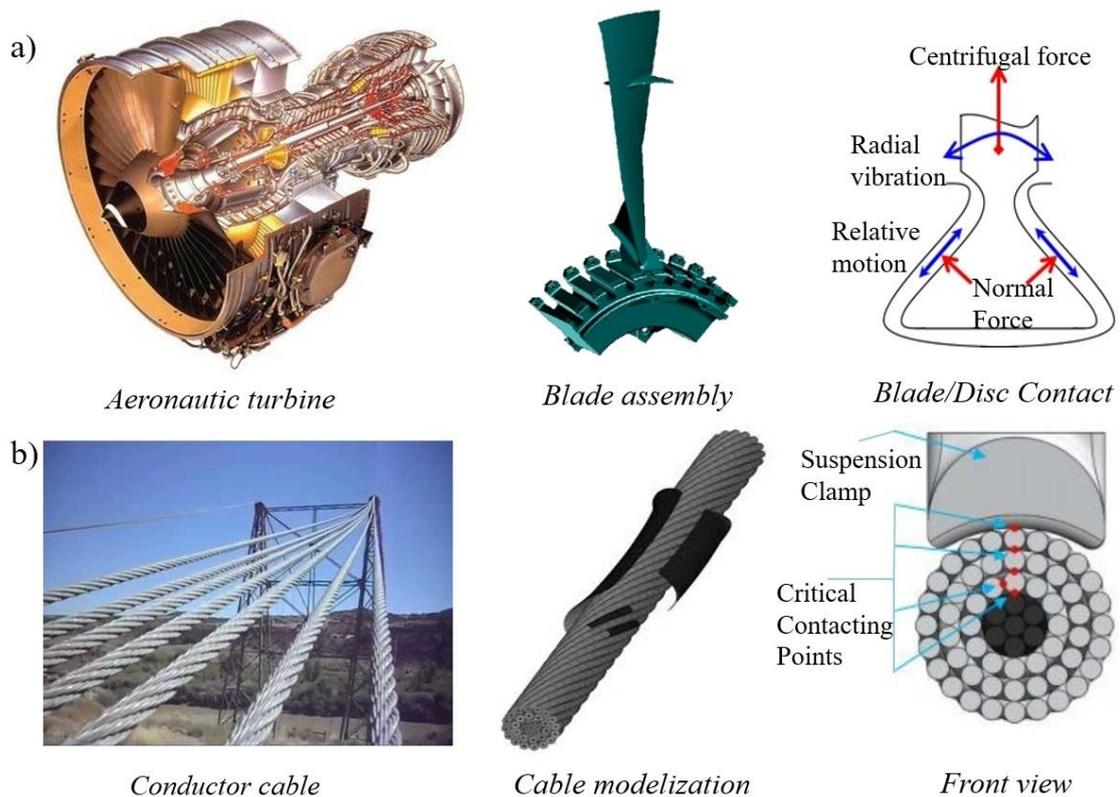
Figure 1.1. Fretting fatigue occurring a) in aeronautic industry [1], and b) in conductor cable [2].

Fretting research has been conducted to determine the variables that influence the phenomenon. Some researchers stated that almost fifty parameters may influence fretting

damage. Most of these factors are dependent on each other. The main factors influencing fatigue behavior/life, are the relative displacement amplitude, the contact geometry, the normal load, the fretting load, the coefficient of friction, the applied bulk load, and the cyclic frequency. These factors are widely studied as they are easily controllable in laboratory conditions.

This work evaluates the influence of a new factor, the phase angle between fretting and bulk loads, on the material life duration. Two materials used in industrial field were used for this study (Fig 1.2). The first one is an aluminum alloy (7050 T7451 Al), that possesses several noteworthy properties, such as high mechanical strength, corrosion resistance, fatigue strength and fracture toughness while also attaining a low specific weight. Due to this excellent set of properties, this alloy has been widely used in the aviation industry. On a conventional aircraft, it is possible to notice the presence of this alloy in several components such as horizontal and vertical stabilizers or wing coatings. The second material used in this work for the phase angle study is a stainless steel (A743 CA6NM). Due to its resistance to corrosion and cavitation damage, this material is widely used in the manufacture of hydraulic machines and components such as turbines, pumps, valves or pipes.

Figure 1.2. a) Aviation parts made of 7050 T7451 Aluminum alloy in aeronautic industry [3], and b) Hydro turbine made of A743 CA6NM [4].

1.2 State of art

Fretting was first observed in 1911 when Eden [5] reported the presence of debris as oxide in the grips of the machine while he was conducing fatigue tests. In addition, Gillet and Mack [6] found a significant reduction of fatigue life due to machine grips in 1924. To analyze this phenomenon, Tomlinson [7] designed a fretting fatigue machine of contacting annuli in small amplitude rotational oscillation in 1927 to observe the caused damages and corrosion. In 1941 Warlow-Davies [8] showed a reduction of fatigue strength (between 13% and 17%) of some steel specimens which had been previously subjected to fretting damage.

If the idea of life reduction was emerging from the first observations, henceforth it became obvious that fretting generally accelerated fatigue degradation. In 1952, McDowell [9] first carry out fatigue tests adding a fretting stress and showed a reduction of fatigue life even greater than those observed by his predecessor. A short time later it has also been proved by Fenner and Field [10] that the crack initiation in fretting fatigue configuration is greatly accelerated and occurs by 5% of fatigue life against 90% for a conventional fatigue loading.

From then, main factors influencing fretting fatigue life, as contact pressure, relative slip amplitude, environmental condition and material properties started to be investigated by experimental means, and major achievements of the field started to emerge. Nitishoka et al [11] published significant works in 1968 and proposed a model allowing prediction of fretting fatigue life from knowledge of slip amplitude, contact pressure and material properties. Waterhouse [12] completed extensive works in 1972 about the changes in coefficient of friction between contacting surface, the effect of frequency cyclic stressing, and the number of cycles required to initiate a propagating crack.

The use of Hertzian contact introduced by Mindlin in 1949 [13] to induce fretting damage has been pioneered by Johnson in 1955 [14], Wright in 1970 [15] and Brahmall in 1973 [16], each study involving a new refinement in modeling of the contact. Wright explained fretting fatigue phenomenon using stresses distribution and Bramhall noticed an apparent size effect. Waterhouse also provided complete achievement relying on the analysis of the Hertzian contact under condition of partial slip in 1981 [17]. Nowell and Hills continued Bramhall work and verified the variation of fretting fatigue life with

contact size under closely controlled experimental conditions. As achievement of their studies, they published a book in 1994 [18] which covers the areas of modeling contact problems including partial slip, modeling short cracks to deal with steep stress gradients, kinking and closure, experimental simulation of fretting fatigue, production of quantified growth criteria, and study of the surface phenomenon known to influence fretting fatigue.

Those extensive researches made possible the analytical calculation of the stress fields for some contact geometries, and open the door to the life prediction of specimens submitted to fretting fatigue conditions. The improvement of finite element methods also permits to investigate more complex geometries or study cases that involve plastic deformation. Several methods have been developed in the last decades, their predictions being confronted with experimental tests. In 1995 Petiot et al first applied a multiaxial fatigue criterion to predict the life of a steel specimen submitted to fretting fatigue condition [19]. Following the idea, Szolwinski and Farris [20] used modified version of the Smith and Wastson Topper (SWT) criterion to take into consideration the mean stress and provide predictions in terms of number of cycles to failure. Since then, multiaxial criteria were widely used in the field and extensive works emerged to identify the most appropriated methods for the fretting fatigue life prediction. In 2000, Araujo [21] applied the critical plane method and compare the efficiency of the SWT criteria with the Fatemi-Socie (FS) one. However, parameters involved in fretting fatigue, such as the friction coefficient or the contact geometry make predictions difficult and require adaptive methods.

The main obstacle for the life prediction of a specimen tested under fretting fatigue condition is the presence of strong stress gradient induced by the contact geometry. Even if the location of crack nucleation is well predicted, incoherence between the stress levels calculated and the obtained lives was observed by several authors in the early 90's. These divergences were due to the accommodation capacity of the materials under the contact which forced researchers to consider the scale effect in order to correctly estimate lives in fretting fatigue [22]. From then, stresses responsible of crack nucleation have been analyzed on a micro-volume of the material. In the beginning of the 21th century, Fouvry identified the micro-volume to calculate stress field as a characteristic length of the grain size dimension for steel [23], while Araujo proposed to take advantage of the finite element mesh, that implicitly induces average an effect, to deal with the micro-volume [24]. Nevertheless, difficulties encountered to define the structural volume led other

searchers to considerate the fretting fatigue problem as a notch effect [25], with reasonable success, bringing this method popular in the last years.

Recently, Abbasi and Majzoobi [26] investigated the effect of phase angle between normal and tangential loads on fretting fatigue behavior of Al2024-T3 using an original apparatus. They found that a phase angle affects the location of maximum dissipated energy, fretting fatigue crack initiation and lifetime. In 2017, Bhatti and Wahab [27] found that a phase angle of 180° between the tangential and the bulk loads leads to crack initiation on opposite side of an "in phase" condition. In a second work, Bhatti et al. [28] presented numerical studies, introducing a phase angle of 90° between the fatigue load and the fretting load. It revealed that, in comparison with an in-phase loading, the fatigue life is improved, and the crack can initiate at both contact edges contrary to conventional loading. However, no experimental results on the subject were found until now.

Development and improvement of laboratory equipment permit to investigate additional factors that might influence the fatigue life of specimens submitted to fretting fatigue loadings. These studies bring essential information to companies seeking improvement of mechanical components that are exhibiting failures due fretting damage. A testing system, composed by a MTS 322 test frame and a hydraulic pump, has been developed in the Department of Mechanical Engineering of the University of Brasília. It allows the distinct control of tangential load and bulk load applied during a fretting fatigue test using two different sets of servo-hydraulic pistons. New studies can emerge from this equipment.

1.3 Objective

The objective of this work is to investigate the influence of the phase angle between the tangential fretting load and the bulk fatigue load. Indeed, using adequate software and methodology, it is possible to apply and control a phase angle introduced on the cyclic fatigue load. Experimental tests were conducted to evaluate the phenomenon while numerical analysis were carried out for comparison. The objective is to show how the phase angle parameter can affect the fretting fatigue life of materials. Fatigue life predictions are also addressed using different methods to determine the most appropriate ones for fretting fatigue tests conducted with phase angle.

1.4 Scope of the thesis

In Chapter 2, the fundamentals of the fretting fatigue phenomenon such as fretting regime and contact mechanics of elastic solids are introduced.

Chapter 3 presents the different methodologies used to estimate the fatigue life in this work. A short overview of the fatigue process, paying special attention of the fretting fatigue particular case, is reminded. The critical plane methodology permitting to deal with the multiaxial state of the loads in presence is detailed, and the three different stress-based criteria tested during the study are described. Finally, to take into consideration the high stress gradient induced by the geometry of a fretting fatigue test, some methodologies based on the theory of critical distance are presented.

Chapter 4 describes the equipment and methodologies used in this work to conduct fretting fatigue tests with phase angles. The materials tested are firstly presented. The details of the new MTS 322 test frame and the procedure to follow for the introduction of a phase angle on the fatigue load are then given. The loading configurations of the three phase angles investigated ($\Phi=45°$, $\Phi=90°$, and $\Phi=135°$) and the conventional in-phase loading ($\Phi=0°$) are also described. Finally, the numerical model used to assess the stress behavior occurring for such loading configurations and to provide life estimations is also detailed.

Chapter 5 presents extensive results of the phase angle effect studying an aluminum alloy. The influence of the phase angle parameter on the fatigue life is firstly demonstrated. A complete stress analysis is then given for a better understanding of the phase angle influence on fretting fatigue loading. Life estimations using the numerical model described in Chapter 3, together with methodologies of Chapter 2 are then given. Microscopic observations of the failure process are also provided.

Chapter 6 gives complementary results on the phase angle effect studying a stainless steel, to answer the interrogations emerging from Chapter 4. Once again, experimental lives, numerical results and microscopic observations are presented.

In the last chapter, interpretations of the results, conclusions and recommendations for future works are given.

Chapter 2. Fretting fatigue fundamentals

In this chapter, some fretting fatigue fundamentals are explained in order to well frame the study case. The theory of linear elastic contact mechanics, which allows stress calculation for in-phase loadings is also presented.

2.1 Fretting regimes

Fretting fatigue is a sub-domain of contact mechanics. Indeed, fretting can be classified into two main regimes depending of the magnitude of displacement between the contacting surfaces. Assuming that no other loads are present (as seen in Figure 2.1a), the displacement might be controlled by the ratio between the tangential load, Q, and the normal pressure, P. If this ratio is low enough, a part of the contact sticks while the other slips. This gives a partial slip state usually denoted as fretting fatigue. Otherwise, if the ratio of the tangential load over the normal one is high enough, each point in the contact zone experiences a relative slip. This gives a gross slip state commonly called fretting wear. The relations between relative displacement and applied loads (depicted in Figure 2.1b) are presented as fretting maps and are commonly used to describe the fretting process [29]. Nevertheless, additional sub regimes can be established, and fretting fatigue does not occur only when the ratio Q/P is low [30].
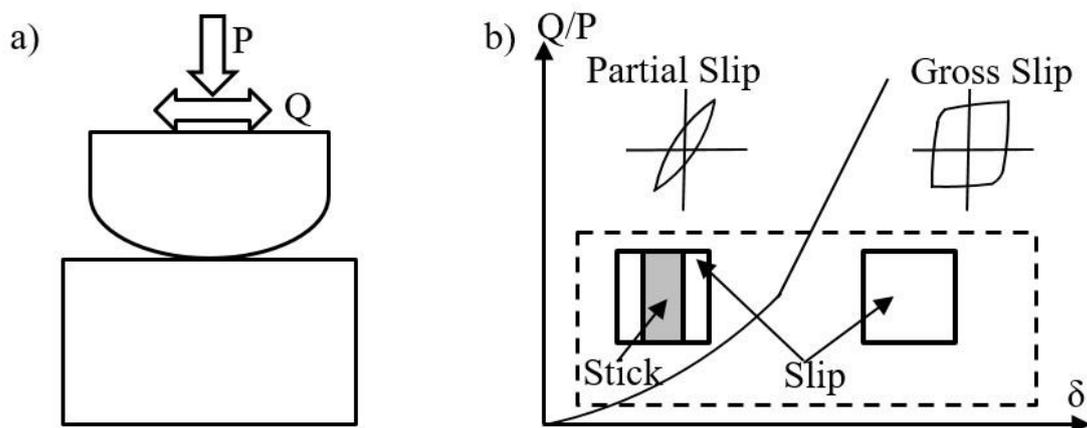
Figure 2.1. a) Applied forces for a fretting test in laboratory and b) resulting fretting maps allowing the identification of fretting regime.

The relative displacement occurring in these two main regimes leads to two distinct types of degradation, as seen if Fig. 2.2. In the case of fretting fatigue (Fig. 2.2a),

the stress concentration induced in the contact zone leads to crack nucleation whereas in fretting wear (Fig. 2.2b), degradation is observed as abrasive wear or galling. That is how it is possible to define where fretting phenomenon occurs and to identify which process is involved. Note that for higher values of load ratios and relative displacements than those observed for gross slip regime, the two bodies experiment an alternate gliding. However, in the current work, only fretting fatigue regime is studied.
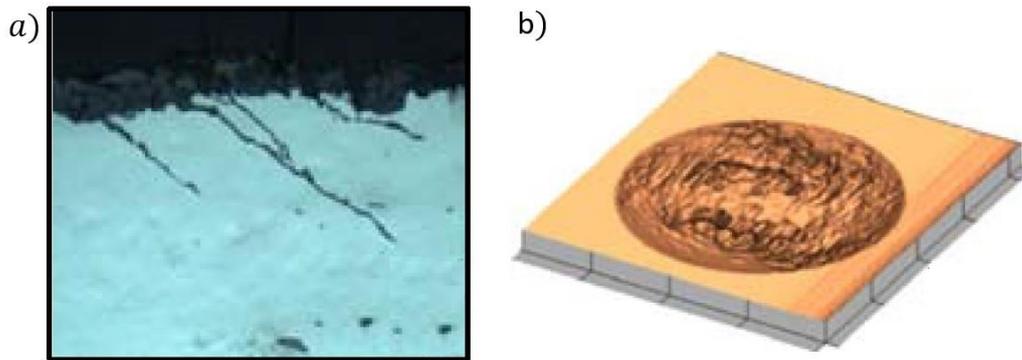
Figure 2.2. Damage observed in a) in fretting fatigue and in b) fretting wear [31].

2.2 Contact geometry

In practical applications, the contact geometry is usually complex. A small change in contact geometry has a great influence in the fatigue life as it can drastically change the local stress level and the relative displacement amplitude. When modeling the fretting fatigue problem, a classification of the different contact configurations must be defined. Figure 2.3 shows the most common contact configuration, also known as Hertzian configurations [32].
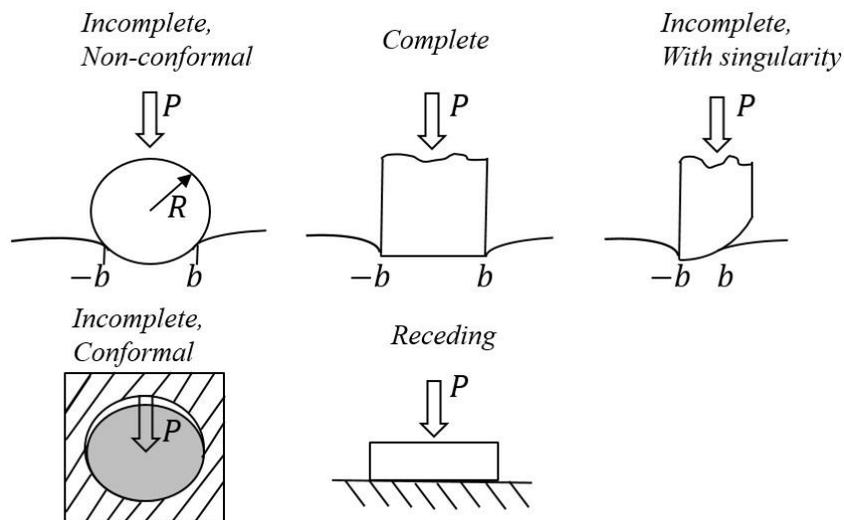
Figure 2.3. Different geometries occurring in fretting.

The contact is said to be incomplete when its size is dependent on the applied pressure and to be complete when it's independent of the pressure. For an incomplete configuration, pressure distribution may fall continuously to zero at the edges of the contact zone. A second kind of classification concerns the conformability. The contact will be said non-conformal if the half-width contact is much less than the characteristic radius, R, of the cylindrical part. In this case the cylinder is approximated by a half-plane for evaluating the deformation and stresses. Otherwise, when the radius of the cylindrical part is comparable to the contact width, the contact zone presents itself as arc so that none of the bodies can be approximated as half-plane. For this situation, the problem is defined as conformal. Note that the contact geometry of the current work is incomplete and non-conformal.

The contact occurring in practical problems can hardly be reproduced while carrying out experiments in laboratory. Nevertheless, the established classification gives a good idea on how to model and solve each problem. Simple design for testing in laboratory allows researchers to achieve complete study and provide accurate results. The three main representations encountered in laboratory nowadays are presented in the Figure 2.4.
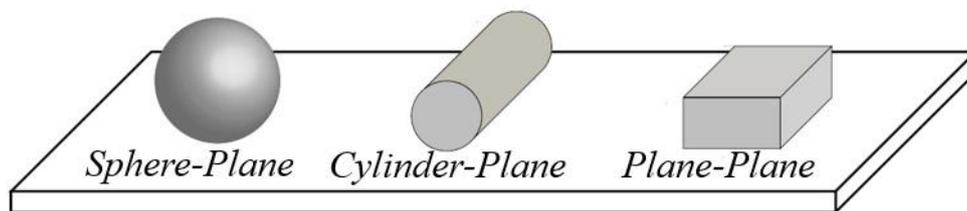
Figure 2.4. Geometry used in laboratory to conduct fretting tests.

The plane-plane representation allows to solve the complete geometry problems. If alignment is difficult to obtain for this design, the main difficulty remains that there are only few analytical solutions provided until today [33]. The Sphere-Plane and the Cylinder-Plane configurations are both covered by the Theory of Hertz and therefore have analytical solutions. However, the Sphere-Plane has a more expensive computational cost and usually require 3D modeling. The Cylinder-Plane configuration was used in the study. The analytical solution for such problem is detailed in the next section.

2.3 Analytical solutions

In this section, the equations for the stress field evaluation of a cylinder to plane contact are detailed. For the sake of simplicity, only equations that will be used in the current work are presented. The interested reader might refer to [18, 34].

2.3.1 Formulation of the problem

In the case of this study, the radius of the cylinder pad (Fig. 2.5) that insures the contact on the specimen is larger than the contact width, so that both bodies are approximated by half-planes, as explained in previously.
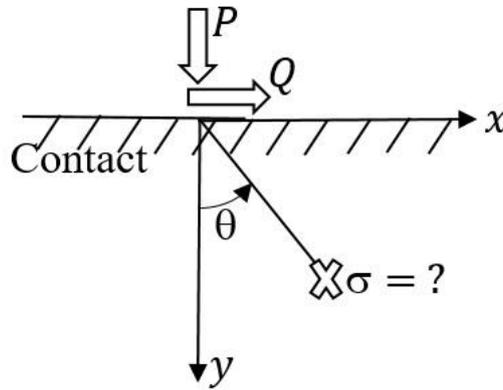
Figure 2.5. Formulation of a fretting fatigue problem for a cylinder-plane geometry.

The state of stress in this case is hence given by the Airy function solution of the following bi-harmonic equation:

$$\Phi(r,\theta) = -\frac{r\theta}{\pi}(Psin\theta + Qcos\theta) \qquad (2.1)$$

The definition of an infinitesimal radius, δr, in this bi-harmonic equation yields a stress field given by,

$$\begin{cases} \frac{1}{r}\frac{\partial \Phi}{\partial r} + \frac{1}{r^2}\frac{\partial^2 \Phi}{\partial r^2} = \sigma_{rr} = -\frac{2}{\pi r}(Pcos\theta - Qsin\theta) \\ \sigma_{\theta\theta} = 0 \\ \tau_{r\theta} = 0 \end{cases} \qquad (2.2)$$

while the introduction of Hooke's Law, leads to the following definition of the strain field,

Chapter 2 Fretting fatigue fundamentals

$$\begin{cases} \varepsilon_{rr} = \frac{1}{8G}\{\sigma_{rr}(1+\kappa) + \sigma_{\theta\theta}(\kappa-3)\} = \frac{1}{8G}\sigma_{rr}(1+\kappa) \\ \varepsilon_{\theta\theta} = \frac{1}{8G}\{\sigma_{\theta\theta}(1+\kappa) + \sigma_{rr}(\kappa-3)\} = \frac{1}{8G}\sigma_{rr}(\kappa-3) \\ \qquad\qquad \gamma_{r\theta} = \frac{\tau_{r\theta}}{G} = 0 \end{cases} \qquad (2.3)$$

In Eq. (2.3), $k = 3 - 4v$, G being the shear modulus and v being the Poisson's ratio.

Using the plane strain formulation, the displacement can be found by integration, as $\varepsilon(i) = \frac{du}{di}$. To solve contact problems, it is important to obtain an influence function that forms the kernel of an integral equation by finding the surface displacement. This may be obtained by setting $\theta = \pm\pi/2$ and converting to Cartesian coordinates. Finally, it is preferable to work with the following equations which use terms of the derivatives of $(x), v(x)$:

$$\frac{\partial u}{\partial x} = \frac{\kappa-1}{4G}p(x) + \frac{\kappa+1}{4\pi G}q(x)\int\frac{q(\xi)d\xi}{\xi-x} \qquad (2.4)$$

$$\frac{\partial v}{\partial x} = -\frac{\kappa-1}{4G}q(x) + \frac{\kappa+1}{4\pi G}q(x)\int\frac{p(\xi)d\xi}{\xi-x} \qquad (2.5)$$

From this point, the derivation of the relative displacement, $h(x)$, at any point is given by direct distribution and shear tractions applied over the surface, as seen in Figure 2.6.
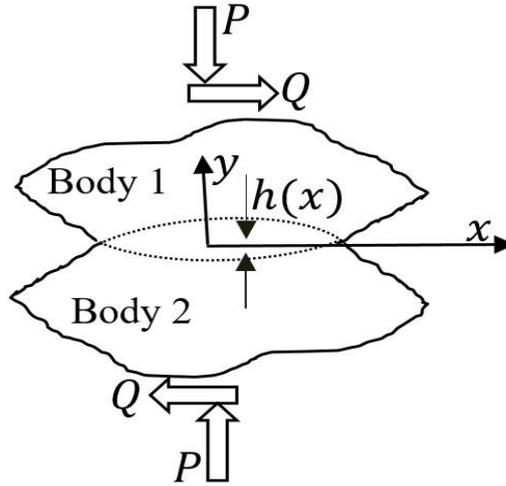
Figure 2.6. Visualization of contacting bodies, forces in presence, and function that characterize the relative displacement.

Having defined Eq's (2.4) and (2.5), it is possible to describe the relative displacement between two points on the surface of one body, $v_1(x)$ and $v_2(x)$, as follows:

$$h(x) = v_1(x) - v_2(x)$$

$$\frac{1}{A}\frac{\partial h}{\partial x} = \frac{1}{\pi}\int\frac{p(\xi)d\xi}{x-\xi} \pm \beta q(x)$$
(2.6)

$$\text{With } \begin{cases} A = \frac{\kappa_1+1}{4G_1} + \frac{\kappa_2+1}{4G_2} \\ \beta = \frac{\Gamma(\kappa_1-1)-(\kappa_2-1)}{\Gamma(\kappa_1+1)+(\kappa_2+1)} \\ \Gamma = \frac{G_2}{G_1} \end{cases}$$

where A and β are respectively the composite compliance and the Dundur's parameter, and the sign of $\beta q(x)$ depends on which body is observed. Equation (2.6) can be used as the basis of a solution for contact problem.

2.3.2 Analysis of the normal pressure

In the case where no shear tractions arise, the right term of Eq. (2.6) is equal to zero, and the relative displacement will only be expressed as function of the normal pressure. Assuming that the contact occurs in a centered zone equivalent of $2a$ in size, the inversion of such relation gives:

$$p(x) = -\frac{w(x)}{A\pi}\int_{-a}^{a}\frac{h\prime(\xi)d\xi}{w(\xi)(\xi-x)} + Cw(x)$$
(2.7)

From inversion of Cauchy singular integral equations of the first kind, the terms C is equal to zero and the function $w(x)$ is equal to $\sqrt{a^2 - x^2}$, if there is no singularity at the end of integral. The normal pressure can then be expressed as:

$$p(x) = p_0\sqrt{1 - \left(\frac{x}{a}\right)^2}$$
(2.8)

where p_0 is the peak pressure and a is the half-width of the contact line. Equation (2.8) has been established ensuring equilibrium between the contact pressure and the applied load and following the Hertz contact theory [12]. Indeed, with this formulation, the stress distribution in the contact width (Fig. 2.7) is function of the normal force applied, the curvature of bodies in the contact zone, and their Young moduli. Thus, the essential parameters of the problem are:

$$a = \sqrt{\frac{4PR}{\pi E^*}}$$
(2.9)

$$p_0 = \frac{2P}{\pi a}$$
(2.10)

$$\text{where} \begin{cases} P = \frac{\pi E^* a^2}{4R} \\ R = \left(\frac{1}{R_1} + \frac{1}{R_2}\right)^{-1} \\ E^* = \left(\frac{1-v_1^2}{E_1} + \frac{1-v_2^2}{E_2}\right)^{-1} \end{cases} \tag{2.11}$$

Note that in Eq. (2.9), P is the applied load, R is the radius describing the curvature of a body and E is the Young modulus. The subscripted indexes are used to describe respectively the first and the second solid body.
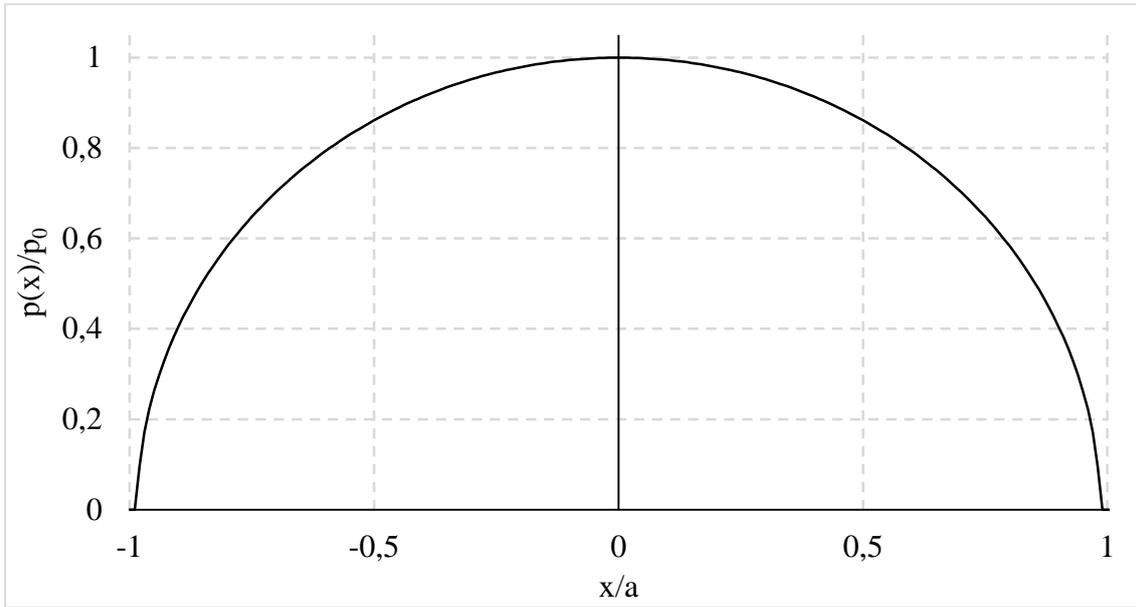
Figure 2.7. Pressure distribution over the contact zone.

2.3.3 Analysis of the shear traction distribution

The relations presented here have been established for the case where only the normal pressure is applied. In fretting fatigue, when assuming the Coulomb's law the tangential force should be proportional to the normal force. In the case of our study, the application of this tangential load will lead to a state of partial slip, where the contact will be divided in two zones [13,35].

The first zone characterizes the slip of surfaces, where the shear tractions act in a direction which is opposed to the relative motions of the surface particle. In this zone, the shear tractions are related to the friction law. Considering that $g(x) = u_1(x) - u_2(x)$, the two following equations characterize the slip zone.

$$|q(x)| = -fp(x) \tag{2.12}$$

13

$$sgn\big(q(x)\big) = -sgn\left(\frac{\partial g}{\partial t}\right) \tag{2.13}$$

Note that f is the friction coefficient which depends on the nature of the contacting surfaces. The second zone is a stick area, where there is no slip between surfaces so that the relative displacement between particles remains constant. In this zone, the shear tractions are less or equal to the limited frictional value, which gives the following characteristic relations:

$$|q(x)| \leq -fp(x) \tag{2.14}$$

$$\frac{u_1(x)}{dx} - \frac{u_2(x)}{dx} = \frac{\partial g(x)}{dx} = g_0(x) \tag{2.15}$$

In the case where a cylinder part ensures pressure on a flat one, the slip takes place in two symmetrical regions $a > |x| \geq c$, which surround a central stick zone $|x| < c$. Recovering Eq. (2.8), in the case where both bodies are in fully sliding state, yields:

$$q(x) = fp_0\sqrt{1 - \left(\frac{x}{a}\right)^2} \tag{2.16}$$

For the Partial slip, it is convenient to add a perturbation $q'(x)$, that is equal to zero in the slip zone, and remains to be determined in the stick zone.

$$q(x) = fp_0\sqrt{1 - \left(\frac{x}{a}\right)^2} + q'(x) \tag{2.17}$$

To determine $q'(x)$ in the slip zone, it is possible to use the same approach than with the pressure (Eq. 2.6) but for the tangential load. The motion particle is now evaluated in u, and as there is no relative displacement in the stick zone, $g_0'(x) = 0$. The Dundur's parameter is also set to zero, while the two materials in contact are similar, and Eq. (2.6) becomes:

$$\frac{1}{\pi}\int_{-a}^{a} \frac{q(\xi)d\xi}{\xi - x} = 0 \tag{2.18}$$

Substituting Eq. (2.17) in Eq. (2.18) gives an integral form function of fp_0, and using again inversion of Cauchy integral leads to the following expression of $q'(x)$:

$$q'(x) = -fp_0 \left(\frac{c}{a}\right)\sqrt{1 - \left(\frac{x}{c}\right)^2} \tag{2.19}$$

It is now possible to write the tangential load in the very convenient form of Eq. (2.17) and to obtain the size of the stick zone $2c$ by enforcing tangential equilibrium:

$$q(x) = fp_0\sqrt{1 - \left(\frac{x}{a}\right)^2} + q'(x) \qquad (2.17)$$

$$q'(x) = \begin{cases} 0, & if\ c \leq |x| \leq a \\ -fp_0\left(\frac{c}{a}\right)\sqrt{1 - \left(\frac{x}{c}\right)^2}, & if\ |x| < c \end{cases} \qquad (2.20)$$

$$\frac{c}{a} = \sqrt{1 - \left|\frac{Q}{fP}\right|} \qquad (2.21)$$

Note that looking to Eq's. (2.8) and (2.17) the term $q'(x)$ could correspond to a perturbation of the normal distribution curve. For a ratio Q/fp_0 equal to 1, the curve is not perturbed. When reducing this ratio, a perturbation appears at the center of the contact ($x/a = 0$), characterizing the zone of the contact that sticks. The central stick zone increases when the ratio Q/fp_0 decreases, as seen in Figure 2.8.
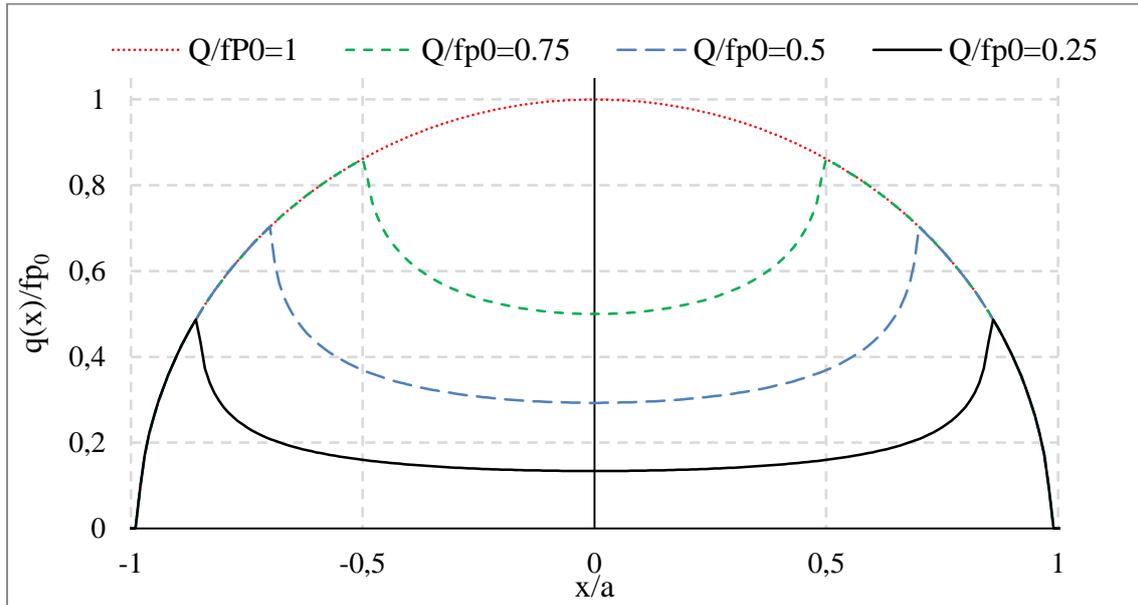
Figure 2.8. Shear traction distribution for different value of Q/fp₀.

Equation (2.17) has been established for a monotonically increasing tangential force. In fretting fatigue, the variation of tangential force is cyclic and, as consequence, the shear traction has an history. At an infinitesimal time-lapse after the removal of the loading, the requirement for shear tractions to oppose relative motion is violated, leading

to an instantaneous state of total stick. Afterwards, during the decreasing of the load, the shear traction changes direction and, due to the loading history, it appears reversed slip at the edge of the contact. Indeed, at the edges of the contact, there are reversed slip zones ($c' < |x| \leq a$), where shear traction got inverted. It is necessary to redefine the stick zone ($|x| \leq c'$), and to introduce a correctional term which insures a continuous load history. This process is depicted in Fig. 2.9.
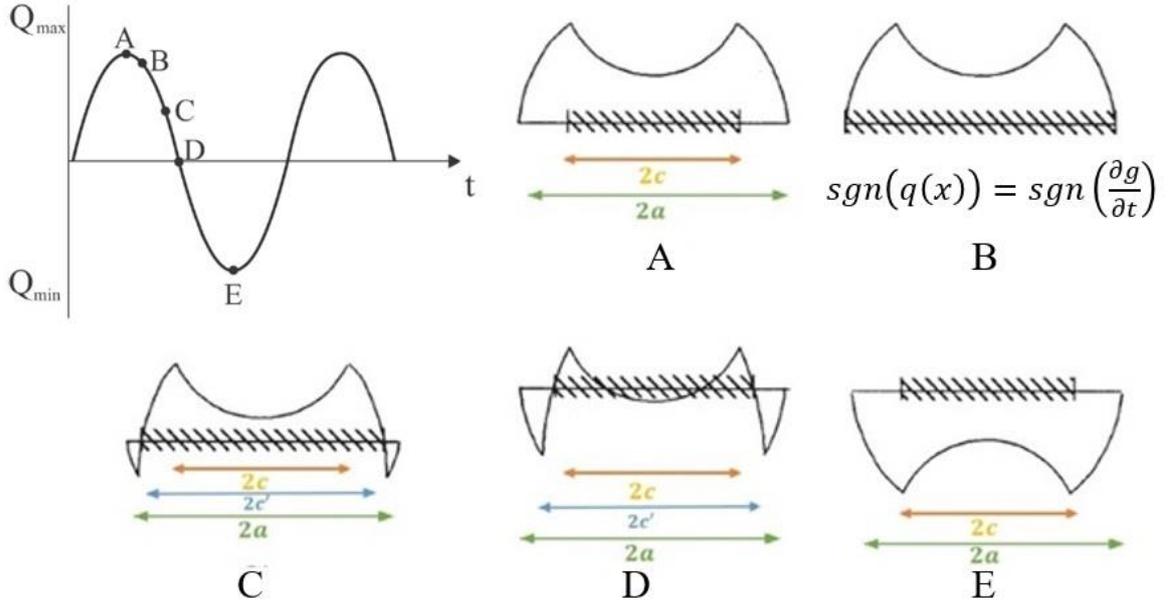
Figure 2.9. Evolution of shear traction distribution during a cyclic loading.

Therefore, in order to accommodate this effect, Eq. (2.17) is modified such that,

$$q(x) = -f p_0 \sqrt{1 - \left(\frac{x}{a}\right)^2} + q'(x) + q''(x) \tag{2.22}$$

$$\text{with } q'(x) = \begin{cases} 0 & \text{if } c \leq |x| \leq c' \\ -f p_0 \left(\frac{c}{a}\right) \sqrt{1 - \left(\frac{x}{c}\right)^2} & \text{if } |x| < c \end{cases} \tag{2.23}$$

$$\text{and } q''(x) = \begin{cases} 0 & \text{if } c' \leq |x| \leq a \\ +2 f p_0 \left(\frac{c'}{a}\right) \sqrt{1 - \left(\frac{x}{c'}\right)^2} & \text{if } |x| < c' \end{cases} \tag{2.24}$$

$$\text{where } \left(\frac{c'}{a}\right) = \sqrt{\frac{1}{2} \times (1 + (c/a)^2)} \tag{2.25}$$

Note that for the point E in Fig. (2.9), the shear traction distribution is completely reversed, so that for the next loading it is possible to use Eq. (2.23) with an appropriate change of sign. In fact, the terms $fp_0\sqrt{1-\left(\frac{x}{a}\right)^2}$ and $q'(x)$ are negative during unloading and positive during loading while the corrective term $q''(x)$ is positive during unloading and negative during loading.

2.3.4 Effect of the fatigue load

Fretting fatigue normally takes place in presence of bulk stresses within one or both of the contacting bodies. In the case of this study, the tested flat specimen is submitted to this fatigue load whereas the contacting cylindrical pad is not (Fig. 2.10). While the bulk stress is applied to the specimen in condition of plane strain, the difference in relative tangential displacement in the stick zone is now equal to $-\epsilon_{xx} = -\frac{\sigma(1-v)}{2\mu}$ which gives at the end a shortly different expression for the perturbation:

$$q'(x) = -fp_0\left(\frac{c}{a}\right)\sqrt{1-\left(\frac{x-e}{c}\right)^2} \tag{2.30}$$

where $e = \frac{\sigma a}{4fp_0}$ \hfill (2.31)

As a result, the shear traction differs due to this offset e. Figure 2.11 shows the comparison of the shear traction distribution with and without an applied bulk load.
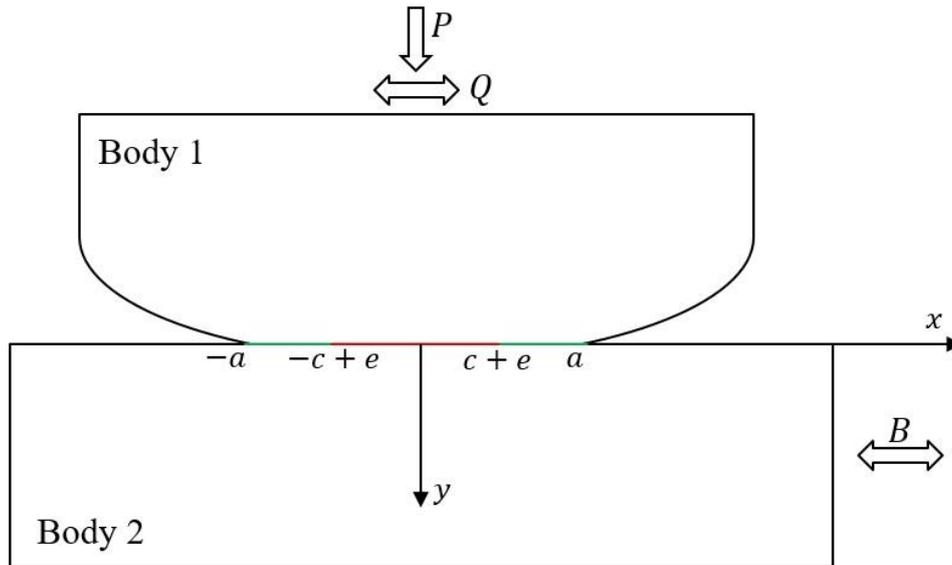
Figure 2.10. Visualization of every applied loads, and stick/slip zones for a fretting fatigue test.
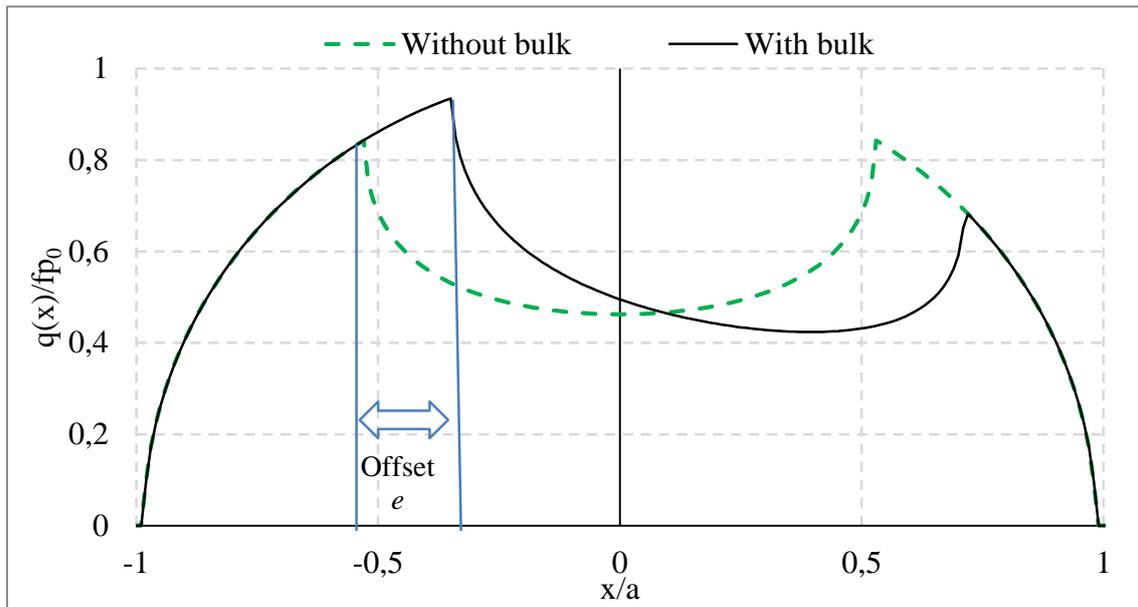
Figure 2.11. Influence of the bulk load on the shear traction distribution.

2.3.5 Muskhelishvili's potential

After the evaluation of the surface tractions, subsurface stresses can be obtained by using Muskhelishvili's potential [36]. The potential can be defined using coordinates in the complex form ($z = x + yi$), as follow:

$$\psi(z) = \frac{1}{2\pi i} \int \frac{p(t) - iq(t)}{t - z} dt \tag{2.32}$$

where $p(t)$ and $q(t)$ are respectively the arbitrary normal and shear stresses distributions, as depicted in Figure 2.12.
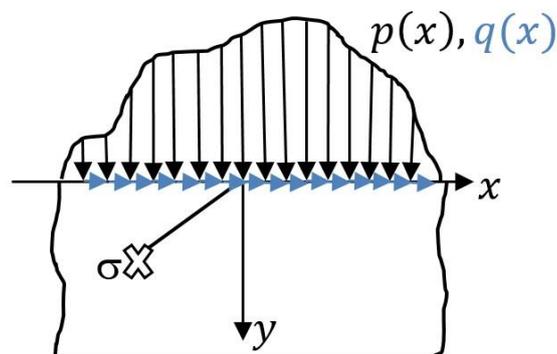
Figure 2.12. Half plane submitted to arbitrary stress distribution.

Under sliding conditions, these distributions are related to Eq. (2.14) and the equation can be rewritten as:

$$\psi(z) = \frac{1-if}{2\pi i} \int \frac{p(t)}{t-z} dt \tag{2.33}$$

Once the potentials have been determined, the stress components can be extracted as follow:

$$\sigma_{xx} + \sigma_{yy} = 2(\psi(z) + \overline{\psi}(\bar{z})) \tag{2.34}$$

$$\sigma_{yy} - \sigma_{xx} + 2i\tau_{xy} = 2((\bar{z} - z)\psi'(z) + \overline{\psi}(z) - \psi(z)) \tag{2.35}$$

where $\psi(z)$ is the potential function derivation in relation to z, $\overline{\psi}(z)$ is the conjugate function and $\overline{\psi}(\bar{z})$ is the conjugate function applied to the conjugate of z.

2.3.6 Determination of the stress field

At this point, the stresses components can be determined by superposing the effects of the normal pressure, the shear traction and bulk load, and using Muskhelishvili's potential theory. For example, at a given point of coordinates (x,y), located under the contact, the evaluation of the component σ_{xx} of stress tensor can be obtained with the superposition of the results obtained for the different stress tractions distributions. Although, the introduced perturbations terms, *q'(x)* and *q''(x),* must be considered, and as discussed in the previous section, their signs change during the loading process. Note that four different combinations are used to express the stress field at the maximum and minimum loading time, but also during unloading and reloading, as already discuss in previous sections. For instance, the σ_{xx} components of the stress tensor can be written as follow for the different stages:

- At maximum load:

$$\frac{\sigma_{xx}(x,y)}{p_0} = \left(\frac{\sigma_{xx}^n\left(\frac{x}{a},\frac{y}{a}\right)}{p_0}\right) + f\left(\frac{\sigma_{xx}^t\left(\frac{x}{a},\frac{y}{a}\right)}{fp_0}\right) - f\frac{c}{a}\left(\frac{\sigma_{xx}^t\left(\frac{x-e}{c},\frac{y}{c}\right)}{fp_0}\right) + \sigma_B \tag{2.36}$$

- During unloading:

$$\frac{\sigma_{xx}(x,y)}{p_0} = \left(\frac{\sigma_{xx}^n\left(\frac{x}{a},\frac{y}{a}\right)}{p_0}\right) - f\left(\frac{\sigma_{xx}^t\left(\frac{x}{a},\frac{y}{a}\right)}{fp_0}\right) + 2f\frac{c'}{a}\left(\frac{\sigma_{xx}^t\left(\frac{x-e'}{c'},\frac{y}{c'}\right)}{fp_0}\right) - f\frac{c}{a}\left(\frac{\sigma_{xx}^t\left(\frac{x-e}{c},\frac{y}{c}\right)}{fp_0}\right) + \sigma_B \tag{2.37}$$

- At minimum load:

$$\frac{\sigma_{xx}(x,y)}{p_0} = \left(\frac{\sigma_{xx}^n\left(\frac{x}{a},\frac{y}{a}\right)}{p_0}\right) - f\left(\frac{\sigma_{xx}^t\left(\frac{x}{a},\frac{y}{a}\right)}{fp_0}\right) + f\frac{c}{a}\left(\frac{\sigma_{xx}^t\left(\frac{x-e}{c},\frac{y}{c}\right)}{fp_0}\right) + \sigma_B \tag{2.38}$$

- During reloading:

$$\frac{\sigma_{xx}(x,y)}{p_0} = \left(\frac{\sigma_{xx}^n\left(\frac{x}{a},\frac{y}{a}\right)}{p_0}\right) + f\left(\frac{\sigma_{xx}^t\left(\frac{x}{a},\frac{y}{a}\right)}{fp_0}\right) - 2f\frac{c'}{a}\left(\frac{\sigma_{xx}^t\left(\frac{x-e'}{c'},\frac{y}{c'}\right)}{fp_0}\right) + f\frac{c}{a}\left(\frac{\sigma_{xx}^t\left(\frac{x-e}{c},\frac{y}{c}\right)}{fp_0}\right) + \sigma_B \qquad (2.39)$$

where σ_{xx}^n, σ_{xx}^t, σ_B are the terms calculated for the components calculated for the normal, tangential and bulk loads respectively. Similar formulations can be derived for the σ_{yy} and τ_{xy} components of stress tensor for the same loading times, and the σ_{zz} component can be obtained from the other two direct stresses.

Chapter 3. Fatigue life estimation

The methodology used for the fatigue life estimation attempted in this work is detailed in this chapter. A quick overview of the fatigue process is established. The state of stress provided by the fretting fatigue loading configuration and the strong stress gradient induced by the contact geometry require special attention. To deal with this issue, multiaxial stress-based criteria and non-local approaches are presented.

3.1 Fatigue

In engineering, the term fatigue is widely used to refer to damage or failure of materials under cycling loading. The fatigue damage is a phenomenon observed for the first time in 1829 by W.A.J. Albert [37] on a rupture of coal's conveyor and which was firstly described as a mysterious phenomenon that may occur without warning signs. The term of fatigue was first applied in 1839 by Poncelet [38]. The understanding of this phenomenon became essential as fatigue is responsible of approximately 90% of metal failure [39]. Schutz presented an overview of the contributions brought to the field by several searchers from 1837 to the end of the 20th century [40]. In the beginning, works focused on metallic materials, but the interest in non-metallic materials and composite presenting a good potential for mechanical application had quickly grown. Extensive studies were conducted on the fatigue process of ceramics [41,42], polymers [43,44], and more recently composites [45].

Nowadays it is possible to clearly define fatigue as a permanent, progressive and localized alteration process that occurs in a material subjected to conditions that produce stresses at a single point or at various points, and which can lead to cracking or complete fracture of the component after a sufficient number of cycles. In fatigue, failures happen due to loads that vary over time, not to static loads. These failures typically occur after a certain number of cycles, at stress levels significantly lower than the values of the material yield stress. Fretting fatigue regime, is characterized by the same failure process, the exception being that stresses are very concentrated which results in cracks nucleation well located. The fatigue process is composed of three distinct steps. Firstly, a nucleation step corresponding to the creation of micro-cracks associated to a difficult growing prediction,

followed by a propagation step where the micro-cracks nucleated will growth stably in time according to the load conditions and a failure step where cracks reach an unstable size causing the rupture of the part.

3.1.1 Crack nucleation

The crack nucleation, that makes possible the fatigue failure, is caused by various reasons. Industrial metallic materials generally possess complex compositions with a large number of additional elements, so the micro-heterogeneity of the microstructures can be responsible of crack nucleation. During loadings, dislocations tend to accumulate at porosities [46], difficultly avoidable in material conception, or at grain boundaries [47], provoking micro-cracks nucleation. In addition, the application of mechanical stresses during fatigue loading leads to a dislocation movement on the slip planes of certain grains caused by shear stresses. This movement causes the appearance of stairs at the surface, known as irreversible slip bands which, depending on their height and orientation, bring about micro-cracks nucleation [48]. However, in fretting fatigue, cracks are nucleated at the edge of the contact where the stresses are mostly concentrated (Fig. 3.1). When the structure geometry induces strong stress gradients, and is responsible of crack nucleation, the phenomenon is known as notch effect. The notch effect is subject of numerous studies and simulations, as in industrious field, real parts contains corners, leaves or holes that involve such stresses concentrations.
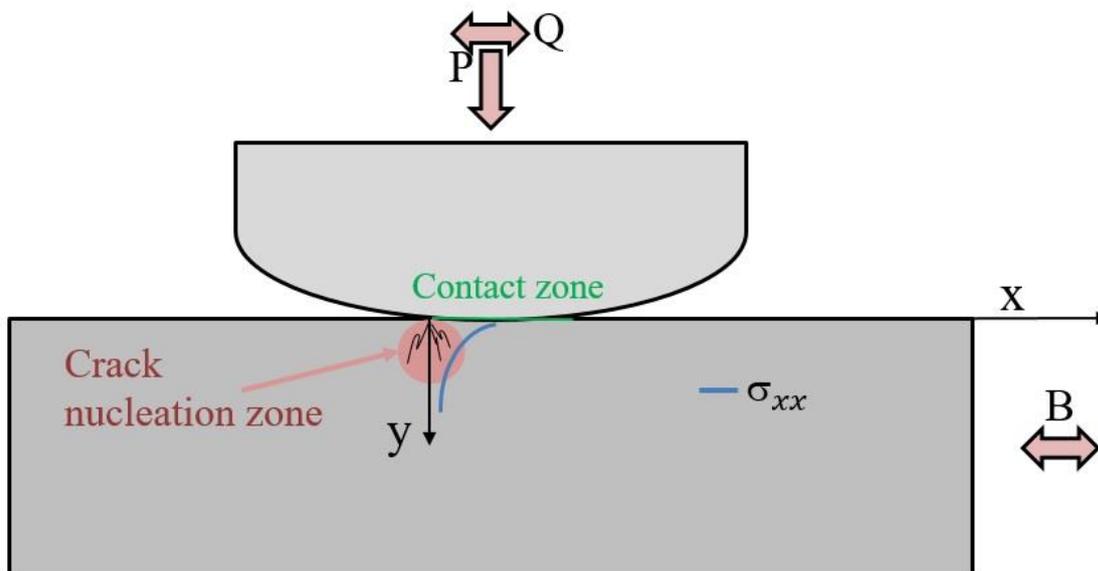
Figure 3.1. Stress gradient responsible of crack nucleation in fretting fatigue

3.1.2 Crack propagation

Not all nucleated crack continues to propagate, leading to a fracture. Frost was the first to observe the phenomenon of cracks arrest at the bottom of notch [49]. Widely confirmed since then, this phenomenon is due to the rapid decrease in the stresses concentration effect in the vicinity of the stress raiser. The capacity of the crack to propagate then depends on the value of the stresses that contribute to the opening of the crack. Nevertheless, if the value of the stresses responsible of the crack opening is low enough, the crack will never propagate and will not be able to reach the critical size leading inevitably to failure. In such a case, the stress value is the so-called fatigue limit σ_0 of the material. In fretting fatigue, the macroscopic direction of crack propagation is perpendicular to the normal stress, which could be affiliated to the opening mode I. However, the shear tractions induced by the loads applied to the pad also play a role in the propagation, and clearly remind the shear plane opening mode II (Fig. 3.2).
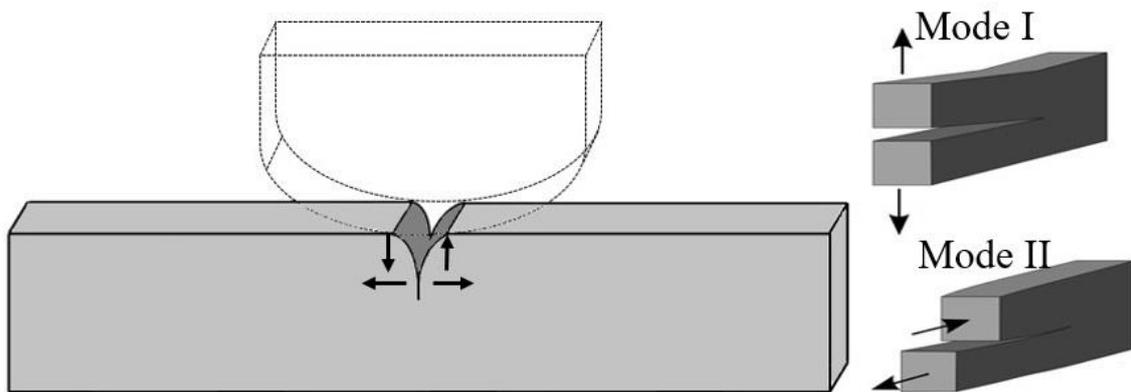
Figure 3.2. Opening crack of a fretting fatigue specimen

After reaching a certain critical size, the propagation of a crack can be predicted, using an analytical solution of constraints in the neighborhood of the crack tip governed by the stress intensity factor K. This stress intensity factor was introduced by Irwin [50] and depends on the geometry, on the size and the location of the crack, and on the stress magnitude and distribution. In fact, the classical observations of the crack velocity in fatigue process can be separated in three distinct regimes in terms of speed propagation. The first regime which still could be associated to the crack initiation is delimited by a propagation threshold term ΔK_{th} below which the crack stops to propagate. The second regime, associated to crack propagation, shows propagation velocity as a linear evolution of the propagation velocity in logarithm scale with ΔK. This linear dependence is known

as the Paris law, Paris [51] being the first to establish its existence. The last regime of propagation velocity corresponds to the last fatigue step.

3.1.3 Fracture

The crack continues to grow with time as long as there are sufficient stresses. At a given moment, the crack becomes large enough, so that the stress intensity factor K is elevated to the fracture toughness level of the material Kc, and a sudden failure occurs instantaneously. Naked eye examination of fatigue failure (Fig. 3.3) exhibits easily this sudden fracture. The region near the crack origin has a more polished appearance with Wallner lines which correspond to the propagation process while the rough region, similar to a fragile fracture, corresponds to the portion of the material that ruptured catastrophically when the crack reached its limit size.
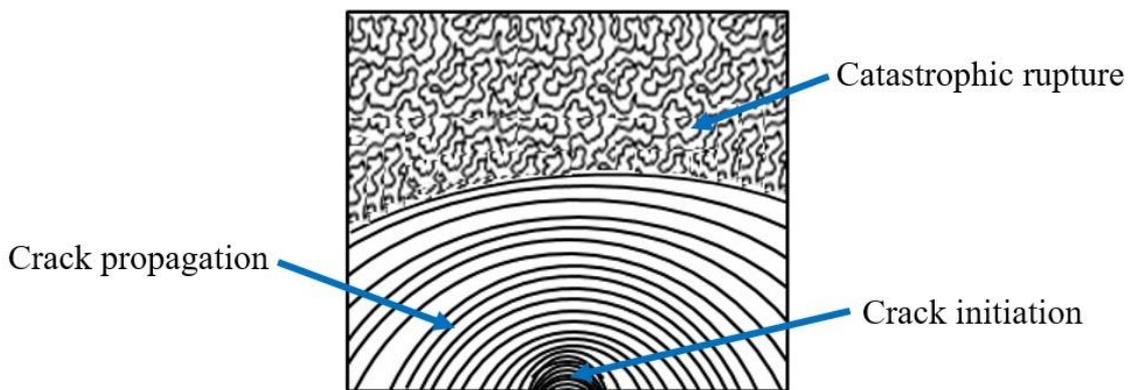
Figure 3.3 Schematic representation of a naked eye observation of fatigue failure, with distinct zones.

3.1.4 Fatigue life

Fatigue strength of materials can be established by uniaxial fatigue tests. These studies allow to put into service several industrial parts submitted to uniaxial loading. The laws or equations that define the behavior of a material under fatigue conditions are generally empirical relationships obtained in laboratories by testing specimens of the material to be studied. In these laws, the amplitude of stress or deformation is related to the number of cycles until failure. Methods for characterization of life in terms of nominal stress arise from the work of Wöhler [52] in 1960, who analyzed the fatigue phenomenon in axes of railway machines. Most of fatigue life prediction methods are based on the Wöhler diagram commonly called S-N curve. This curve relates the nominal stress amplitude applied to a laboratory specimen with the number of cycles until the failure of this specimen (Fig. 3.4). In laboratory, these data can be obtained from different loading

configurations such as bending, torsion or tension/compression, and with different load ratios (minimal load value over maximal load value).

Some materials, such as steel alloys, when subjected to constant stress amplitudes, have a lower limit of stress amplitude below which the specimen failure cannot be observed even with a very high number of cycles (Nf≥N0). This stress amplitude, already discussed in the previous section, is known as the fatigue limit, σ_0. For other materials, like aluminum, which is a non-ferrous metal, the fatigue limit is not well defined. In this case the fatigue limit continues to decrease while the number of cycles increases. A fatigue limit for such cases is adopted as the stress amplitude in which the specimen supports a given number of cycles to failure, like 10^7 for aluminum alloys.
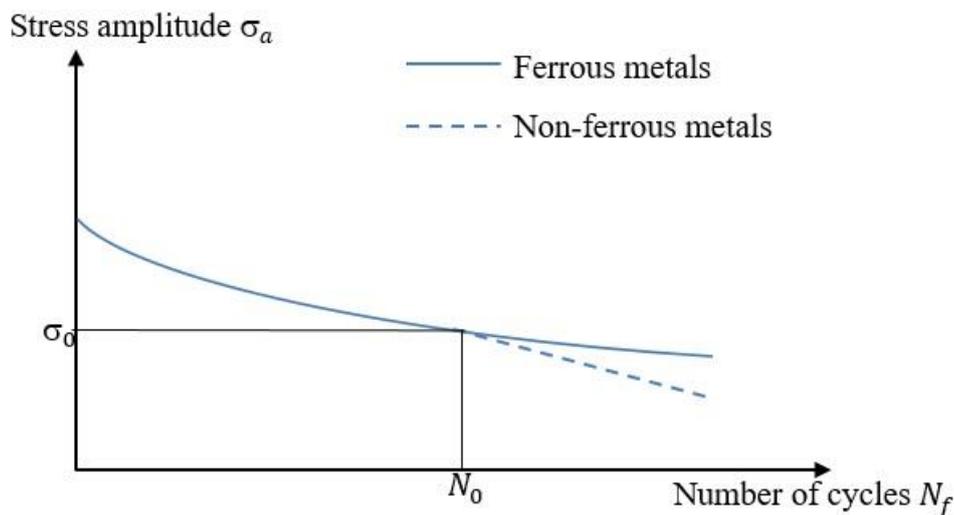
Figure 3.4. S-N Curves for ferrous and Non-ferrous metals.

3.2 Multiaxial problem

Uniaxial approach remains insufficient for various industrial applications that involve multiaxial stresses. Parts like drive shafts can for example be submitted to torsion and flexion at the same time. Hence it appeared necessary to develop predictive models which will consider the multiaxial stresses to characterize fatigue strength of these more complex structures. The first rotational machine operating torsion and flexion was presented by Lanza [53], and preliminary results emerged. Multiaxial models to estimate fatigue life came next, based on stresses combination [54]. Later, some multiaxial models based on deformation appear to focus on the low cycle fatigue regime study, were high stress levels give place to plastic deformation. However, stress based multiaxial models

still widely used as they are representative of numerous fatigue cases, where deformations are relatively small.

Besides that, in fretting fatigue, crack initiation occurs in a contact region between two bodies which is governed by a state of stresses that is multiaxial in nature (Fig. 3.5a). It is then obvious to use the developed multiaxial fatigue model predicting fatigue life of material submitted to fretting fatigue. There are three main approaches to predict fatigue life of material submitted to multiaxial loading: the critical plane approach, the invariant tensor approach and the energetic approach. The critical plane has been used for our study, as it is an appropriate approach for fretting fatigue studies [21].

3.2.1 Critical plane approach

The idea of this approach is that crack initiates in preferential planes characterized by high stress values. The critical plane has the advantage of giving not only the fatigue life but also information about the location and the direction estimated for the crack nucleation. This is very attractive from a mechanical point of view, the notion of critical plane reminding clearly the well-known preferential slip plane process which states that cracks initiate in preferential material planes. These preferential material planes are usually those with the higher shear stresses [55-57]. However, the normal stress must also be taken into account as it keeps the crack faces open and makes their growth easier [58-61]. To find the critical planes, it is then necessary to estimate the best combination of shear and normal stress.

Every material plane Δ of a material component, passing through the point O, subjected to multiaxial fatigue is defined by its normal vector **n** and by its spherical coordinates t and θ (Fig.3.5b). For the instant t, the Cauchy theorem states that the expression of the stress vector $\boldsymbol{t}(t)$ is function of this normal vector $\boldsymbol{n}$ and the stress tensor $\boldsymbol{T}(t)$:

$$\boldsymbol{t}(t) = \boldsymbol{T}(t).\boldsymbol{n} \tag{3.1}$$

The stress vector can be decomposed in two components (Fig3.5c) which are its normal and its shear stresses, given by the following equations:

$$\begin{cases} \boldsymbol{\sigma}(t) = (\boldsymbol{T}(t)\boldsymbol{n}.\boldsymbol{n})\boldsymbol{n} \\ \boldsymbol{\tau}(t) = \boldsymbol{T}(t)\boldsymbol{n} - \boldsymbol{\sigma}(t) \end{cases} \tag{3.2}$$
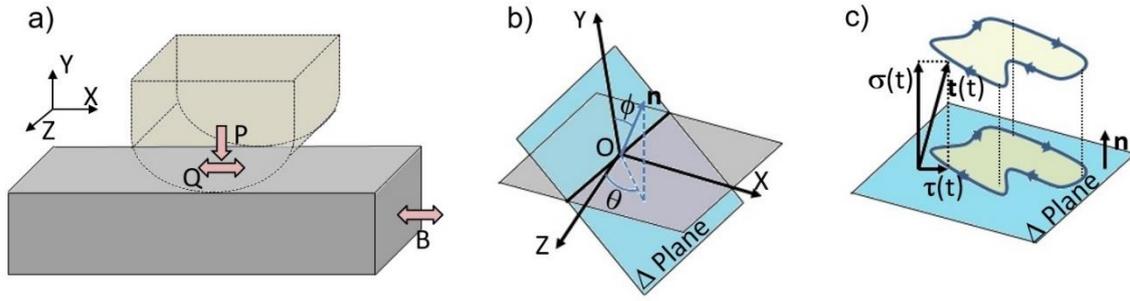
Figure 3.5 a) Specimen subjected to multiaxial loading in fretting fatigue, b) Definition of a material plane with its spherical coordinates, and c) history and decomposition of the stress vector.

Note that in this study, the complete loading histories of the stress tensor have been extracted from numerical simulations and set into matrix using *Matlab©* software. The stress vector is deducted, by projection in the material plane basis, and use of the Cauchy theorem. A step of 5° has been chosen to vary successively the penetration angle ϕ and the orientation angle θ of the material planes Δ, so that the stress vector and its component have been calculated in about 5 000 material planes. To determine which plane is the critical one, it remains necessary to define the quantities that characterize the normal and the shear stresses, and to apply a multiaxial fatigue criterion based on the critical plane approach.

3.2.2 Definition of the normal stress

Most of existing models use different terms to describe the normal and shear stresses acting on a material plane. The normal component of the stress vector is easily calculated at any time using the dot product (Eq. 3.2), but it remains to specify the value used as driving parameter for the crack nucleation. During one cycle, the normal stress $\sigma_n(t)$ can for example be characterized by its maximum value, σ_{nmax} its minimum value σ_{nmin}, its amplitude σ_a , or its mean value σ_{nmean} (Fig. 3.6). These quantities are link together by the following equations and the next figure permits to visualize them, for a classical sinusoidal loading:

$$\sigma_{na} = \frac{\sigma_{nmax} - \sigma_{nmin}}{2} \tag{3.3}$$

$$\sigma_{nmean} = \frac{\sigma_{nmax} + \sigma_{nmin}}{2} \tag{3.4}$$
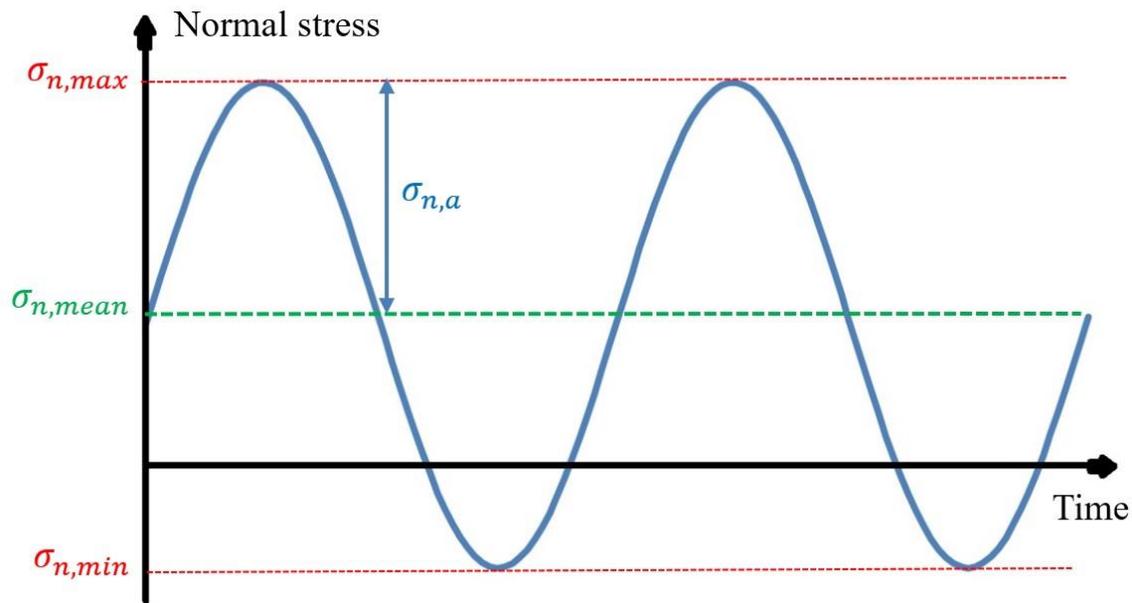
Figure 3.6. Characterization of the normal stress values.

3.2.3 Definition of the shear stress

It is also possible to characterize the shear stress by its maximal value, minimal value, mean value or amplitude. However, it is more complicated to determine them due to the two-dimensional state of the shear component, as already shown in Fig. (3.5). It is possible to define a new basis in the material plane and to project the two components of the shear vector on the axes of this basis. Then, the maximal shear stress value can be taken as the maximal one between the two components. But using this formulation clearly assumes that not every information is taken into account for the shear stress definition. Some methods have hence been developed to provide more accurate results. The most popular method, widely used for multiaxial fatigue studies to compute the value of the shear stress is the minimum circumscribed circle method (MCC), which was first proposed by Papadoupolus [62]. The idea is to find the circle with the minimum radius which surrounds all the points of the loading trajectory. This method is iterative, starting with the choice of a small radius and an initial center for the circle, and ending when reaching convergence. However other alternative methods emerge to compute the shear stress amplitude, like the highest string [63], or the minimum ellipse [64], each one possessing its own advantages. In this study, the Maximum rectangular Hull (MRH) method has been used, being revealed that it could provide better results for the fretting fatigue loading configuration [65].

The MRH concept is to generate several rectangle hulls which surround the loading trajectory using a rotary step angle φ. Every rectangular Hull can be defined by its halves sides a_1 and a_2 which gives quantities for the shear stress in two axes of the material plane. Then, the shear stress amplitude, τ_a, is defined as the maximization of the square root of both squared halves sides, and the corresponding rectangular hull is called the Maximum Rectangular Hull (Fig. 3.7). In this work, a step of 5°, has been chosen to rotate the angle φ, so that about 72 rectangular were compared.

$$a_i(\varphi) = \frac{1}{2}\left[\max_t \tau_i(\varphi, t) - \min_t \tau_i(\varphi, t)\right] \tag{3.5}$$

$$\tau_a = \max_\varphi \sqrt{a_1^2(\varphi) + a_2^2(\varphi)} \tag{3.6}$$
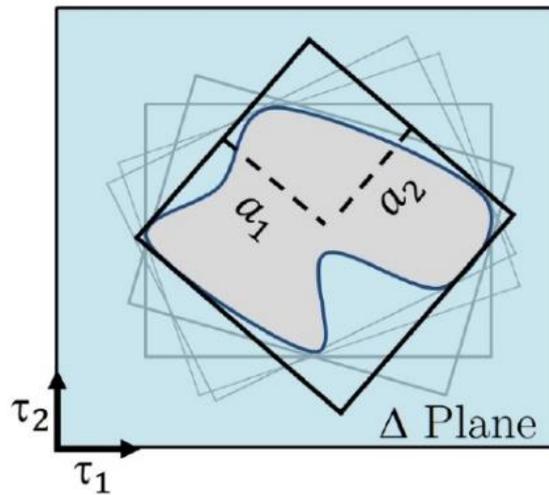
Figure 3.7. MRH method to compute the shear stress amplitude.

3.2.4 Multiaxial criteria

Several criteria have been developed based on the critical plane approach, differing in the way to find the critical plane and to express the material constants. For instance, the Findley criterion [66], established in 1957, consists in finding the plane where the combination of values of shear stress amplitude and maximal normal stress is higher, while the Matake criterion [67,68], developed in 1977, states that the critical plane is the one where the shear stress amplitude is maximal. Criteria are usually written as a relation between the driving stresses (σ_{na}, τ_a) and parameters that consider the fatigue limits of materials. Three criteria have been employed in this work, to evaluate which stresses describe better the behavior of a specimen in the presence of a phase angle between the fretting load and the bulk load. One stating that the normal stress contribution is sufficient to predict the crack behavior, another one assuming that the shear stress is

the main parameter leading to crack nucleation, and a last one considering that both stresses must be taken into account.

Smith-Watson-Topper criterion

The Smith-Watson-Topper (SWT) criterion [69] was developed to estimate lives of materials failing by the mode I crack growth. It usually gives good results for non-ductile materials under both proportional or non-proportional loadings [70]. The SWT relation considers both cyclic strain and stress:

$$\sigma_{nmax} \frac{\Delta \varepsilon_1}{2} = \frac{\sigma'_f}{E}(2N_f)^{2b} + \sigma'_f \varepsilon'_f (2N_f)^{b+c} \tag{3.7}$$

The left side of the equation, $\sigma_{nmax} \frac{\Delta \varepsilon_1}{2}$, is the so-called SWT parameter that permits to estimate the fatigue life. Considering only elastic regime and looking to the stress values calculated with the critical plane method, this parameter has been rewritten:

$$SWT = \sigma_{n,max} \left(\frac{\sigma_{n,amp}}{E} \right) \tag{3.8}$$

The methodology employed in this work to estimate the fatigue life with this criterion uses an equation developed at the University of Brasilia [71], based on experimental and numerical results. Fatigue tests have been conducted at different stress levels, and the corresponding SWT parameter of each level has been calculated using a finite element model together with the critical plane method. The results can be presented in a log-log graph as shown in Fig. (3.8), and the relation between the SWT parameter and life can be expressed as a simple power law:

$$SWT = A_{swt} N^{b_{SWT}} \tag{3.9}$$

Where A_{swt} and b_{SWT} are material parameters, the associated indexes serving to differentiate them from other parameters used in this work. Finally, the estimated fatigue life is given by the following equation:

$$N_{est,SWT} = e^{\frac{\ln\left(\frac{SWT}{A_{SWT}}\right)}{b_{SWT}}} \tag{3.10}$$
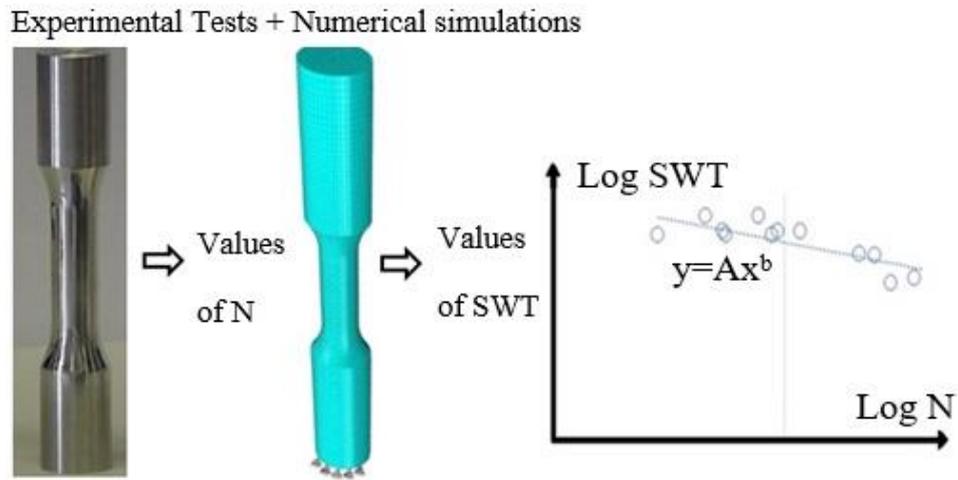
Figure 3.8. Methodology used to estimate the fatigue life with the SWT criterion.

Fatemi-Socie criterion

This second criterion developed by Fatemi and Socie [72], inspired by the findings of Brown and Miller [73], suggests that the normal stress reduces the surfaces irregularities of a micro-crack, which decreases the friction between surfaces and brings the work of the shear strain primordial. This model provides good results for materials where the nucleation step consumes the majority of the material life. The modification brought by Fatemi and Socie consists in introducing a normal stress value in the model to take into consideration the hardening that could occur in non-proportional loading. The relation is given as follows:

$$\Delta\gamma_{max}\left(1 + k\frac{\sigma_{n,max}}{\sigma_y}\right) = \frac{\tau'_f}{G}(2N_f)^{b_0} + \gamma'_f(2N_f)^{c_0} \tag{3.11}$$

The left side of the equation is the so-called FS parameter which, using the values of the driving stress and, considering the regime elastic, can be rewritten as:

$$FS = \frac{\tau_a}{G}\left(1 + k\frac{\sigma_{n,max}}{\sigma_y}\right) \tag{3.12}$$

where G is the shear modulus of the material, σ_y its yield stress and k is a constant obtained from uniaxial and torsional fatigue tests. As for the SWT parameter, simulations have been carried-out at the University of Brasilia to calculate the FS parameters corresponding to the different stress levels of a S-N curve. Eq. (3.13) is the output of that analysis:

$$FS = A_{FS}N^{b_{FS}}$$ (3.13)

leading to the Eq. (3.14) the relation used in this work for estimation:

$$N_{est,FS} = e^{\frac{\ln\left(\frac{FS}{A_{FS}}\right)}{b_{FS}}}$$ (3.14)

Modified Wöhler Curve Method

The third criterion used in this study to estimate the fatigue life with the critical plane approach is the modified Wöhler curve method (MWCM) [74-76]. This criterion suggests that the fatigue damage must be predicted using both micro and macro cracks behavior. However, these hypotheses consider the actual morphology of the material, which turns out to be complex. Some approximation must have been introduced to describe both crack initiation and propagation, like assuming a linear elastic regime and a homogeneous material. The crack nucleation is characterized by the convergence of sliding bands into a starting point for the propagation. This initial process is often driven by shear stress. After reaching a certain size, crack growth is driven by the normal stress.

The methodology consists in evaluating a stress ratio $(\rho = \sigma_{nmax}/\tau_a)$ at the material point where the crack is supposed to nucleate, and to interpolate two reference fatigue curves for which this ratio is known. Indeed, for some reference loadings, the stress ratio can be identified by analyzing the Mohr circle as shown in Fig (3.9).
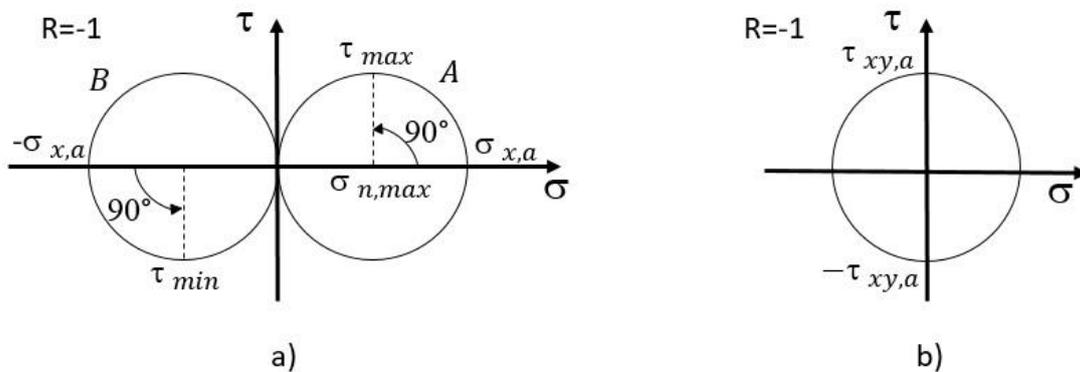
Figure 3.9. Mohr circle corresponding to a) fully reversed uniaxial loading (R=-1), and b) fully reversed torsional loading (R=-1)

32

For the fully reversed uniaxial loading, the circle "A" represents the maximum load applied, while the circle "B" represents the minimum load applied, giving the following values for the stress components:

$$\tau_a = \frac{\sigma_{x,a}}{2} \tag{3.15}$$

$$\sigma_{n,a} = \frac{\sigma_{x,a}}{2} \tag{3.16}$$

$$\sigma_{n,m} = 0 \tag{3.17}$$

Hence, the stress ratio, ρ, for fully reversed uniaxial loading is equal to 1. Furthermore, Susmel [74] shows that the stress ratio, for uniaxial loadings, can be calculated for a given load ratio R ($\sigma_{n,min}/\sigma_{n,max}$), using the following equation:

$$\rho = \frac{2}{1-R} \tag{3.18}$$

Concerning the fully reversed torsional loading, the Mohr circle analysis gives the following stress components:

$$\tau_a = \tau_{xy,a} \tag{3.18}$$

$$\sigma_{n,a} = \sigma_{n,m} = 0 \tag{3.19}$$

Resulting in a stress ratio ρ equal to zero.

Once the fatigue curve available for the studied material have been selected, the modified Wöhler diagram can be established. It consists in a log-log diagram of the shear stress amplitude as function of the number of cycles, where the values of the inverse slope κ, and the reference shear stress amplitude $\tau_{a,ref}$, that corresponds to an appropriate number of cycle N_a, can be easily obtained as shown in Fig. (3.10).
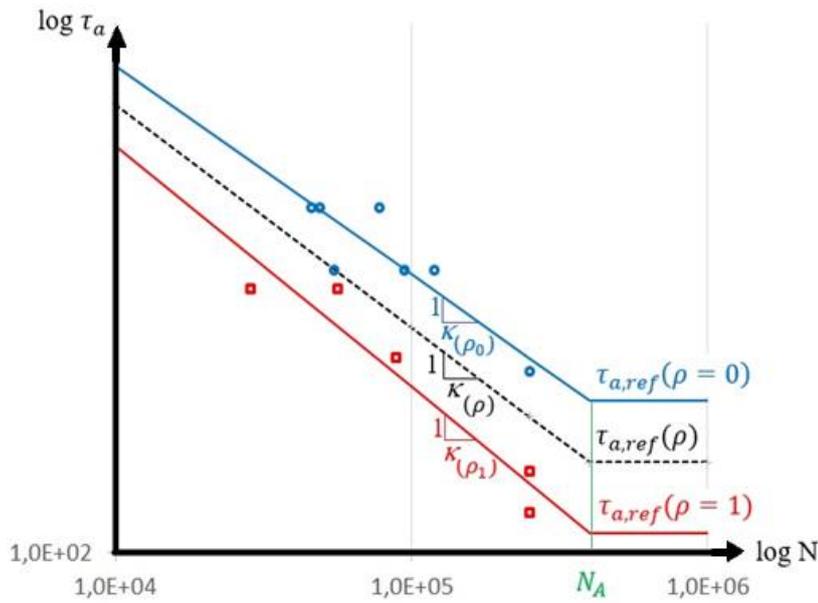
Figure 3.10. Modified Wöhler Curve diagram, with the interpolation of referential curve obtained under fully reversed uniaxial loading ($\rho=1$) and fully reversed torsional loading ($\rho=0$), to estimate the fatigue life in the process zone characterized by a stress ratio ρ.

Linear interpolation of the material reference curves for the stress ratio, ρ, allows the determination of an intermediate curve representing the study case. Therefore, the estimation of the fatigue life is obtained as follow:

$$N_{est,MWCM} = N_A \left(\frac{\tau_{a,ref}(\rho)}{\tau_a} \right)^{\kappa(\rho)} \tag{3.20}$$

3.3 Stress gradient problem

As it also happens to components containing geometrical discontinuities, the fretting fatigue configuration is characterized by the presence of a stress concentration at the surface which rapidly decays over depth as explain in section 3.1.1. In such configuration, the elastic stress doesn't reach values as high as those predicted by the continuum mechanic theory. As consequence, the critical plane criteria (described in section 3.2) cannot be directly applied to a material point of the surface. In order to correctly estimate fatigue strength, it is necessary to calculate an effective stress representative of the real stress damaging the fatigue zone. Once the location of this effective stress is defined, a critical plane criterion can be applied.

3.3.1 Theory of critical distance

The so-called theory of critical distance emerged in the late 1950's from Neuber [77] works in Germany, and from Peterson [78] works in the United States of America, to predict fatigue failure of metallic structures under high stress gradients by studying notched specimens. Neuber first proposed to average the stresses along a line originated at the notch tip and ending at a "critical distance". Peterson suggests that the effective stress can be related to a certain distance of the stress gradient apex. These two formulations of the critical distance, respectively called the line method (LM) and the point method (PM), were widely used in the 60's, for the fatigue life prediction of brittle metals, and complementary studies come to reinforce the theory of critical distances. Indeed, the effect of hole size, notch length and other geometries discontinuities on the fatigue life, have been investigate through this method. A third formulation of the critical distance, known as the area method (AM), which considers that stresses must be averaged on a semi-circular area in the vicinity of the stress concentration, was presented by Taylor [79].

Using the linear elastic fracture mechanics together with the formulations established by their predecessors [77,78], Whitney & Nuismer [80] manage to express the critical distance as function of the fracture toughness, *Kc*. This works opens the door to the classification of the critical distance as a material parameter. The well-known El Haddad equation [81], that expresses the critical distance in function of the threshold intensity factor and the fatigue limit of the material was developed in 1979 and used in many studies. It states that:

$$L = \frac{1}{\pi}\left(\frac{\Delta K_{th}}{\sigma_0}\right)^2 \tag{3.21}$$

Since the stresses are well located in a fretting fatigue configuration, and that the failure always occurrs at the edges of the contact zone, the theory of critical distance seems appropriate for the study. The point method formulation has been selected in this work, applying the critical plane criteria at certain distance from the surface, and at the edge of the contact. Figure (3.11) shows the processing point *L*, according to the fretting fatigue stress gradient, its value remaining to be determined.
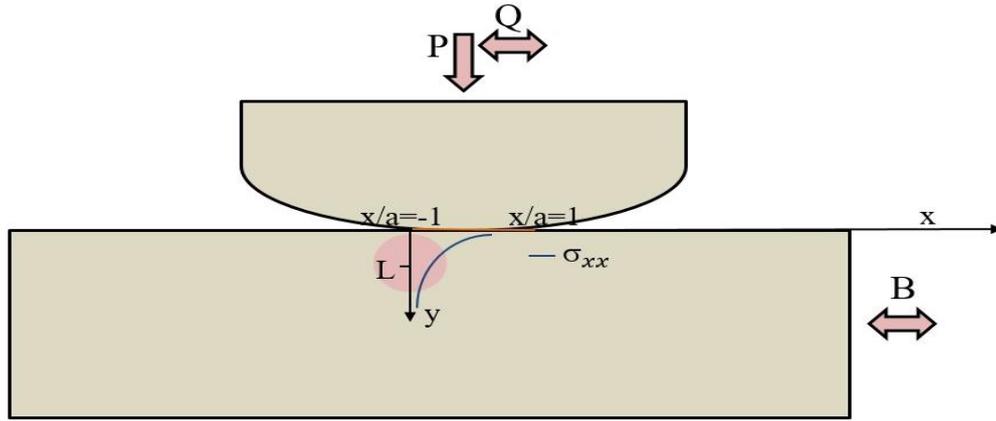
Figure 3.11. Theory of the critical distance, with the point method formulation applied to the fretting fatigue configuration.

3.3.2 LvsN calibration with material parameters

As suggest by Eq.(2.21), the material characteristic length, L, must change with the number of cycles to failure, N. Susmel & Taylor [82] proposed a methodology to express the critical distance in function of the material life, dividing Eq. (3.21) in two distinct cases. For the static case, where material has broken without cycling, the critical distance is function of the ultimate yield stress and the fracture toughness, while for the dynamic case, where material has reached a number of cycle, N_0, without breaking, the critical distance is function of the stress intensity factor threshold and the fatigue limit σ_0.

$$L_s = \frac{1}{\pi}\left(\frac{K_{IC}}{\sigma_{UTS}}\right)^2 \tag{3.22}$$

$$L_{N_0} = \frac{1}{\pi}\left(\frac{\Delta K_{th}}{\sigma_0}\right)^2 \tag{3.23}$$

Considering the Wöhler curve of a given material, σ_{UTS} and σ_0 are correlated to a number of cycles N. Using the material length, L, as ordinate axe instead of the stress value in the log-log diagram, permits to obtain a relation between the life and the critical distance (Fig. 3.12). Thus, the intermediate values between the static case and the fatigue limit case can be found.
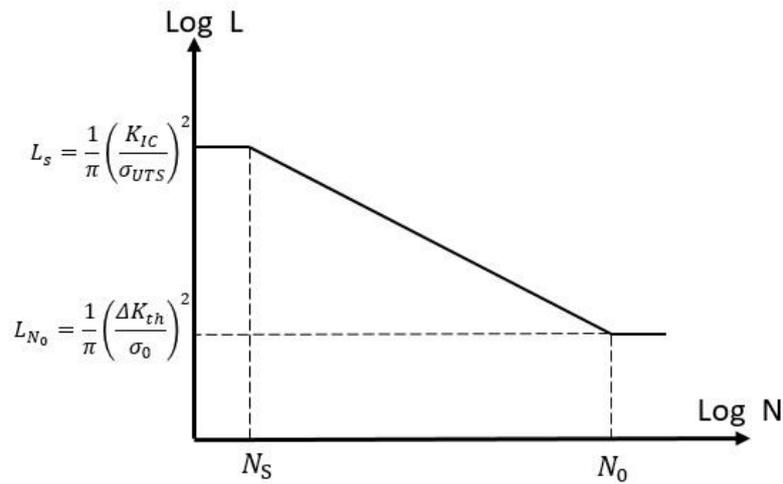
Figure 3.12. Calibration of the LvsN equation using static and dynamic parameter of the material.

As in a log-log diagram, the relationship is given by a simple power law, for any intermediate value, the critical distance can be written as follow:

$$L = AN^b \tag{3.24}$$

where A and b turns material parameters that depend on the yield stress, the fatigue limit, the fracture toughness and the threshold intensity factor of the material.

3.3.3 LvsN calibration using notched specimens

In order to determine the value of the critical distance, experimental data and numerical analysis have been used [71]. Tests have been conducted on V-notched type specimens, whose geometry gives rise to a similar stress gradient that the one obtain in fretting fatigue. The idea is to associate the experimental life (Fig. 3.13a) to an effective stress value using the S-N curve (Fig. 3.13b). A finite element model is then used to identify at which distance from the surface, this stress occurs (Fig. 3.13c). As the power law relationship is linear in a log-log graph (Fig. 3.13d), repeating the operation for two different loading levels is sufficient to obtain two distances associated to two experimental lives and establish a relationship. However, it might be interesting to repeat this process for additional stress levels, to get more consistent power law parameters.
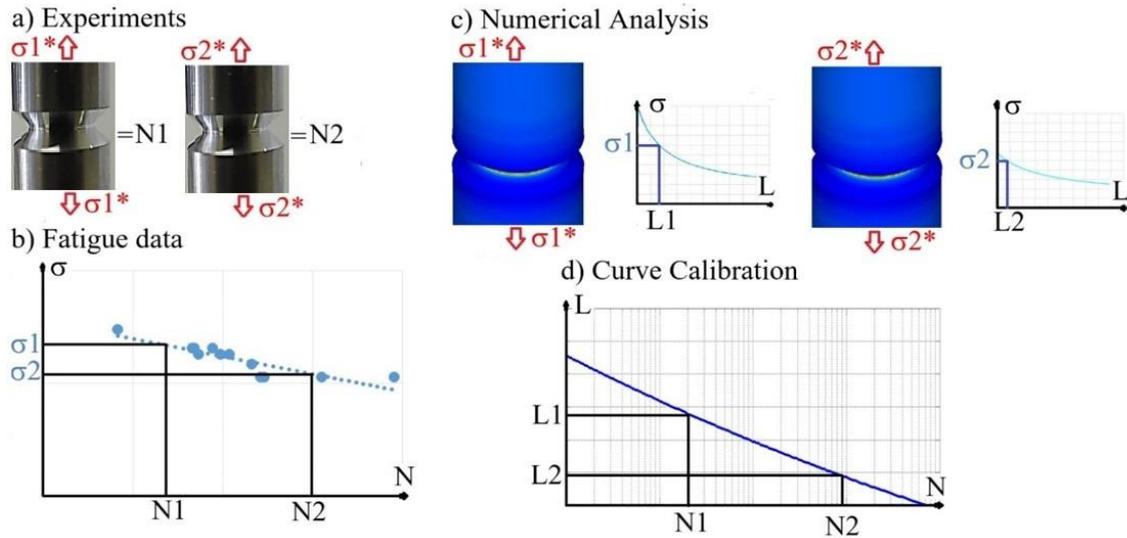
Figure 3.13. Methodology for calibration of a LvsN curve with notched specimens, a) experimental tests, b) identification of the effective stress, c) evaluation of the critical distance using FEM, and d) calibration.

Note that this method, can be applied for different loading types, which may be interesting when investigating a complex multiaxial condition. In his works, Sá [71] conducted tests on notched specimen made of 7050 T7451 aluminum alloy, under fully reversed uniaxial and fully reversed torsional loading conditions, for which he also provides the S-N material curves. As an outcome, two equations have been developed:

$$L_\sigma = A_\sigma N_f^{b_\sigma} \tag{3.25}$$

$$L_\tau = A_\tau N_f^{b_\tau} \tag{3.26}$$

where A_σ and b_σ are material parameters obtained for uniaxial reversed loading and A_τ and b_τ are material parameters obtained for torsional reversed loading. As the stresses in fretting fatigue are multiaxial in nature, (3.25) and (3.26) can be used to determine the critical distance L, for fatigue life estimation. Nevertheless, a third relation, which introduces an equivalent critical distance, L_{eq}, that takes into account these two reference loadings is favored in this work:

$$L_{eq} = \omega_\sigma L_\sigma + \omega_\tau L_\tau \tag{3.27}$$

where ω_σ and ω_τ are coefficient that permit to balance the weight of the L_σ and L_τ. As example for the life prediction of notched specimens [83], the use of L_σ gave over-estimated results, while L_τ gave under-estimated results. In this way, the use of L_{eq}, with appropriated weight ω_σ and ω_τ, could have given a correct fatigue life estimation.

3.3.4 Iterative method

Once the LvsN equations have been established, two ways to identify the critical distance and the stress point becomes available. Using the power laws, Eq.s (3.25-3.27), the critical distance, *L*, can be calculated according to the experimental life, *N*. However, it is necessary to know the magnitude of the fatigue life before conducting the tests. This avoids overly short lives, corresponding to the low cycle fatigue regime, where unwanted plastic deformations can be observed due to the high stress levels. It is also necessary to avoid reaching the number of cycle associated to the fatigue life beyond which it is considerate that the material will never break (*run out*). In this work, a fatigue life of approximately 10^5 cycles is targeted.

An iterative scheme [84], was used to predict the fatigue life of materials. The stresses are first evaluated over a straight line that emanates from the contact edge and is perpendicular to the contact surface. The critical plane method is applied at every single point of this line (using a step of 10μm between points) to calculate the shear stress amplitude and maximal normal stress. The expected number of cycles to failure, N_0, is set before initializing the iterative process, and the associated critical distance is calculated using a power law equation. The fatigue life, N_{fe}, is estimated at the distance *L* using Eq. (3.20) with the stress values τ_a, $\sigma_{n,max}$, and ρ calculated at this point. It has been chosen to use this equation, due to the fact that the MWCM shall be the most efficient multiaxial criterion, as its takes into account both shear and normal stresses for life prediction. If the estimated life, N_{fe}, differs from the hypothetic life, N_0, a new iteration starts, as depicted in Fig. (3.14). The process is repeated until convergence is achieved.
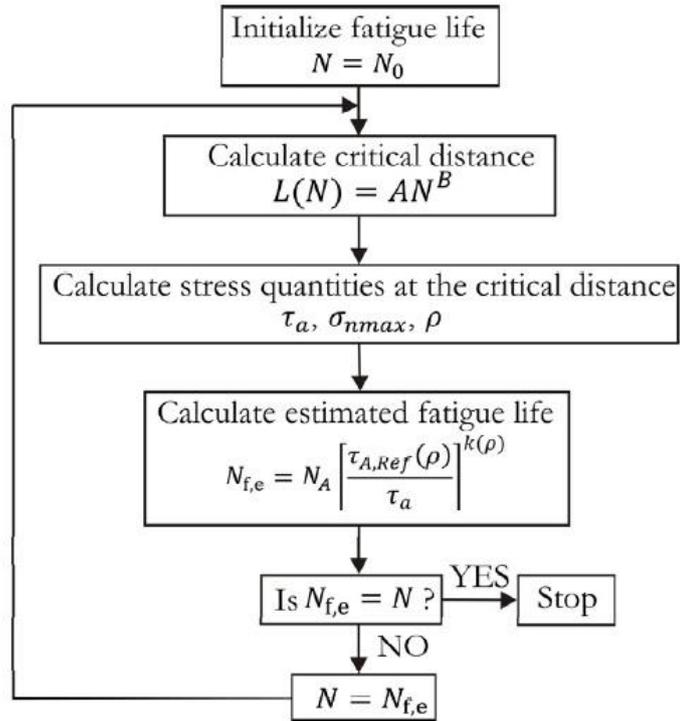
Figure 3.14. Iterative process to predict the fatigue life [84].

Chapter 4. Methodology

In this chapter, the materials and specimens used are presented. The testing system is described and the experimental procedure for introduction of a phase angle between the fretting and the fatigue loads is detailed. The numerical model and an overview of the finite element method used in this work is given. Lastly, the methods for failure analysis are presented.

4.1 Materials

In this work, two distinct materials were chosen: The 7050-T7451 aluminum alloy (further denoted as *Al7050*) and the ATSM 754 CA6NM stainless steel (*CA6NM*).

4.1.1 Al7050 T7451

As already mentioned in Section 1.1, the excellent set of properties of this material, made it a suitable candidate for this study (Tab 4.1). The Al7050 presents in its chemical composition aluminum, zinc, copper and magnesium among other elements. The main element of 7th series aluminum alloy is the zinc, and it has no impurity beyond the natural limit. The complete chemical composition is given in Tab. (4.2). The typical microstructure of the alloy Al7050 (Fig. 4.1), is made of small grains obtained by the recrystallization of the heat treatment that have an average size of about $8\mu m^2$ [86]. The large and clear areas are coarse grains corresponding to the non-recrystallized regions.

Table 4.1 –Mechanical properties of the 7050-T7451 alloy [85].

Mechanical property	Values
Yield limit, σ_y (MPa)	453.8±2.8
Ultimate tensile strength, σ_u (MPa)	513.3±4.1
Elastic modulus, E (MPa)	73.4±2.0
Elongation (%)	11.1±0.6
Microhardness, HV	153.6±2.6
Poisson's coefficient, υ	0.33

Table 4.2 – Nominal chemical composition of the Al7050, wt (%).

	Zn	Ti	Mg	Cu	Zr	Fe	Mn	Cr	Si
AMS Norm	5.7-6.7	0.06	1.9-2.6	2.0-2.6	0.10-0.16	0.15	0.009	0.006	0.12
University of Brasilia	6.75	0.03	2.31	2.65	0.12	0.05	<0.01	<0.01	0.02

Figure 4.1. Microstructure of the Al7050 [71].

This aluminum alloy has been subjected to heat treatment, in order to control its specific characteristics. It has been solubilized and stabilized, bringing it beyond the point of maximum mechanical resistance. In the case of the T7451 heat treatment, the alloy endured a quick cooling followed a double artificial aging. Figure (4.2) illustrates the heat treatment performed.
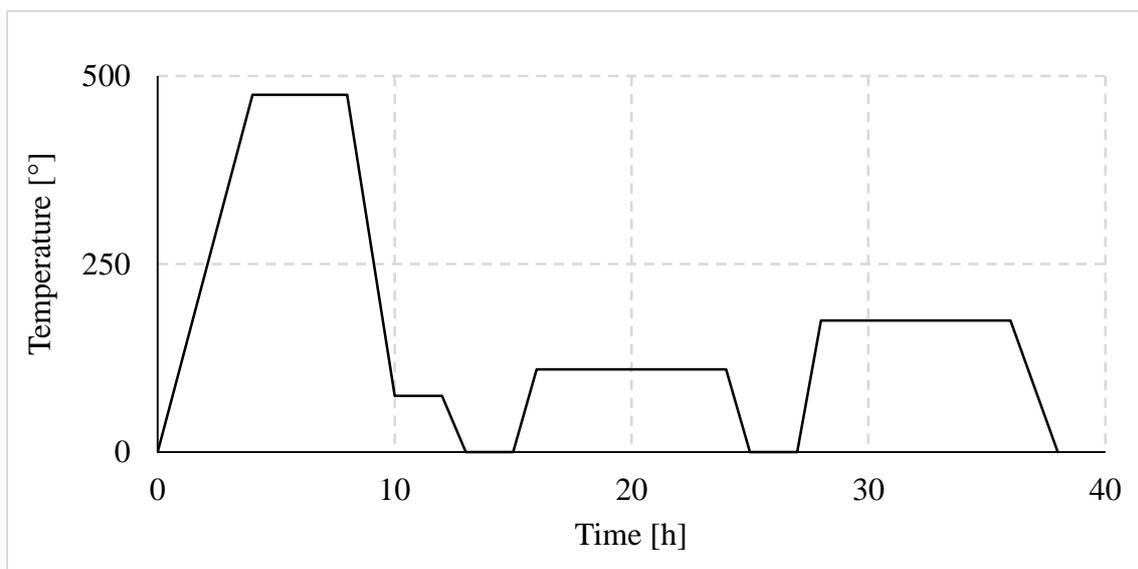
Figure 4.2. Heat treatment of the 7050-T7451 Aluminum alloy.

The fatigue behavior of the Al7050 must be known for the application of the methods proposed in Chapter 3. In this sense, tests were performed on smooth specimens, under fully reversed uniaxial loading and under fully reversed torsional loadings. Specimens dimensions, tolerances and manufacturing conditions have been defined according to ASTM E606 [87]. Seventeen specimens have been tested under uniaxial condition, while twelve have been tested under torsional condition. Five to six stress levels were investigated for each loading condition, and lives varies from 10^4 cycles to the fatigue limit of the material, 10^7 (Fig. 4.3).
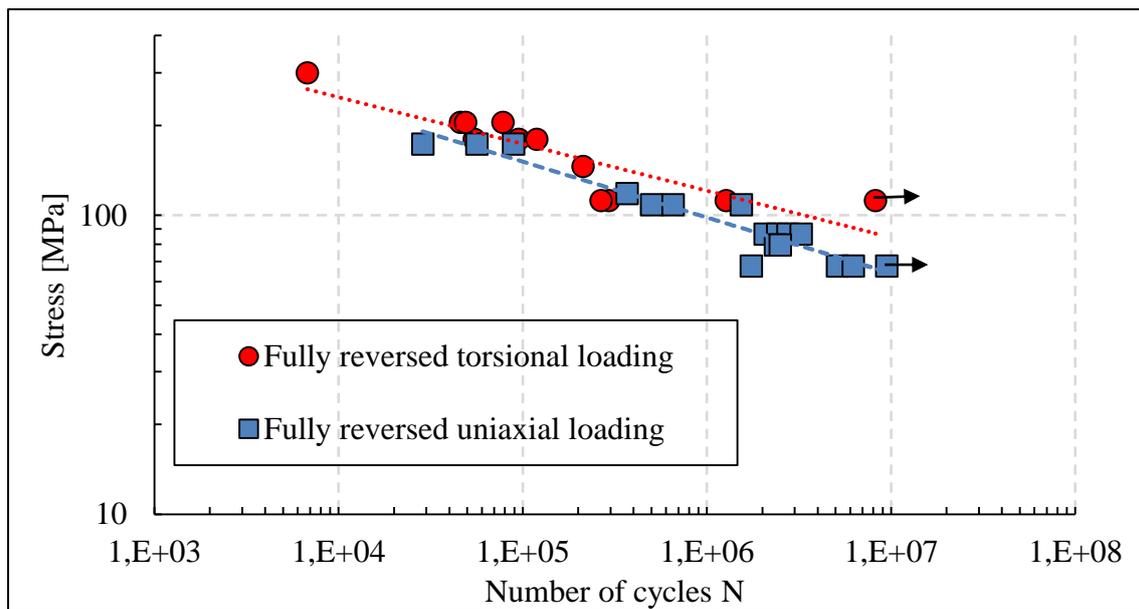
Figure 4.3. S-N curve of the 7050 T7451 under fully reversed uniaxial and fully reversed torsional loadings [71].

4.1.2 ASTM 743 CA6NM

According to ASTM international [88], the CA6NM is a low-carbon martensitic steel, that is offset with addition of nickel, to enable complete austenitization, temper the formation of martensitic, and improve its mechanical properties [89]. In addition to microstructure of the tempered martensitic, this alloy is composed by retained austenite that can improve toughness [90] and delta ferrite that raises the ductile to brittle transition temperature [91]. Mechanical properties and chemical composition of the CA6NM stainless steel are listed in Tabs. (4.3) and (4.4) respectively, and its microstructure is shown in Fig. (4.4).

Table 4.3 – Mechanical properties of the CA6NM alloy, wt (%) [88].

Mechanical property	Values
Yield limit, σ_y (MPa)	550
Ultimate tensile strength, σ_u (MPa)	755
Elastic modulus, E (GPa)	~204
Elongation (%)	>15
Poisson's coefficient, υ	~0.3

Table 4.4 – Nominal chemical composition of the CA6NM, wt (%) [88].

	C	Mn	Si	Cr	Ni	Mo	P	S
ASTM Norm	≤0.06	≤1.0	≤1.0	11.5-14	3.5-4.5	0.4-1.0	≤0.04	≤0.03
University of Brasilia	0.05	0.67	0.52	12.94	3.21	0.4	0.036	0.01
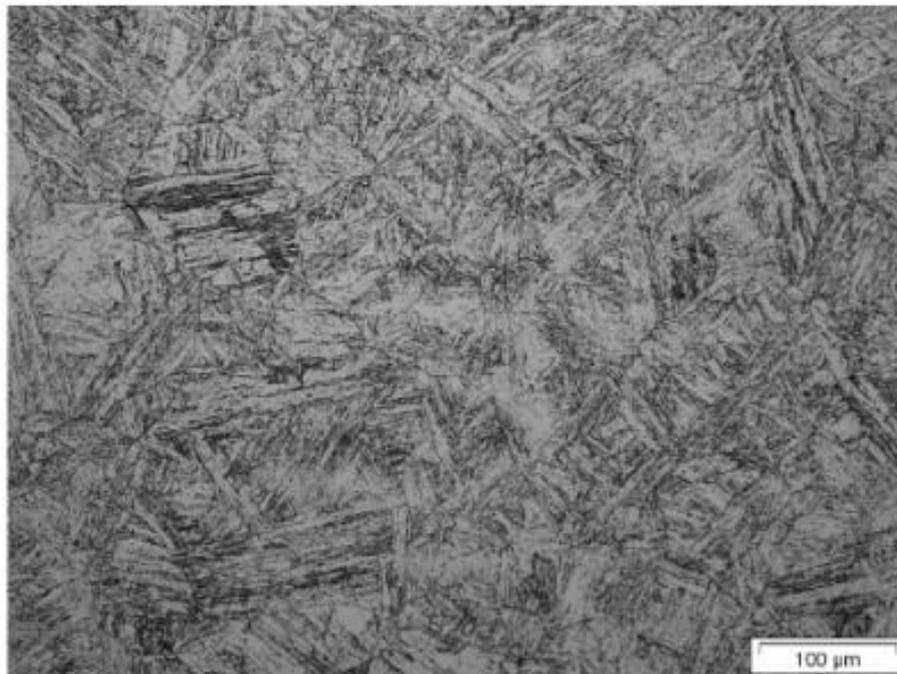
Figure 4.4. Microstructure of the A743 CA6NM stainless steel [92]

Fatigue curves under torsional loading, were not encountered in literature for this material. However, it has been possible to calibrate the critical distance using Eq's. (3.22) and (3.23), and to predict the fatigue life using the iterative process. As described in

Chapter 3, this prediction method is based on the modified Whöler curves method. To use the MWCM, two reference fatigue curves are required, but not necessary under fully reversed uniaxial and torsional loadings. In his work, Silva [93] studied the fatigue behavior of this material for various load ratio, conducting about 130 experimental tests, leading to fatigue lives going from 10^5 to 10^6 cycles. Only the S-N curves obtained with uniaxial load ratios R=0 and R=-1 (Fig. 4.5), have been used to predict the fatigue life of the CA6NM stainless steel. According to Eq. (3.18), these data give the reference curves for the stress ratios $\rho=1$ and $\rho=2$.
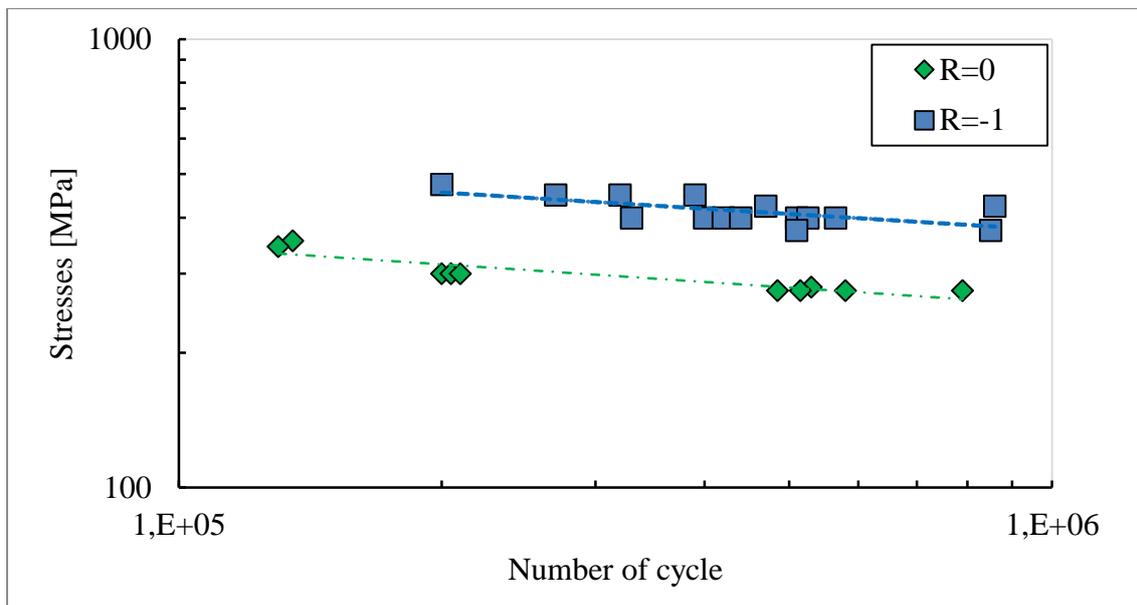
Figure 4.5. S-N curve of the Ca6NM stainless steel under uniaxial loadings [83].

4.1.3 Specimens

The specimens used during this study for the assessment of experimental life are flat "dogbone" specimens with a cross section of 13mm. Pads are cylindrical parts that ensure the cylindrical-plane contact and permit to apply the fatigue load. In this study, all pads possess a radius of 70mm. These dimensions are the same for both material of the study (Fig. 4.6). Note that this work focus on the phase angle effect, and that the contact behavior between dissimilar materials is not studied. The first experimental campaign concerns only the aluminum alloy, while complementary tests will be conducted on the stainless steel. The shape and dimension of specimens and pad for both materials are given in annex.

Figure 4.6. photograph of pad/specimen made of 7050 T7451 aluminum alloy on the top and ASTM 743 CA6NM steel on the bottom.

4.2 Experiments

In this work a servo-hydraulic system (MTS 322 test frame) coupled with a hydraulic pump, from ENERPAC systems, is employed for the experimental testing. This equipment allows the distinct control of the fretting load and of the fatigue load using two different sets of servo-hydraulic pistons while a normal pressure is kept constant using a hydraulic pump. The system is depicted in Figure 4.7. The fatigue load is applied to the specimen in the transversal direction, from the bottom actuator. The fretting apparatus, linked to the upper actuator, is made of a rolling part at the back which block the specimen in the longitudinal direction and a pad at the front which permits to ensure the cylinder-plane contact by applying the normal pressure but also the fretting load in this same direction. The bottom activator is equipped with a load cell of 250 kN, while the upper activator is equipped with a load cell of 100 kN. The MTS machine possesses a third load cell of 250 kN placed up to its top grip which permit to read the force response.
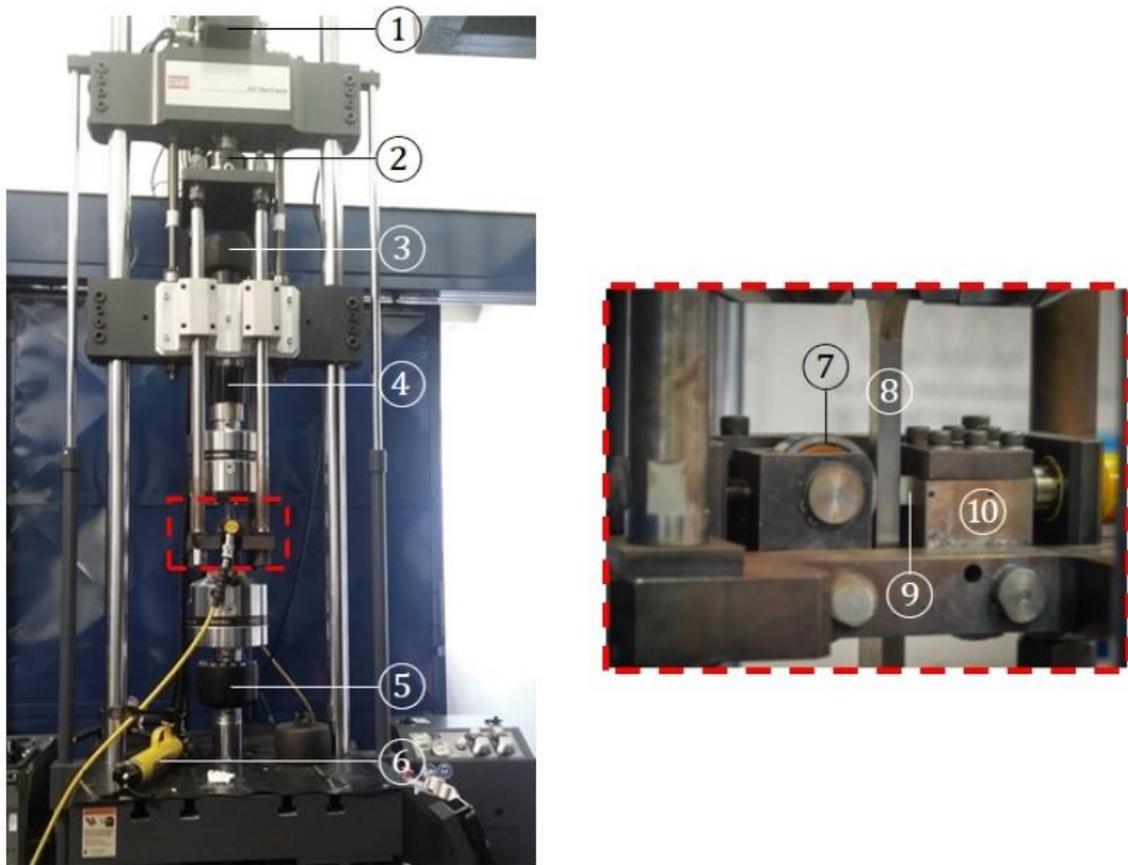
Figure 4.7. Visualization of the servo-hydraulic machine with 1) fretting load actuator; 2) ,3) ,4) load cells, 5) fatigue load actuator, 6) hydraulic pump, and detailed view of the fretting device with 7) roller, 8) specimen, 9) pad and 10) pad holder.

4.2.1 Test Set-up

The specimen is placed into the grips of the testing machine and its alignment in the longitudinal direction is checked. This verification can be done using a caliper to verify that the position of the specimen is the same in both grips. When correctly aligned, a pressure of 100 bars is applied by the grips to firmly hold the specimen in the vertical direction during the test.

The next step is to align the cylindrical pad with the "dogbone" specimen before applying the normal pressure. The hydraulic pump induces a force on a piston (effective area of $640mm^2$, maximal capacity of 700 bars) and is manually set to the desired pressure using a manometer. An accumulator is mounted together with the pump in order to maintain pressure during the fretting fatigue tests. Despite bringing necessary stability to correctly conduct experiments, the accumulator limits the maximal pressure to 350 bars, so that the maximal normal load, P, available for a fretting fatigue test is 22kN. However, this value is more than enough for the loads applied in this work. The hydraulic system is depicted in Figure 4.8.

47
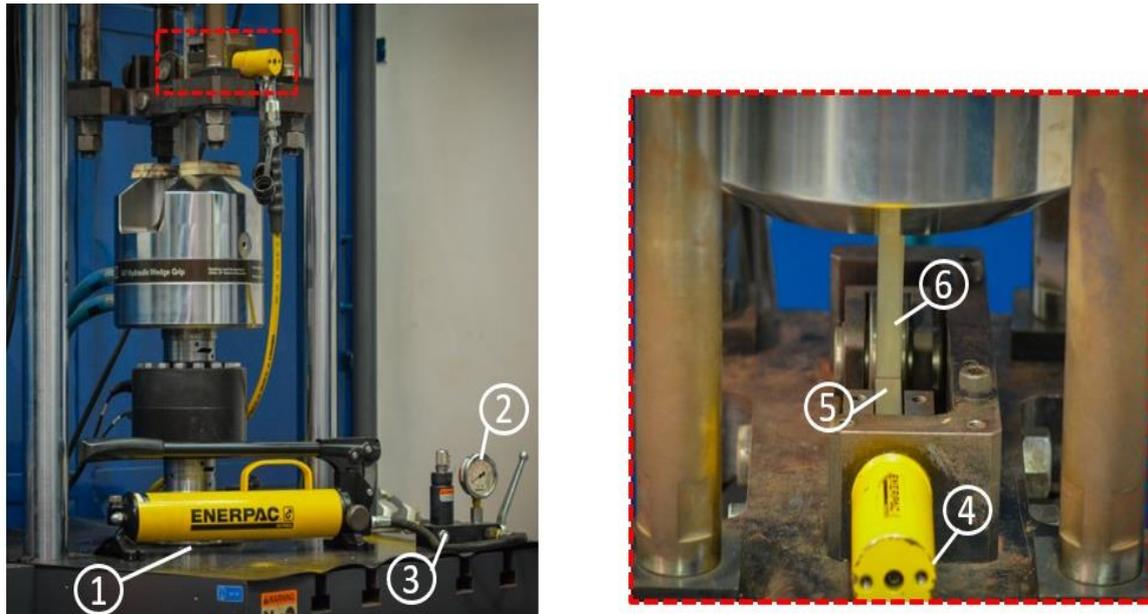
Figure 4.8. Visualization of 1) hydraulic pump, 2) manometer, 3) accumulator, 4) hydraulic piston, 5) pad and 6) specimen.

The alignment between pad and specimen must be meticulous as it is primordial to ensure the uniform propagation of cracks during the fatigue process. It is important to firstly establish the mean force of the bulk load, as its application could undo the alignment. However, in this work, the mean stress is set to zero, which makes the alignment procedure easier.

The contact between the curved part of the pad and the plane surface of the specimen must result in a straight and uniform thick line. A measuring film is placed in the interface such that when the normal pressure is applied a line is drawn. Figure 4.9 describes the adjustments required to the pad holder and the procedure to obtain a good alignment. Four screws are used to adjust the pad position. The two back screws permit to adjust the pad inclination while the two front screws ensure that the contact is established from one side of the specimen to the other. The alignment screws must be adjusted and readjusted until alignment is achieved. At this point, it is recommended to tight the screws progressively, one by one, and with a normal pressure applied to maintain the alignment.
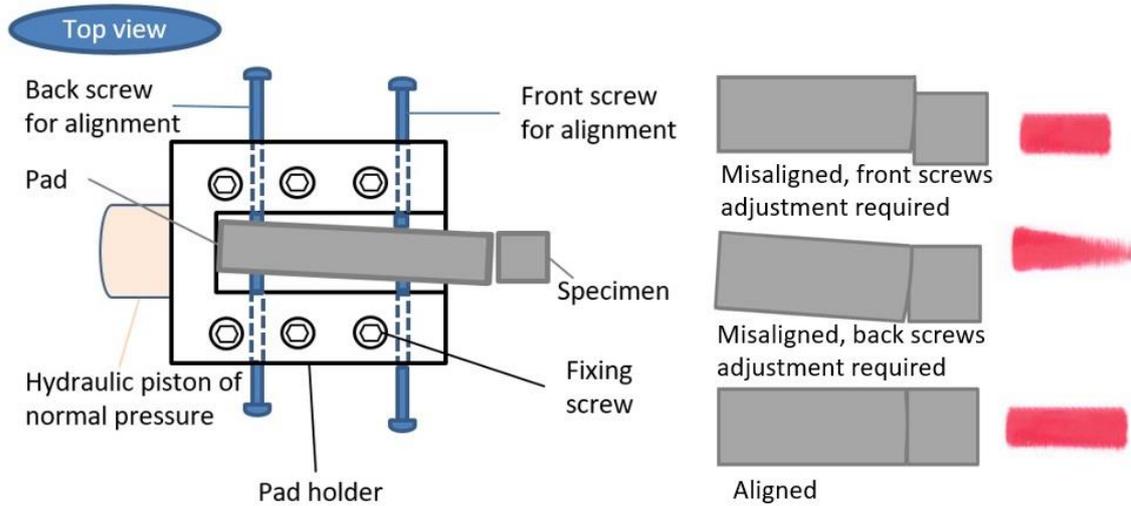
Figure 4.9. Top view of the pad holder on left and examples of wrong or good pad/specimen alignment on right.

Once the alignment between pad and specimen is established, the desired normal pressure is applied. This normal pressure remains constant during all the fretting fatigue test. In this study, a normal load, *P*, of 5.8kN (90 bar) was set for the Al7050 tests while a load equal to 16kN (250 bar) is employed in the CA6NM tests. Note that using Eq. (2.10), these values lead to a peak pressure of approximately 290 MPa and 790 MPa for the Al7050 and CA6NM, respectively. In this way, the regime remains elastic when testing the aluminum alloy, whereas plasticity could occur for the steel. The high Young modulus of this second material forced to apply high forces in order to get a substantial fretting mark that permit to correctly conduct fretting fatigue test without sliding.

The following step is the application of sinusoidal fretting and fatigue loads. In this study, it has been chosen to work with tangential loads of 2.3 kN and 5.5kN, and axial loads of 19.2kN and 50kN respectively for Aluminum and Steel. A representation of the effective forces during a conventional fretting fatigue test is given in Fig. (4.10) and the loads values applied during the study are presented in Tab. (4.5). Note that the fatigue load values described in Tab. (4.5) lead to a stress values of 114 MPa and 296 MPa respectively for the Al 7050 and the CA6NM.
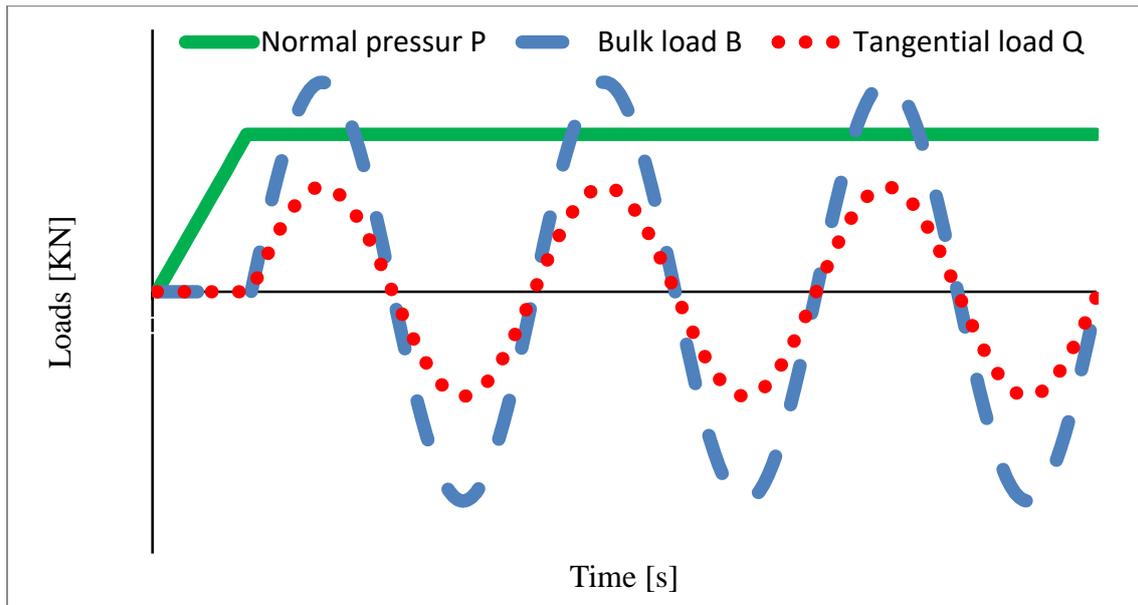
Figure 4.10 Applied loads for an in-phase fretting fatigue test.

Table 4.5 – Values of the loads applied during the study

	Normal Pressure [N]	Fretting Load [N]	Bulk Load [N]
Al7050	5800	2300	19200
CA6NM	16000	5500	50000

4.2.2 Pre-Test procedure

Some sliding problems have been encountered when conducting tests in force control mode. It is preferable to do a pre-test first in displacement control mode, in order to obtain an initial fretting mark and to achieve a stable friction coefficient. Therefore, a small displacement is applied from the upper activator and the tangential force response is read. The displacement must be raised in small increments to avoid scratches on the contact surface. As example, a step of 0.01mm has been used during these pre-tests. In between every step, it is important to wait a few cycles to permit the force stabilization and the generation of the fretting mark. The MTS basic software allows the visualization of the reaction force as function of the displacement, which is used to verify if any disturbance (such as slip) is occurring. Figure 4.11 describes the partial slip regime that must be visualized and the total slip regime to avoid. The displacement is raised until reaching the desired value of Q, discussed in the section 4.2.1. Once the fretting load is established by the displacement control mode, several cycles are performed in order to create an initial fretting mark before setting the experiment to force control mode. Less

than 5000 cycle are necessary for the tests with the Al7050 while 10000 cycles are required for the CA6NM.
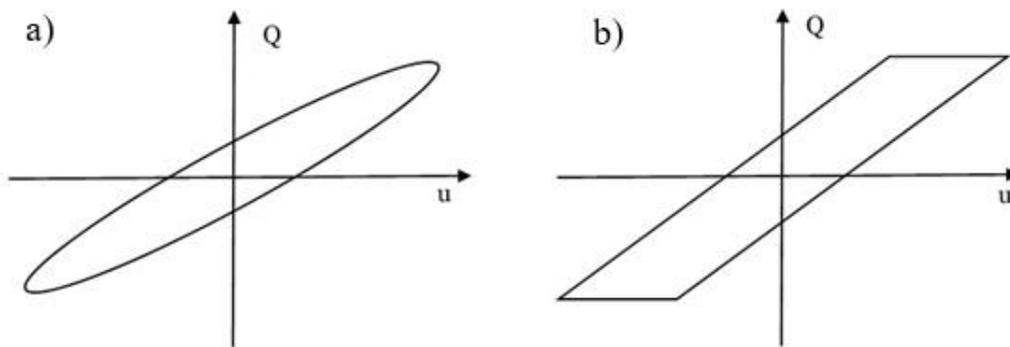
Figure 4.11 Visualization of a) a partial slip regime and b) a total slip regime, looking to the force against displacement loop.

4.2.3 Application of the phase angle

The phase angle has been applied to the fatigue load, as the bottom actuator is the one adequate to this task. Three phase angles have been investigated during this study: $\Phi=45°$, $\Phi=90°$ and $\Phi=135°$. The visualization of these out-of-phase loadings is described in Figure 4.12. For the Al7050, every phase angle was investigated and also compared with conventional in phase loading of Figure 4.10. Concerning the CA6NM stainless steel, only $\Phi=45°$ and $\Phi=135°$ loading configurations have been studied to bring complementary results. Note that, for every conducted test, the loading condition was kept as presented in Tab. 4.5.
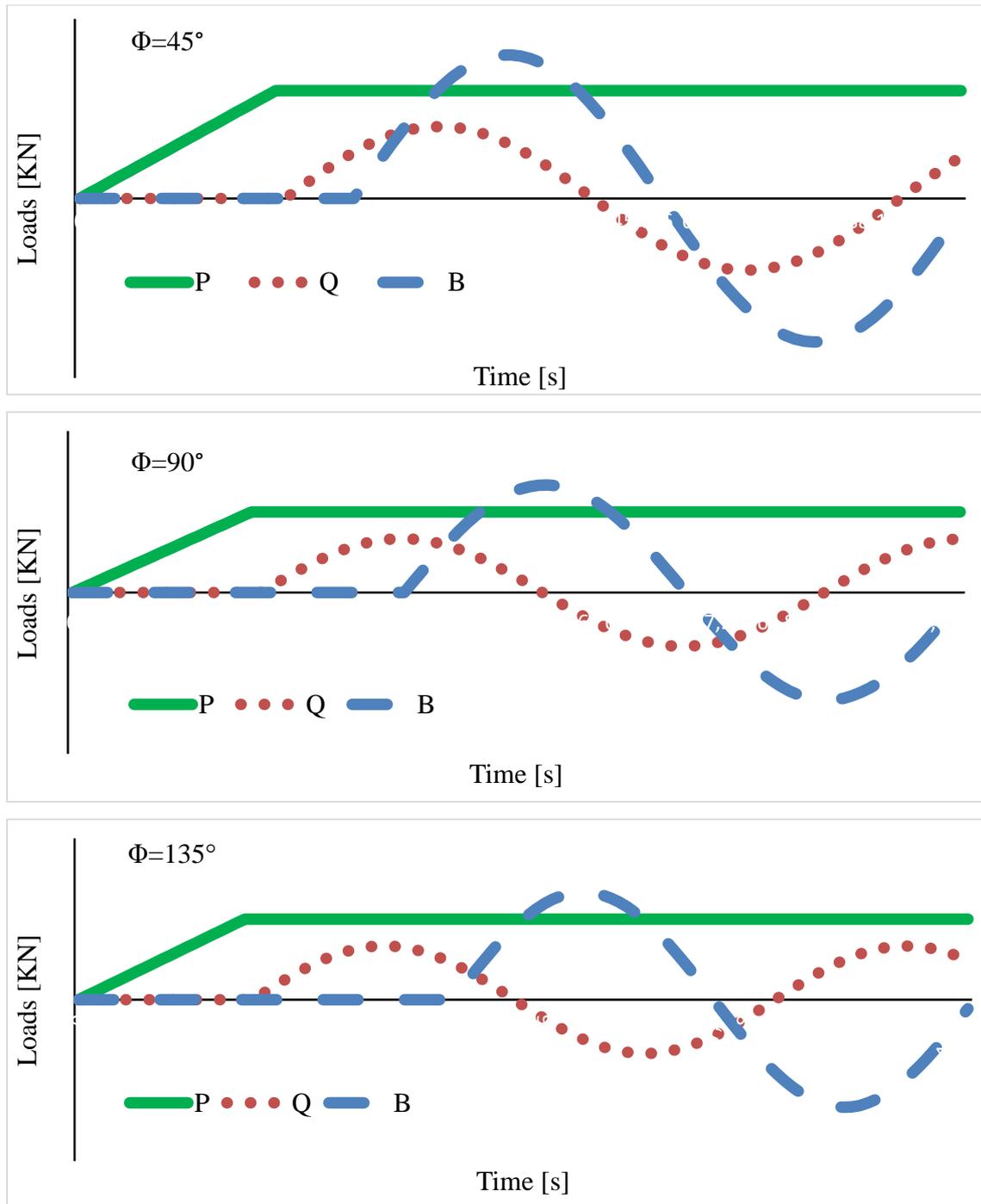
Figure 4.12 Visualization the applied loads for phase angle loadings.

Some problems have been encountered while applying phase angle between loads. It has been noted that raising the phase angle between fretting and fatigue loads produces higher displacement of the upper activator. As consequence, the frequency of tests with a high phase angle must be kept low (Fig. 4.13). Indeed, raising the phase angle while the test is running at high frequency could cause resonance phenomenon and brutal interruption of the test. Raising the frequency when the test is running with the phase

angle established, causes a misbehavior of the force response, losing the phase angle, and loads values established. Experiments have been conducted to see at which frequency the response is lost and what can be the convenient frequency for a given phase angle, the results are summarized in Figure 4.13. It has been concluded that the adequate frequencies are 8Hz, 4Hz and 2Hz for a phase angle of 45°, 90° and 135°, respectively. Additional tests were also carried-out to ensure that frequencies from 2 to 8 Hz do not influence the fatigue life. Furthermore, the CA6NM seemed less sensitive to this phenomenon. Nevertheless, for this material all tests were conducted with the same frequency, 2Hz.
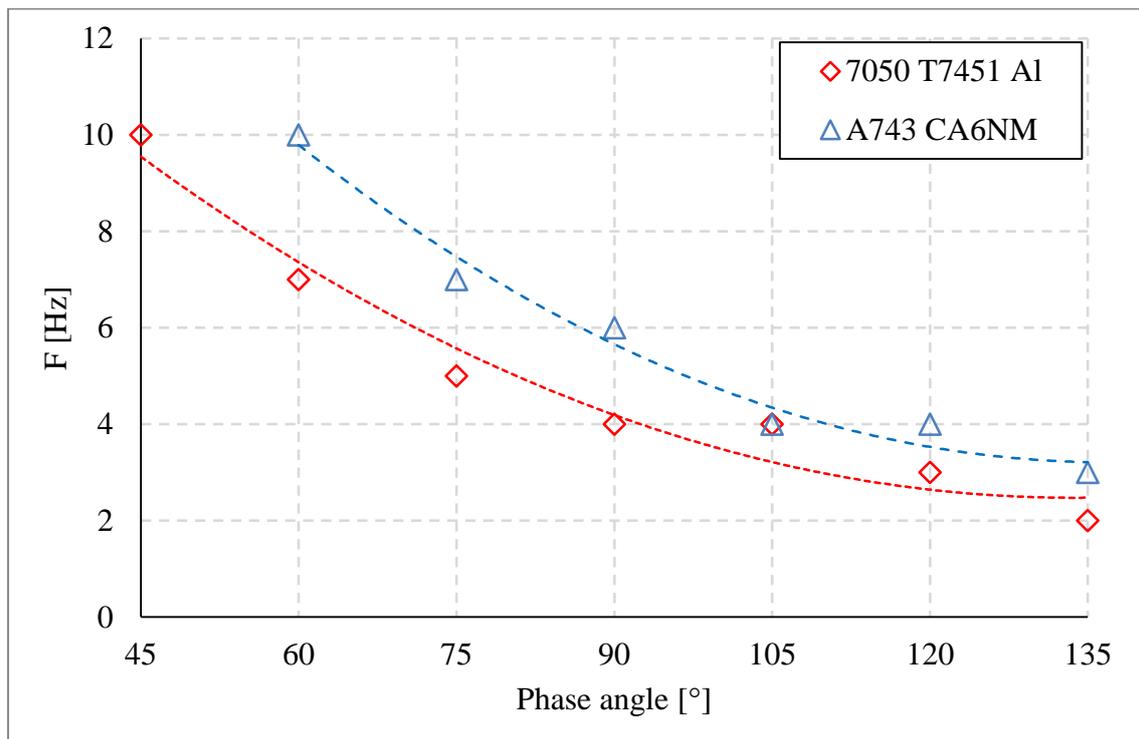
Figure 4.13 Visualization of the frequency limitation for out-of-phase fretting fatigue tests.

It is important to mention that there are two MTS compensators that permit the control of the phase angle: the phase amplitude compensator (APC) and the peak valley phase compensator (PVP). The PVP firstly seemed to be a good option as it permits to reach frequencies a little higher for out-of-phase loads (about one more Hertz than when using APC). Nonetheless, tangential and axial loads must be raised slowly and progressively to keep good force responses and avoid sliding. When raising loads, the peak valley phase compensator tends to stabilize using the maximal and minimal value of the forces as references. As consequence, higher values than those wanted for the test are reached during the stabilization, which usually lead to sliding. Hence, the amplitude phase compensator has been used in this work, as its stabilization does not induce such

overtake of force and permits to correctly establish the wanted loads of a fretting fatigue test conducted with phase angle.

The MTS TestSuite, software used in this study, employs diagram blocks for the control of the force applied by the bottom activator, the force applied by the upper activator and the eventual phase angle between them, as depicted in Figure 4.14.
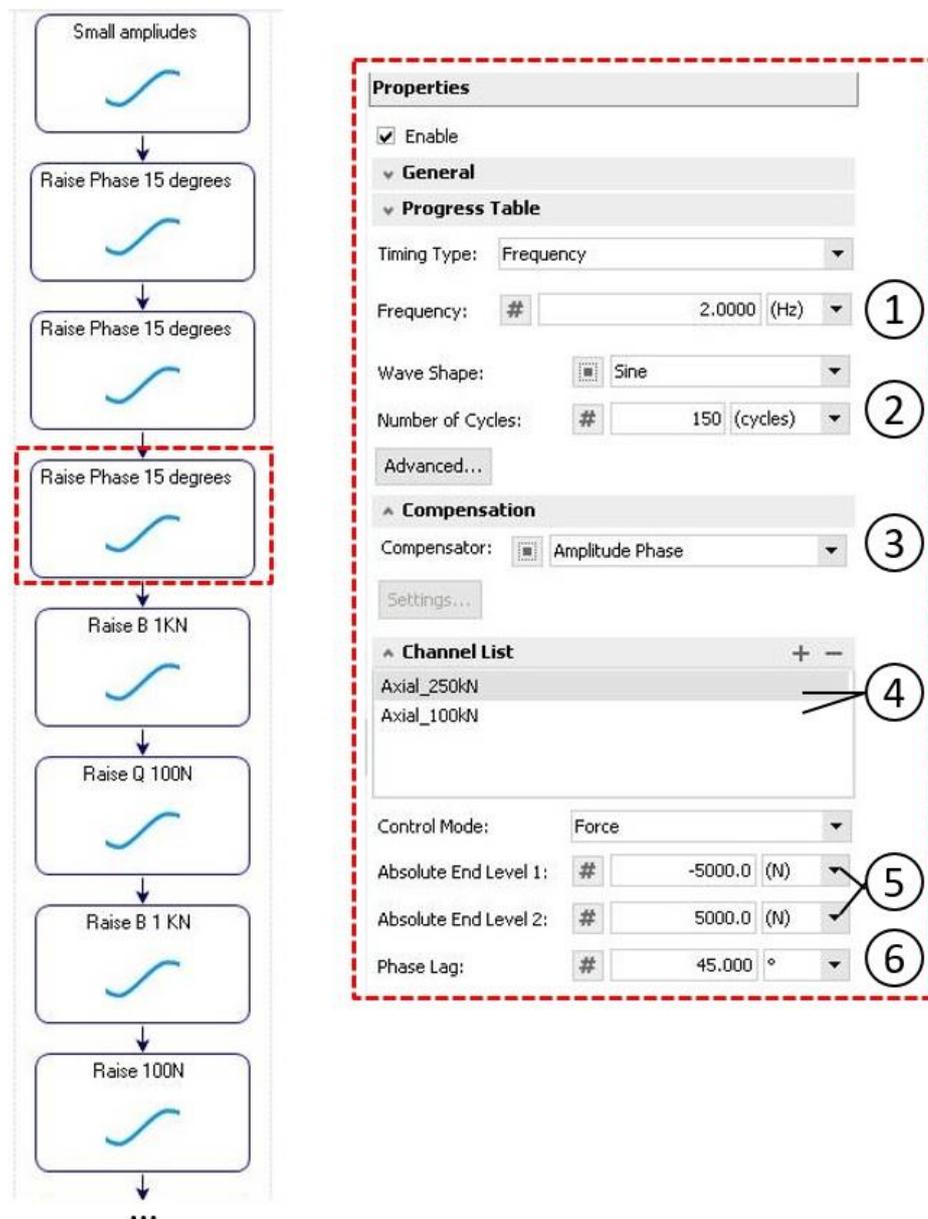
Figure 4.14 Overview of the MTS TestSuite © blocks diagram procedure to conduct an out-of-phase fretting fatigue test on left, and configuration of a single block on right: 1) frequency adjustment, 2) Number of cycles of the block, 3) Compensator to use, 4) Selection of the fatigue (250KN) or the fretting (100KN) load, 5) Maximal and minimal values of the selected load, and 6) desired phase angle.

In the first block, tiny increments of fretting load and bulk loads are applied. Afterwards, the wanted phase angle is progressively established using a step of 15° between every block. The corresponding frequency, when differs from 2 Hz, is then settle using steps of 1Hz. Finally, loads are progressively raised, one after the other, until reaching the desired values of B and Q. Steps of 50N and 100N are used to raise the fretting force for the Al7050, while steps of 500N and 1000N are used for the CA6NM. Every diagram block of the procedure lasts 150 cycles which permits to stabilize the response and give time to the user to confirm good correlation between command and response. An additional MTS scope must be created to visualize the response of the 250kN activator and of the 100kN activator in the same graph, to make sure that the right phase angle is applied. It is necessary to check that the force command signals and the force response signals present a good correlation during all the procedure. A maximum difference of 50N between command and response has been considerate acceptable for the Al7050 while 200N was adequate for the CA6NM. The last block diagram of the procedure permits to record the data of the test in a data file for a given number of cycles (10^7 cycles for the Al7050 and 10^6 cycles for CA6NM). The test ends either with the total fracture of the specimen or when the fatigue limit defined in the last diagram block is reached. An overview of the procedure is given in Figure 4.15.
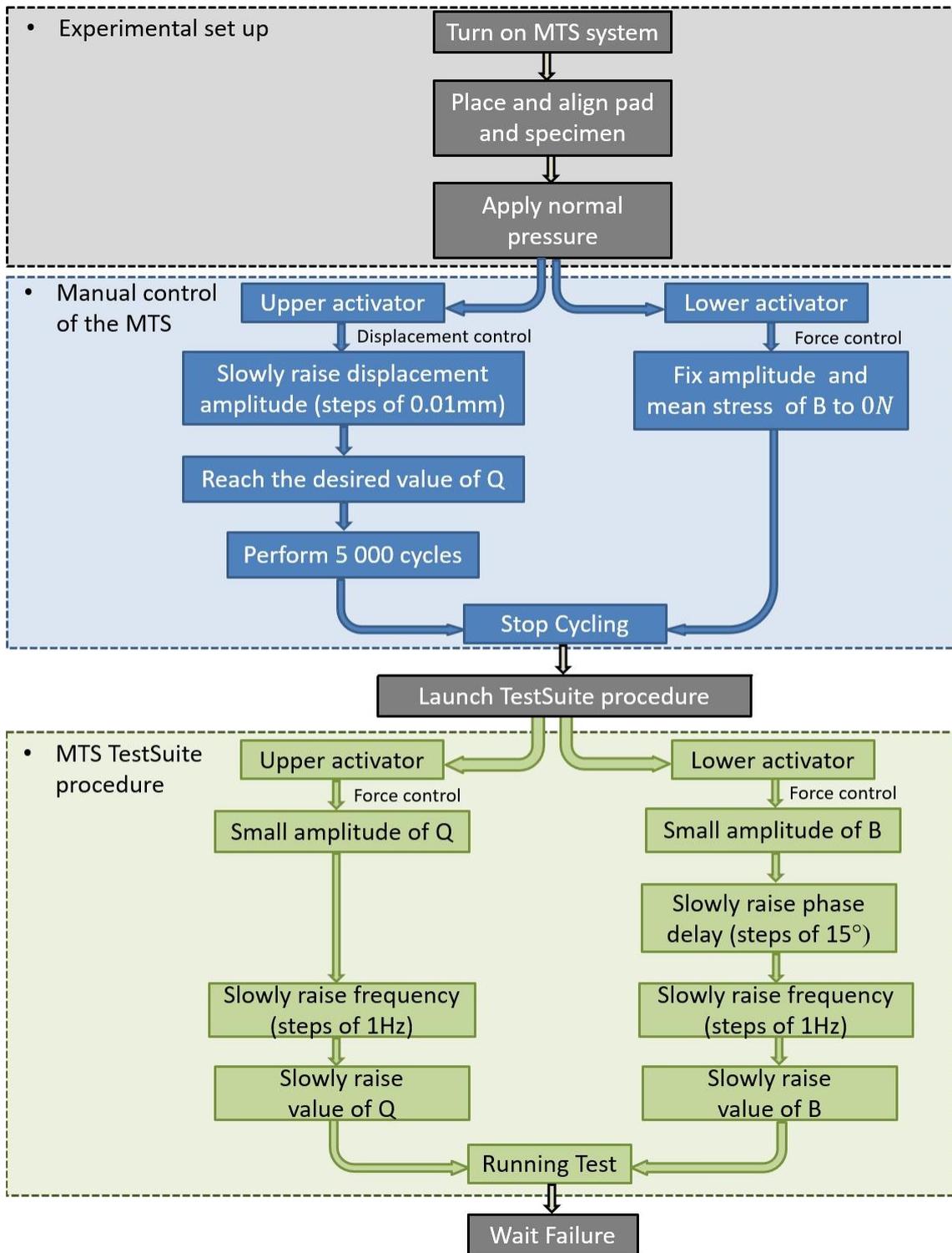
Figure 4.15 Overview of the method to conduct out-of-phase fretting fatigue tests, with the three main steps: Experimental set-up, Pre-test process, and application of the phase angle.

4.3 Numerical method

Most of the engineering problems encountered nowadays can be expressed through ordinary differential equations (ODEs) or partial differential equations (PDEs). However, few problems have an analytical solution. In this sense, numerical methods can be used to give an approximate description of the solution. In this work, the commercial finite element software Abaqus© CAE has been used to model and simulate the contact problem at hand. The in-phase condition has been used to evaluate the accuracy of the model. Concerning the out-of-phase loadings, simulations were carried-out to analyze the phase angle effect on the stress distributions and its eventual influence of on the fatigue life.

4.3.1 Numerical modeling

In order to get a simple and relevant input geometry for the finite element, it has been chosen to model the problem in two dimensions (Fig. 4.16). The pad is modeled as a (13×6.5) mm part with a radius of 70 mm, while the specimen is represented by a (6.5×20) mm rectangular part.
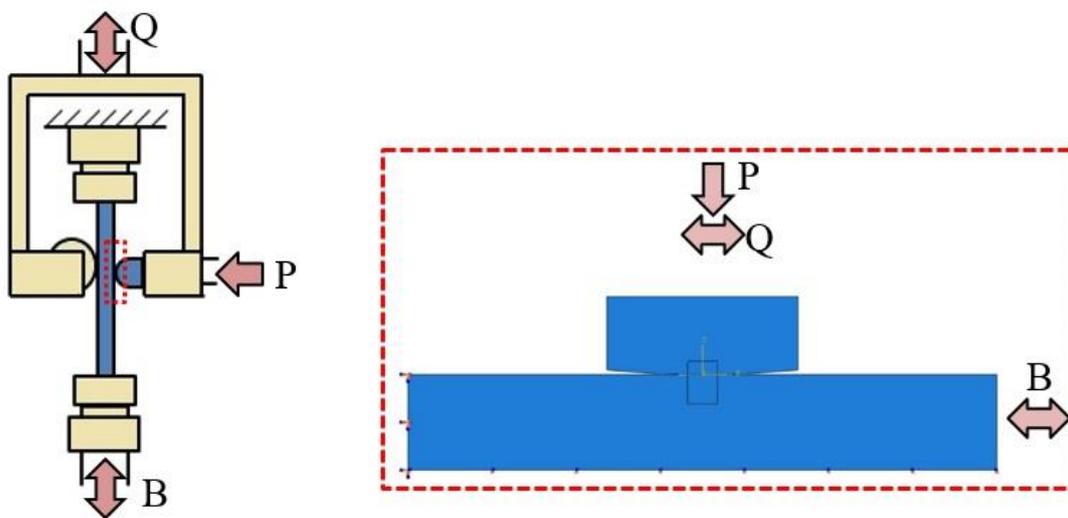
Figure 4.16 Overview of the global fretting fatigue problem on left, and Abaqus© 2D modelling on right.

4.3.2 Finite element modelling

The material properties are given to both parts in accordance with the data presented in Tab. 3.1 and Tab. 3.3, for the Al7050 and CA6NM, respectively. The friction coefficient of the Al7050 was obtained by Rossino et al. [85], the value was verified to be equal to 0.54, while for the CA6NM it has been set to 0.70 [94].

The interaction between bodies has been defined as a surface to surface contact, taking the pad as master surface and the specimen as slave surface. This contact discretization has a higher computational cost than the node to surface formulation, but gives more accurate results [95]. Because of the non-linearity associated with surface contact force conditions, an iterative strategy is generally required to obtain a precise solution. The Lagrange multiplier method has been used in this work, as it gives the exact solution for the normal tractions while avoiding the well-known issues with the tangential loads [96]. This method gives the following expression for the finite element equation of motion:

$$M\ddot{u} + F(u,\dot{u}) + G\lambda = R \tag{4.1}$$

where $\mathbf{M}$ is the mass matrix, $\boldsymbol{u}$ is the displacement vector, $\dot{\boldsymbol{u}}$ represents the velocity, $\ddot{\boldsymbol{u}}$ is the acceleration, $\mathbf{F}$ is used for internal forces and $\mathbf{R}$ for external forces. The so-called Lagrange multiplier is the vector $\boldsymbol{\lambda}$, whose components are the surface contact forces, and $\mathbf{G}$ is a surface contact displacement constraint matrix that prevents the master surface from penetrating the slave surface (Fig. 4.17), governed by the following equation:

$$G\{u + X\} = 0 \tag{4.2}$$

where $\mathbf{X}$ is the material coordinate vector. The Lagrange multiplier method employs $\boldsymbol{G}$ as additional unknowns and the Eq. (4.1) and Eq. (4.2) must be solved simultaneously.
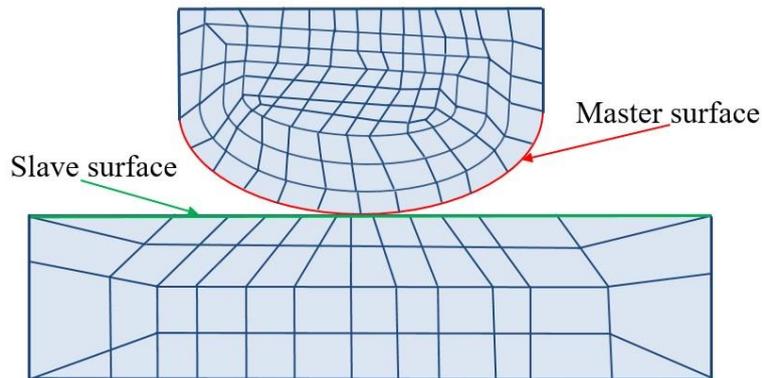
Figure 4.17 Definition of the surface to surface contact.

In order to adequately model the problem, it is necessary to apply the three loads occurring during fretting fatigue test and an adequate representation of the boundary conditions, as depicted in Figure 4.18. A first reference point has been created at the top of the pad, to apply the normal load, P, and the fretting load, Q. The top edge of the pad

has been assigned to this reference point. The bulk load is applied to the specimen, using another reference point (right side). The left edge of the specimen is fully constrained while the bottom edge is restrained in the vertical direction.
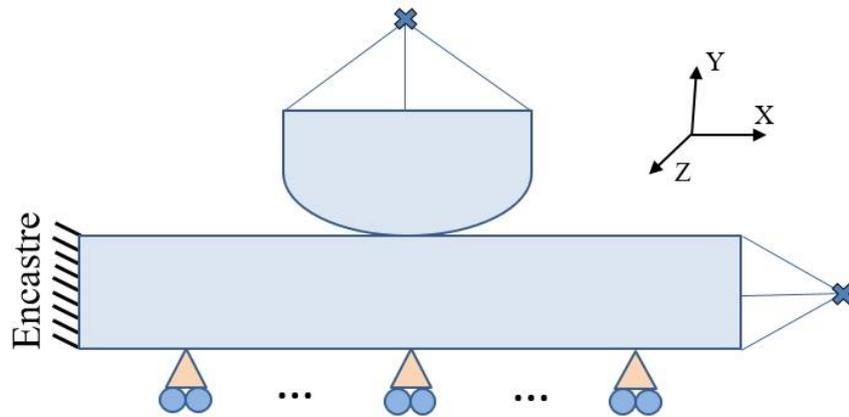
Figure 4.18 Boundary conditions of the problem.

The applied loads, already discussed in the Section 4.2, are defined in Table 4.6. The normal pressure is firstly applied to the pad, and remains constant all the test. Then follows the application of the sinusoidal fatigue and fretting loads. For in-phase loading, they are apply in a same step that has a circular frequency of 2π. When conducting a simulation with a phase angle of $\Phi=45°$, the tangential load is firstly applied in a step that have a circular frequency of $\pi/4$. Afterwards, the fatigue load starts while the fretting load already reached the amplitude corresponding to this frequency. For simulations with a phase angle of $\Phi=90°$, the fatigue load initiates after the tangential load reached a circular frequency of $\pi/2$, and for simulation with $\Phi=135°$, after $3\pi/2$.

Table 4.6 – Values of the loads applied in the 2D model.

	P [N.mm^{-1}]	Q [N.mm^{-1}]	B [N.mm^{-1}]
Al7050	446	172	1475
CA6NM	1 230	423	3845

4.3.3 Validation of the model

The solids are discretized with second order finite elements, which provides better continuity of the stress field and higher accuracy. The model has been partitioned, dividing the contact zone from the rest of the model, as seen in Figure 4.19. The contact zone, where stresses are determinant for crack nucleation, has structured mesh. In the rest of the model, elements are left free so that they can have triangular or rectangular shape,

and their sizes vary from 1mm, at the extremities of the model, to 0.01 mm in the contact zone vicinity. Note that with the loads described in Tab. 4.6 and according to Eq. (2.9), the contact semi width a is equal to 1mm for both Al7050 and CA6NM. Therefore, the contact partition was set as a square of 2mm, to allow a precise evaluation of the stress behavior over depth. Moreover, the size of the finite elements that belongs to the contact area will be further discussed in Chapter 5, as they are determinant for the model's accuracy.
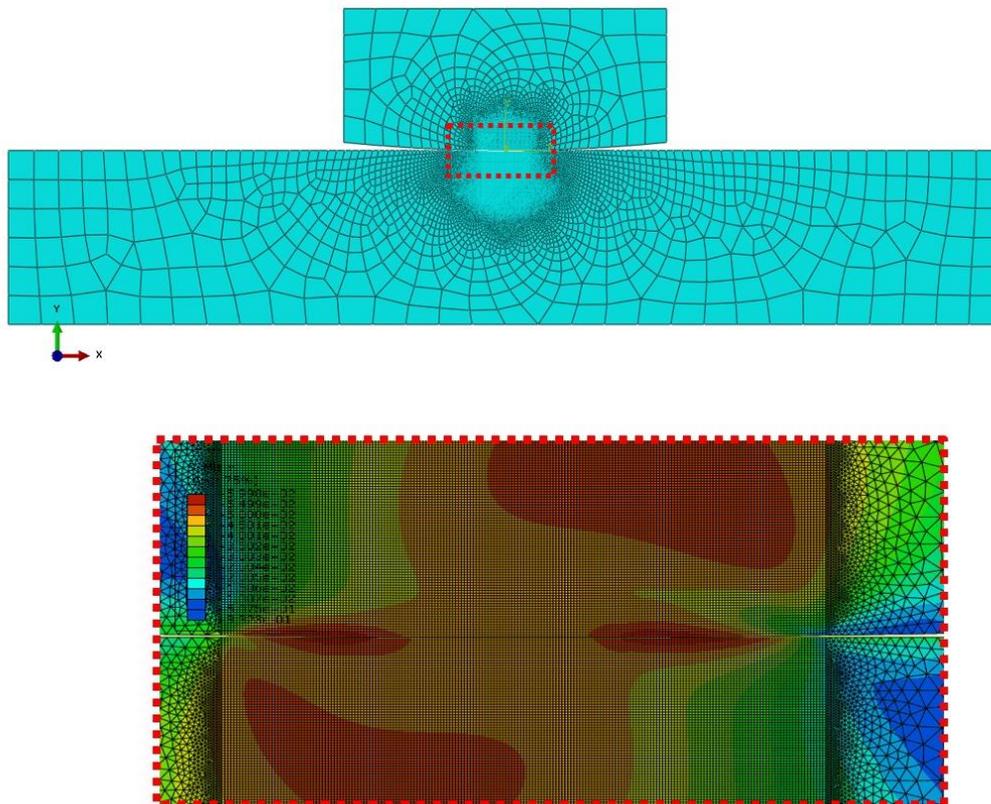
Figure 4.19 Representation of the mesh of the model and zoom of the structured elements of the contact (size of 0.01mm here).

The stresses values, σ_{xx}, σ_{yy}, σ_{zz} and τ_{xy}, are extracted from the structured elements of the contact zone for analysis. The stresses analysis starts when the bulk load is applied, and lasts a circular frequency of 2π so that both fretting and fatigue loads experience a complete loading cycle (see Figure 4.20), regardless the phase angle of the simulation. These loading histories are divided in 64 time steps. Once the values are picked up from elements, the determinant stresses for crack nucleation, τ_a and $\sigma_{n,max}$ are calculated according to Chapter 3. The numerical analysis of contacting elements, or of edges elements along depth is presented in Chapter 5.
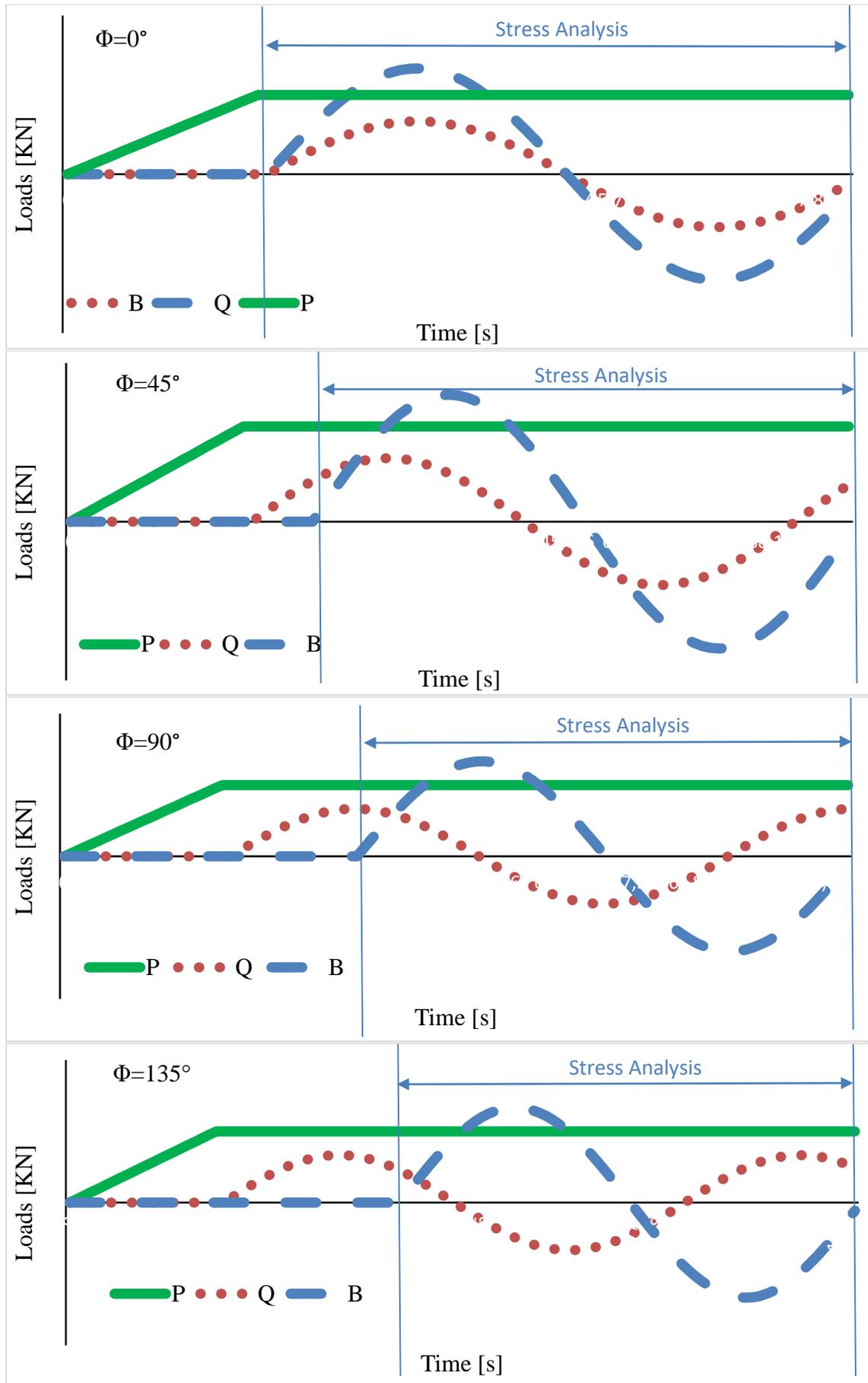
Figure 4.20. Visualization of the stress history analysis for each phase angle simulation.

4.4 Failure analysis

In order to gain additional information about the phase angle effect, microstructural observations, employing several techniques, have been conducted.

4.4.1 Equipment

In this work, a confocal laser microscope (Olympus LEXT, Figure 4.21) and a Scannig Electron Microscope – SEM (Jeol JSM.7100F, Figure 4.22) have been used.

Figure 4.21 Confocal laser microscope.

Figure 4.22 SEM.

The confocal microscope is able to capture the surface profile of a sample which allows the measurement of roughness, fracture area and fracture angles. During this study,

most images have been taken using the stitching function of the equipment, that successively capture samples and build an assembly to get a single high resolution image.

The fracture morphology of the specimen was analyzed with the SEM. This equipment produces images by scanning surface of samples with a focused beam of electrons. The electrons interact with sample atoms, producing signals that contain information about the sample's surface topography and composition. The failure surface has been investigated, attempting to locate the cracks nucleation, and to find information of the microstructural mechanisms involved in the fatigue process.

4.4.2 Inspections
The fracture samples have been cut from the "dog-bone" specimen (see Fig. 4.23).
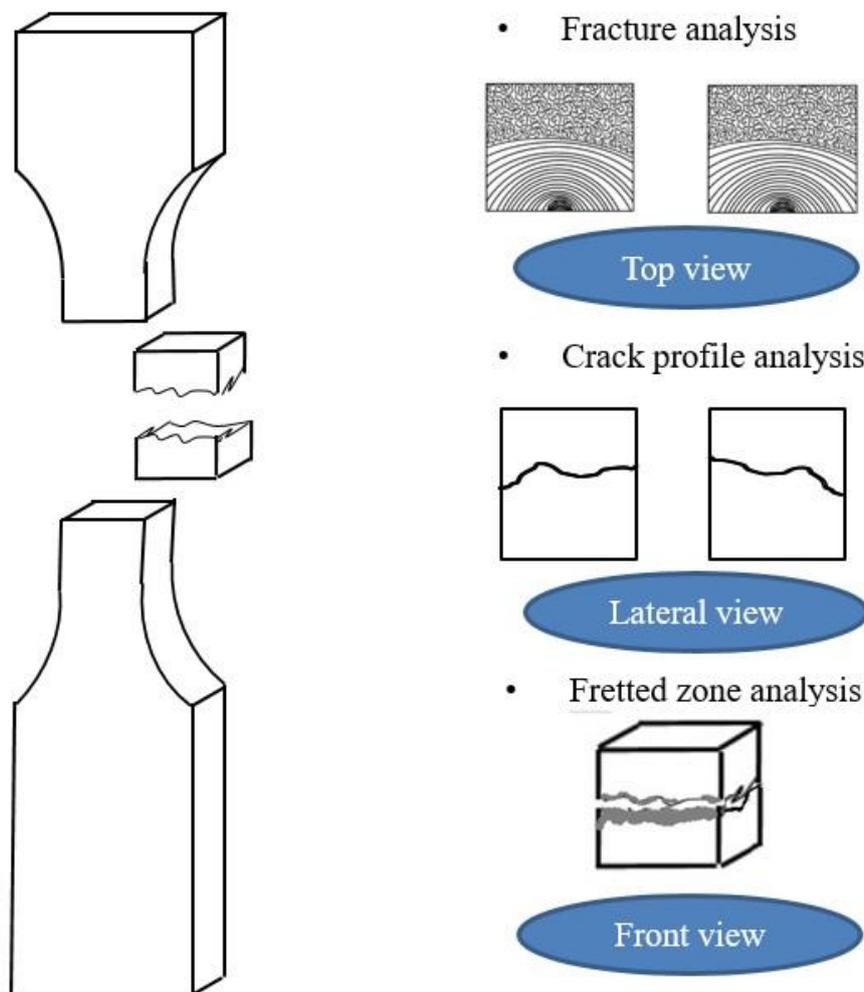
Figure 4.23 Visualization of the different sample faces observed for the failure analysis.

To get information about the failure process, different parts of the fractured specimen have been observed. The top fracture surface has been inspected with the

Confocal microscope and the SEM to verify the crack initiation zone. The lateral facets of the samples also have been inspected, to evaluate if the crack profile is different from a phase angle to another. Finally, the fretted zone (area that endure the contact of the pad), has been analyzed to find the in which position (trailing edge or leading edge) the failure occurred.

Chapter 5. Phase angle effect on the Al7050

This chapter presents the effects of a phase angle introduced between the fretting load and the bulk load. Experiments, numerical and failure analyses of the Al7050, are given. Three phase angles are investigated (Φ=45°, Φ=90° and Φ=135°), and compared with the in-phase loading condition.

5.1 Al7050 experimental results

Herein, the experimental life, N, is defined as the number of cycles after the pre-test until the failure of the specimens. Note that each specimen has been subjected to 5000 cycles in displacement control mode corresponding to the establishment of the friction coefficient and to 15000 cycles corresponding to the establishment of loads values (see section 3.2.2). These 20000 cycles are not taken into account in the presented values of N.

A total of eight tests for the assessment of the experimental life of the Al7050 specimens were conducted, one test series for each angle (0°, 45°, 90° and 135°) and a second series for repetition and dispersion analysis. The results are presented in in Fig. 5.1 and Tab. 5.1.
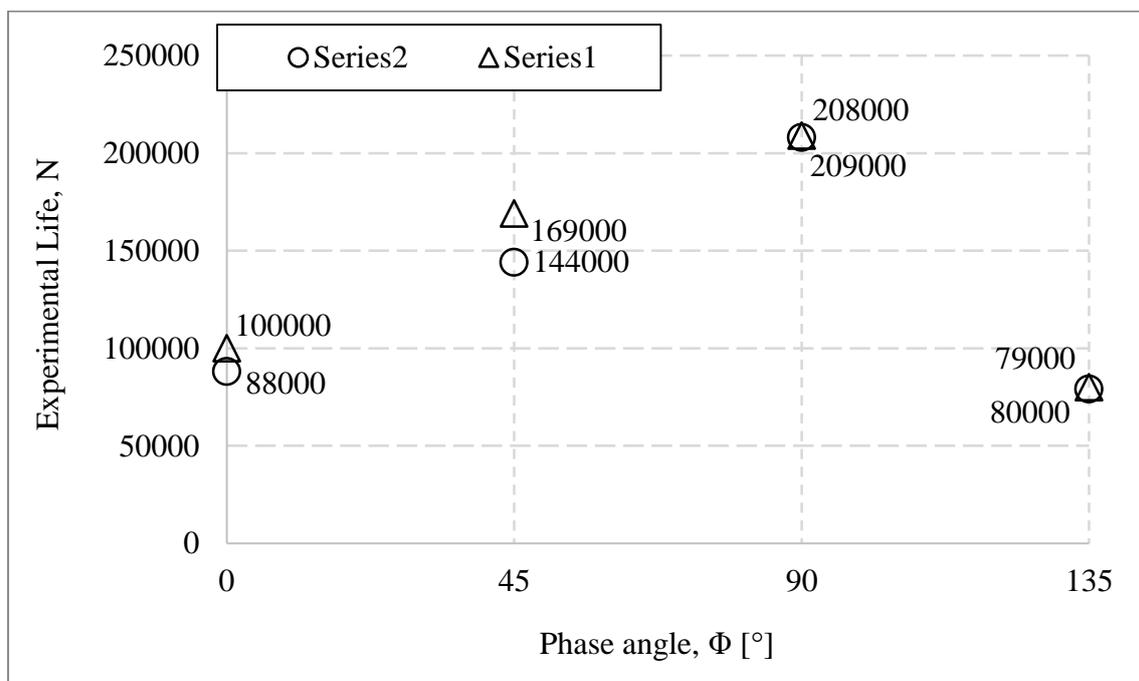
Figure 5.1. Experimental lives *versus* phase angle for the Al7050.

Table 5.1 – Experimental lives data for the Al7050.

Series	$\Phi=0°$	$\Phi=45°$	$\Phi=90°$	$\Phi=135°$
1	100000	144000	209000	79000
2	88000	169000	208000	80000
Average	94000	156500	208500	79500
Standard deviation	6000	12500	500	500

Figure 5.1 reveals that lives vary in function of the phase angle while Tab. 5.1 shows low values for the standard deviation (below 7%), which is considered a low dispersion in fatigue analysis. The in-phase condition provided an average life of 94k cycles, the introduction of a phase angle of 45° lead to a life of 156500 cycles (an increase of 67%). Following this trend, a phase angle of 90° lead to a life of 208500 cycles which is 122% higher than the reference condition. Nevertheless, when the phase angle is set to 135° life is reduced in 15%. From this data, one can imply that an increase of the phase angle, in the 0-90° range, should lead to a direct increase on the life of the specimen. Furthermore, being able to introduce a phase angle of 90° could lead to a significant life increase of a mechanical component used in an industrial application enduring a fretting fatigue condition.

5.2 Al7050 numerical results

In this section the validation procedure employed for the numerical model and stress analyses are presented. Furthermore, the results for the life estimation using different criteria are discussed.

5.2.1 Validation of the model

The mesh of the contact zone has been refined until an adequate representation of the analytical solution was achieved. Figure 5.2 shows the accuracy of the model, for different element sizes (80μm, 40μm, 20μm and 10μm), when predicting both normal pressure and shear traction distributions. The errors observed for each configuration are detailed in Tab's. 5.2, 5.3, and 5.4.
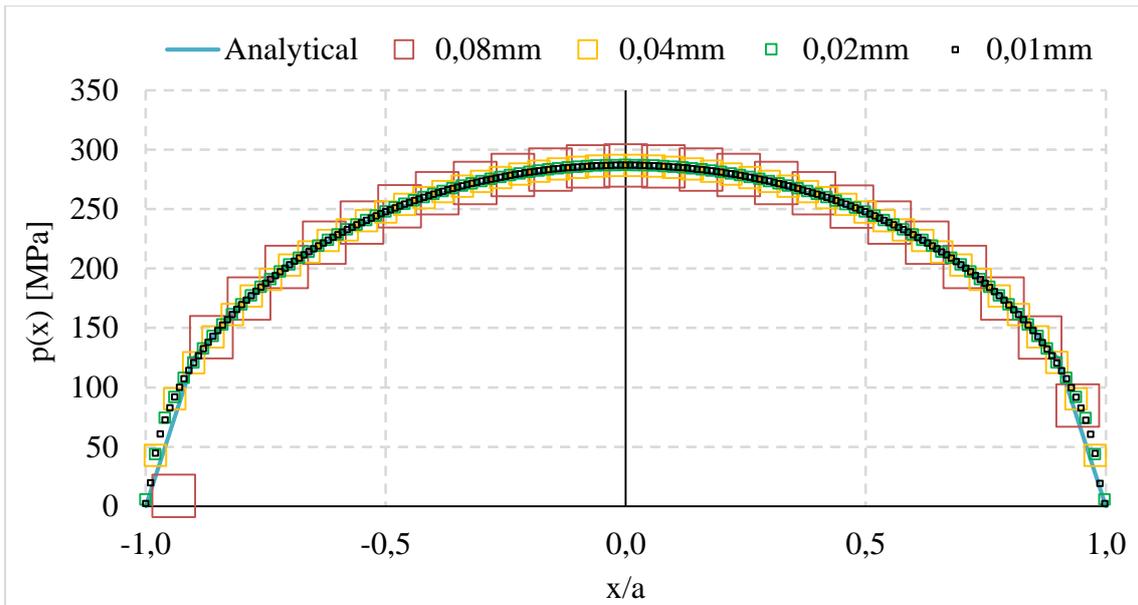
a)   Normal pressure distribution p(x).
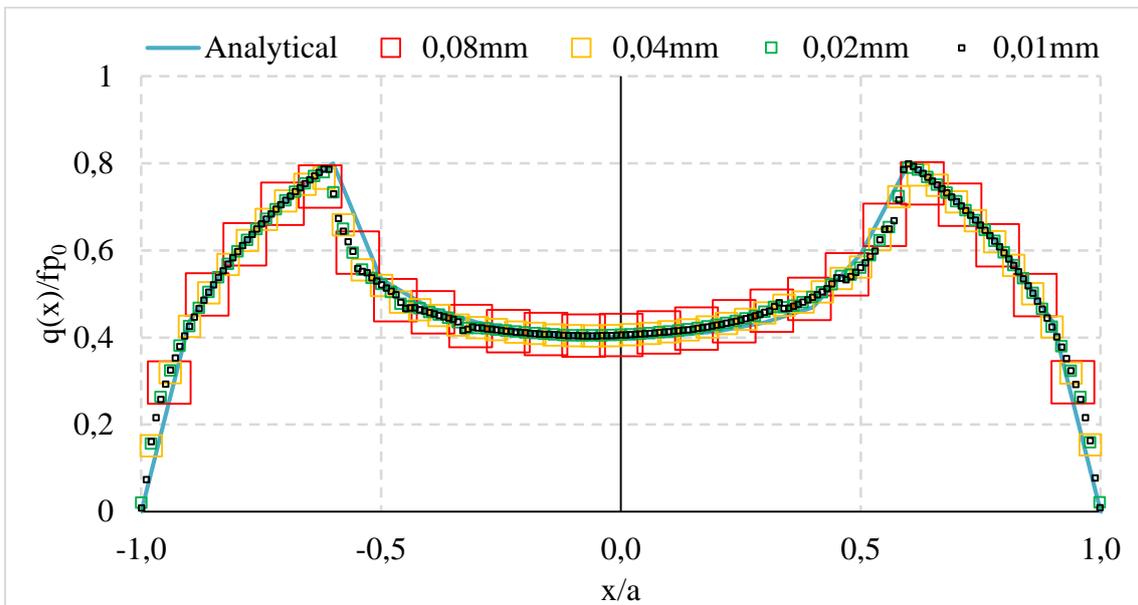
b) Shear traction distribution q(x).

Figure 5.2. Comparison between the analytical solution and the numerical model.
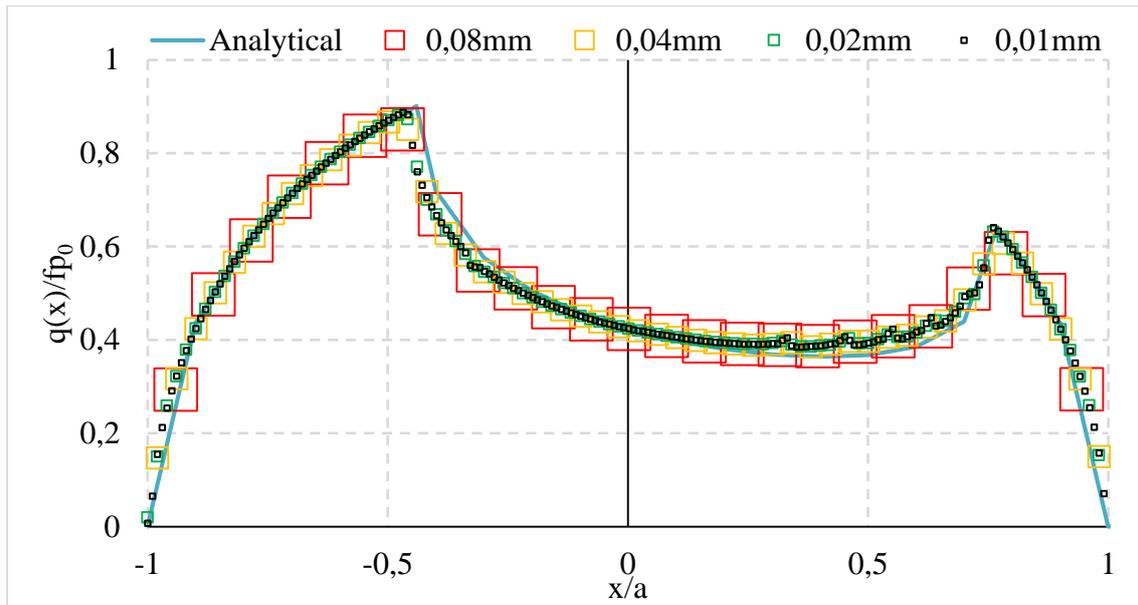
c) Shear traction distribution q(x), in presence of the bulk load.

Figure 5.2. Comparison between the analytical solution and the numerical model.

Table 5.2 – Accuracy and performance of the normal pressure simulations according to element size.

FE size [mm]	a ana [mm]	a num. [mm]	Error of a [%]	p_0 ana. [MPa]	p_0 num [MPa]	Error of p_0 [%]	Time [s]
0.08	1	1.02	2.04	284.9	287.1	0.61	49
0.04	1	1.04	3.89	284.9	286.98	0.65	75
0.02	1	0.99	0.11	284.9	286.76	0.73	149
0.01	1	0.99	0.11	284.9	286.76	0.73	564

Table 5.3 – Accuracy and performance of the shear traction simulations according to element size.

FE size [mm]	c ana [mm]	c num. [mm]	Error on c [%]	q_{max}/fp_0 ana. [MPa]	q_{max}/fp_0 num. [MPa]	Error on q_{max}/fp_0 [%]	Time [s]
0.08	0.6	0.55	8.44	0.8	0.75	6.23	49
0.04	0.6	0.58	3.45	0.8	0.77	3.72	87
0.02	0.6	0.59	1.78	0.8	0.78	1.03	224
0.01	0.6	0.59	0.12	0.8	0.79	0.77	839

Table 5.4 – Accuracy and performance of the shear traction in presence of the bulk load simulations according to elements size.

FE size [mm]	e ana [mm]	e num [mm]	Error of e [%]	q_{max}/fp_0 ana. [MPa]	q_{max}/fp_0 num. [MPa]	Error of q_{max}/fp_0 [%]	Time [s]
0.08	0.17	0.16	8.44	0.9	0.86	4.55	50
0.04	0.17	0.12	3.45	0.9	0.87	3.33	91
0.02	0.17	0.14	1.78	0.9	0.88	2.33	252
0.01	0.17	0.16	0.12	0.9	0.89	1.12	926

Results indicate that the use of 20μm elements should be appropriate for this study. Indeed, this element size gives an accuracy of about 99% when the normal pressure and the tangential load are applied, and about 98% in presence of the bulk load. Furthermore, this configuration of the mesh is attractive from the computational time point of view, as going from 20μm elements to 10μm elements increases the cost in about four times without significant errors reduction. However, for the fatigue life estimation using the stresses of an element located at a certain distance from the surface (see Section 2.3), it is necessary to employ 10μm elements as a deviation in life prediction of about 10000 cycles is observed between elements when employing 20μm size. Therefore, structured quadrilateral second order elements with 20μm in size have been used in the contact zone for preliminaries investigations while 10μm elements have been used for the life estimations.

5.2.2 Shear traction distribution

Unfortunately, an analytical solution for the shear traction distribution in an out-of-phase condition is not available. Nevertheless, a brief analysis of distributions behavior for different phase angles is presented here. Figure 5.3 shows the results obtained with the numerical model at different phase angles, at different loading times. Note that, together with the Muskhelishvili's potential, the shear traction distribution permitted the analytical calculation of stresses for the in-phase loading at maximum and minimum loading time, but also during loading and unloading (see Chapter 2). The shear traction distribution, at others determinant loading times, for the different phase angles is given in Fig. 5.3.
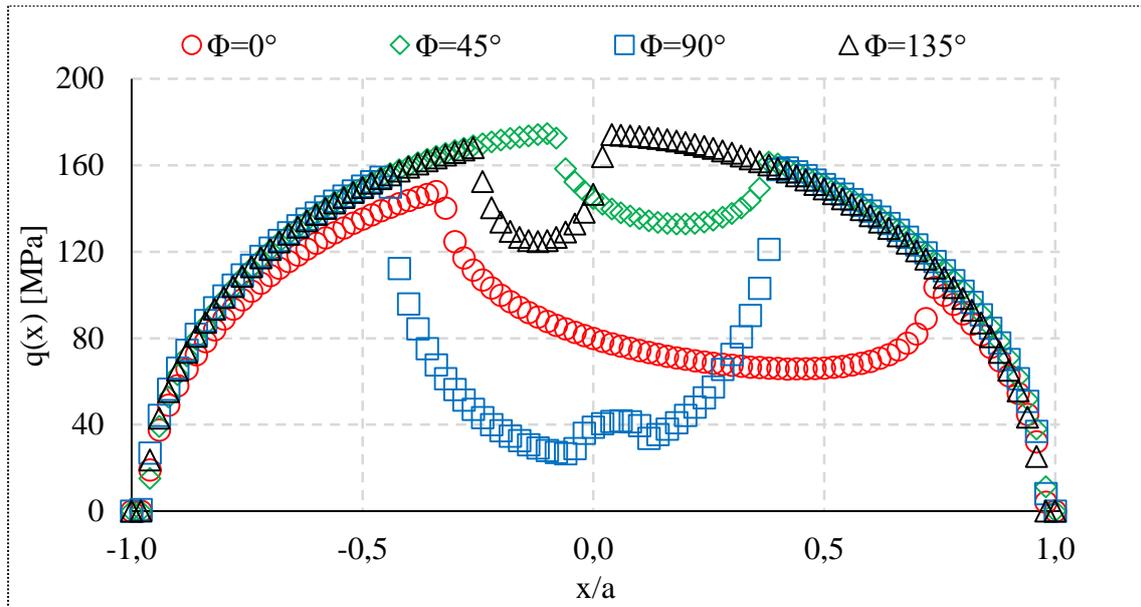
a) At the loading time $\pi/2$
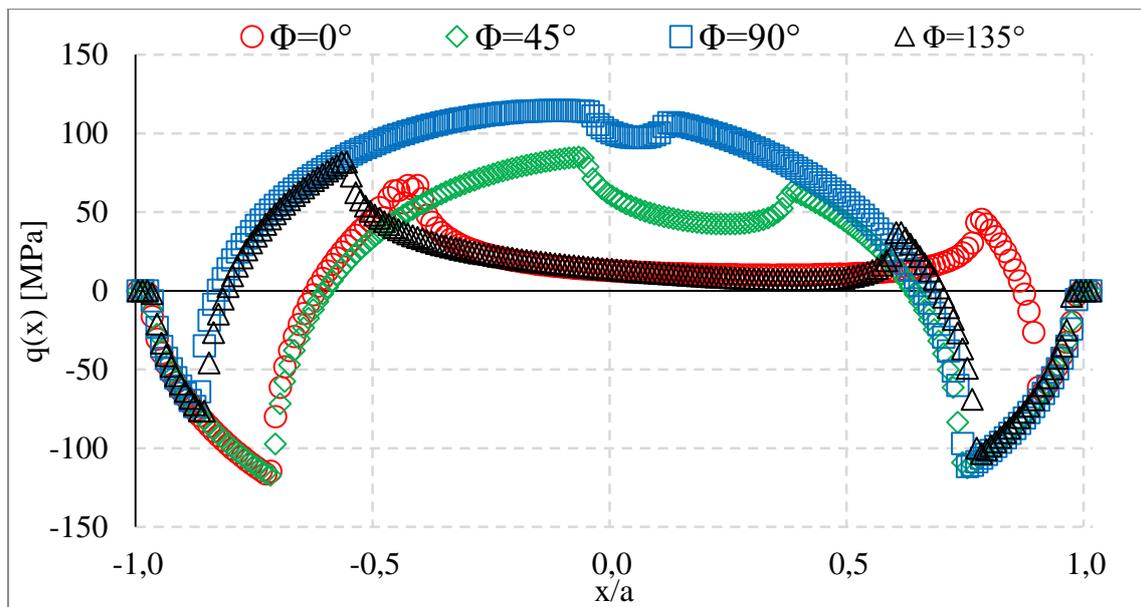
b) At the loading time π

Figure 5.3. Comparison of the shear traction distributions for different phase angle.
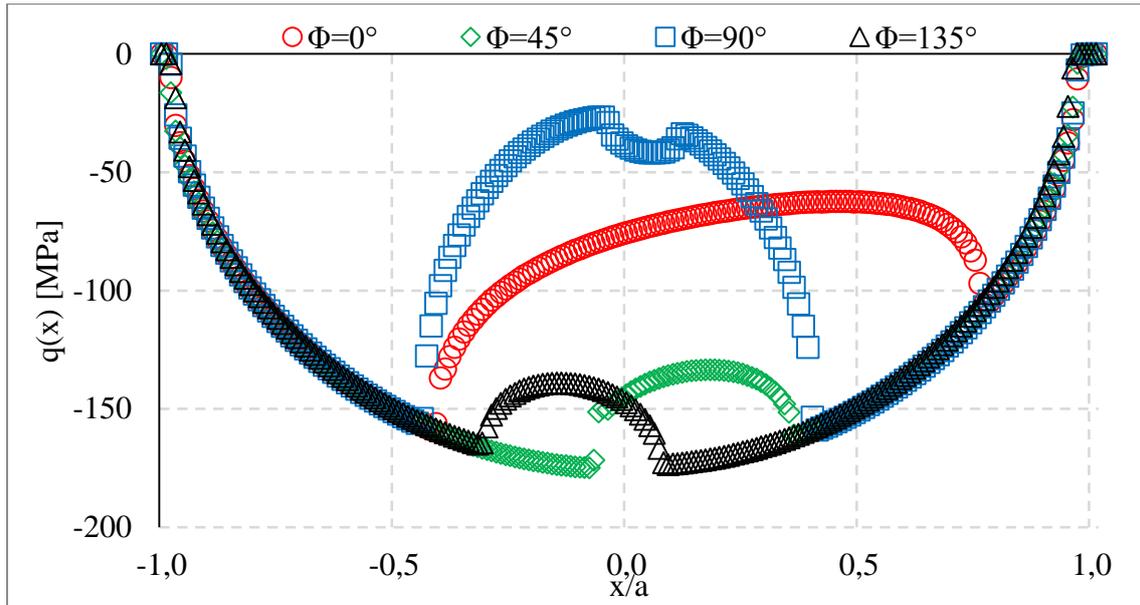
c) At the loading time $3\pi/2$
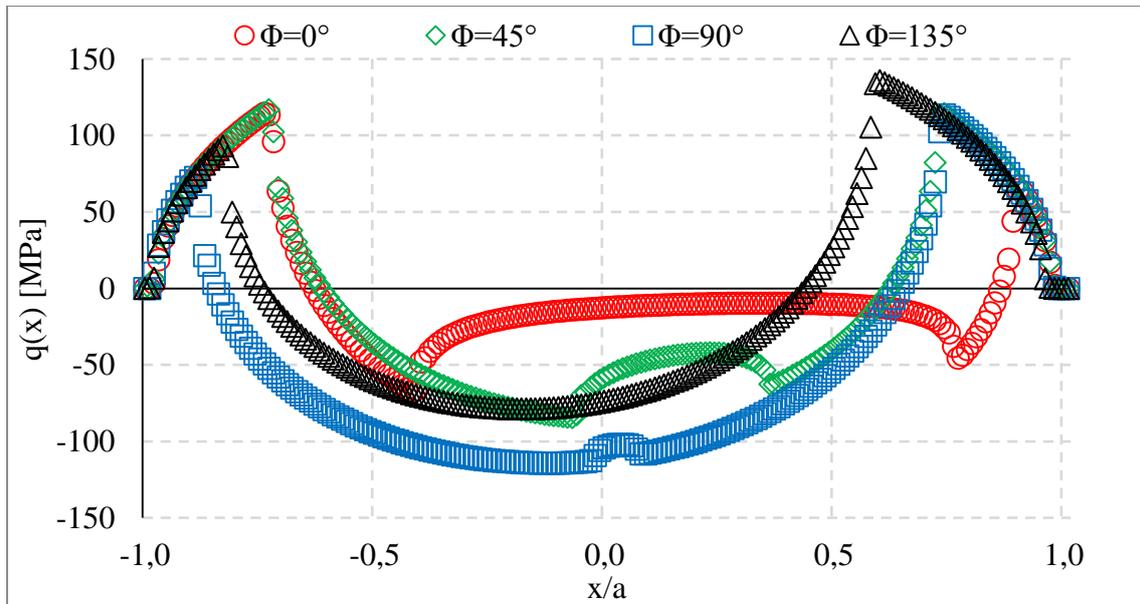
d) At the loading time 2π

Figure 5.3. Comparison of the shear traction distributions for different phase angle.

Looking to the loading time $\pi/2$, it seems that $\Phi=90°$ shortly reduces the offset e, while $\Phi=45°$ and $\Phi=135°$ lead to higher offset values. At this loading time, looking to the total size of the stick zone, $2c$, it appears that the stick regime is higher for $\Phi=0°$, and vary depending on the applied phase angle. When the fretting load reach the circular frequency, the size of the stick zone is equal to 1mm, 0.5mm, 0.8mm and 0.4mm for the phase angles of 0°, 45°, 90° and 135°, respectively. Another important remark is that, at this same instant, looking at the center of the contact zone, the maximal value of the shear

traction is found on the left side for Φ=0° and Φ=45°, and on the right side for Φ=135°. For Φ=90°, the distribution is almost symmetrical, which makes sense as at π/2 the bulk load is equal to zero and has no influence on the shear traction distribution. In fact, the curve obtained when the delay of bulk load is 90° curve clearly reminds the shear traction distribution when only the normal and the fatigue loads are applied (see Fig 2.10), except a small perturbation at the center of the contact that may result from the loading history. Quantitatively, the highest values of the maximal shear traction are obtained with Φ=45° and Φ=135° while the smallest value is associated to the in-phase loading. The phase angle of 90° gives an intermediate value for the maximal shear traction, remaining close to the one obtained for Φ=0°.

5.2.3 Load path

The components σ_{xx}, σ_{yy}, σ_{zz}, and τ_{xy} of the stress tensor have been retrieved from the elements located at the extremities of the contact zone, where cracks are supposed to nucleate. The load paths have been plotted in a σ_{xx} vs τ_{xy} graph, using the same scale, in order to assess the eventual non-proportionality induced by the phase angles (see Fig. 5.4).

a) at the trailing edge.
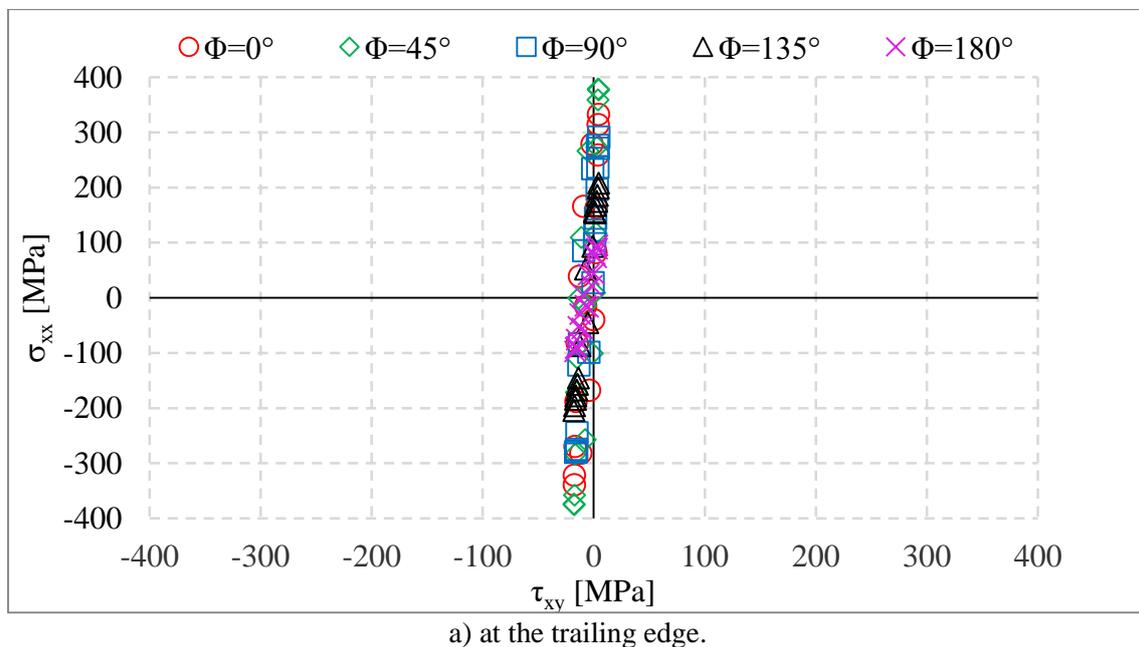
Figure 5.4. Visualization of the load paths for different phase angles.
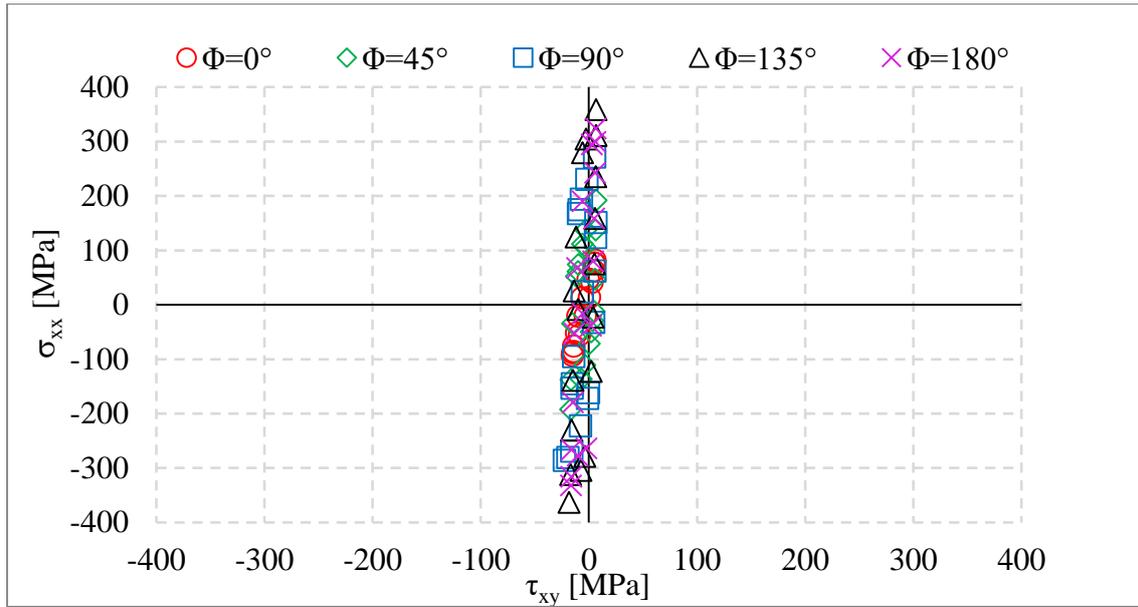
b) at the leading edge.

Figure 5.4. Visualization of the load paths for different phase angles.

For the sake of simplicity, the stress histories (overall commonly divided in 64 time-steps) has been reduce to 16 points in this particular study. The load paths plotted at the position $x/a = -1$ (Fig. 5.4a) and $x/a = 1$ (Fig. 5.4b) are known as the trailing edge and the leading edge, respectively. Phase angles (Φ=45°, Φ=90°, Φ=135°) are compared with the in-phase loading (Φ=0°) and the opposition o phase loading (Φ=180°). Obtained curves show a pattern similar to proportional loading condition, far from the elliptical or circular shapes usually observed for multiaxial loading [97]. A close look reveals that σ_{xx} values (Tab are significantly different for each phase angle.

Table 5.5 – Values of σ_{xx}, at both contacting edge, according to the applied phase angle.

	Φ=0°	Φ=45°	Φ=90°	Φ=135°	Φ=180°
Trailing edge (x/a=-1)	333 to -337 MPa	359 to -357 MPa	291 to -282 MPa	214 to -206 MPa	94 to -96 MPa
Leading edge	81 to -91 MPa	192 to -192 MPa	276 to -282 MPa	340 to -362 MPa	324 to -331 MPa

It can be assumed that for the loading configuration Φ=0° and Φ=45°, stresses are mainly concentrated at the trailing edge while for the Φ=135° and Φ=180° highest stresses are located at the leading edge. Concerning the Φ=90°, the σ_{xx} values are well balanced going from about 291 MPa to -282 MPa at both extremities of the contact zone. Another important observation is that the stress occurring at the trailing edge for Φ=45° (378 MPa

73

to -357MPa) are very close in values to those occurring at the leading edge for Φ=135° (340 MPa to-362 MPa). Reciprocally, the low stress values found at the position $x/a = -1$ for Φ=135° are similar to those obtained at $x/a = -1$ for Φ=45°. This phenomenon also occurs when comparing the in phase loading Φ=0° and the opposition of phase loading Φ=180°. Finally, it can be assumed that for the loading configurations Φ=45° and Φ=135° the values of σ_{xx} are reversed from the trailing edge to the leading edge, as well for the loading configurations Φ=0° and Φ=180°.

5.2.4 Driving stress parameters for crack nucleation

The driving stresses for crack nucleation have been calculated using the stress tensor components. Afterwards, the critical plane method was applied to every element in the contact zone, going from $x/a = -1$ to $x/a = 1$. The plane that possessed the higher value of the maximal normal stress in between those pre-selected (where the shear stress amplitude is close to its maximal value, $\tau_a = \tau_{amax} \pm 1$ MPa) is considered as the critical one. Note that this assumption corresponds to same one implied by the MWCM. The values of the maximal normal stress $\sigma_{n,max}$, and the shear stress amplitude τ_a, acting in the critical planes are reported Fig. 5.5 for the different loading configurations studied in this work. The analytical solution obtained, using the Muskhelishvili's potentials for stresses calculation, is also presented.
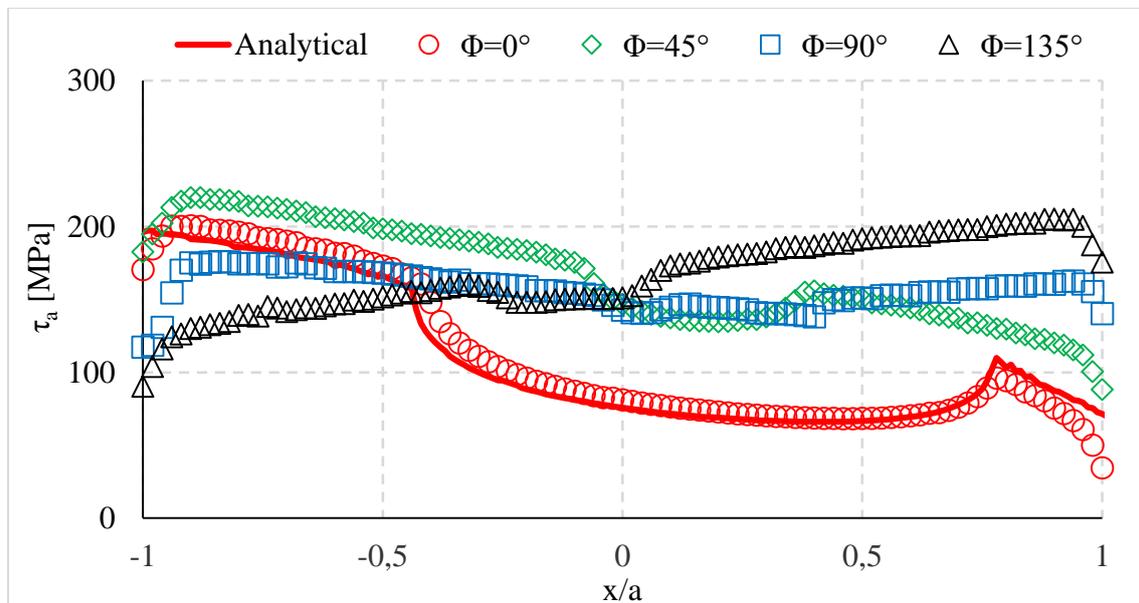
a) Shear stress amplitude over the contact surface, for different phase angles.

Figure 5.5. Evolution of driving stresses.
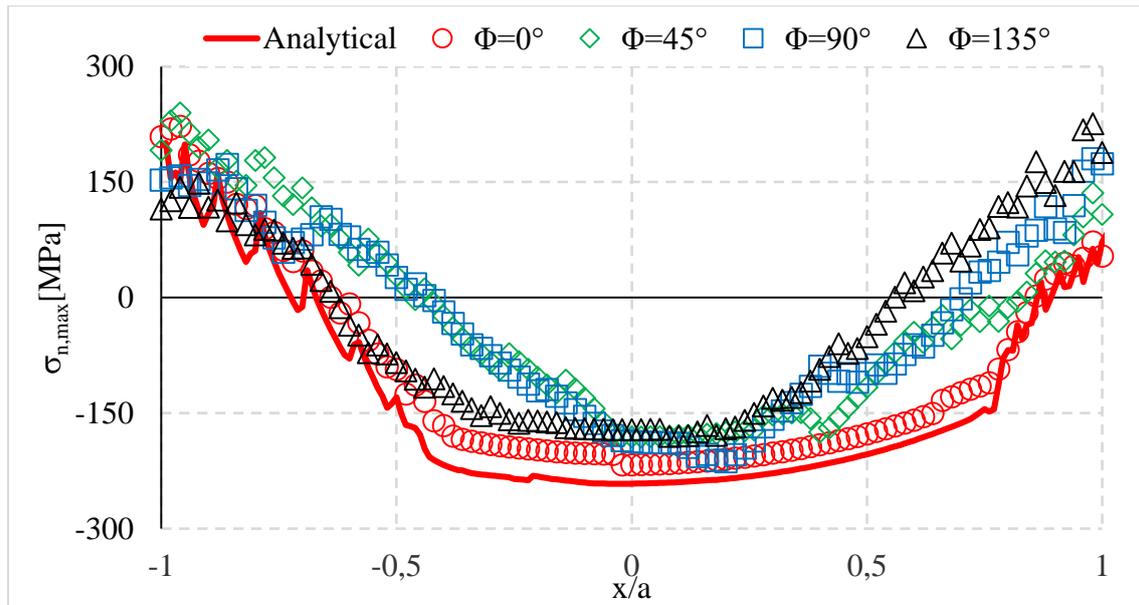
b) Maximal normal stress over the contact surface, for different phase angles.

Figure 5.5. Evolution of driving stresses.

The tendency that the stresses are reversed from Φ=45° to Φ=135° is confirmed. It also appears that looking to the center of the contact ($x/a = 0$) the curves obtained for these two loading configurations are mirrored. The curve obtained for Φ=90° presents stresses symmetrically distributed, with respect to the center of the contact zone. Finally, a good agreement is observed between stresses values of the in-phase simulation and the analytical solution. These observations are more visible looking to the shear stress amplitude curves. Indeed, the maximal normal stress curves are not perfectly continuous over the contact. The small jumps observed, due to the fact that the coordinates of the critical plane change over the contact surface.

Note that if the maximal stresses are rigorously encountered at the extremity of the contact ($x/a = -1$) for the analytical solution, this it is not the case for all simulations (for instance Φ=0° and Φ=45°). The numerical error or the discontinuity of the contact zone must have induced these offsets. However, in conformity with the theory of critical distance formulated with the point method, the driving stresses have been recalculated at a certain distance from the contact surface, using a straight line whose origin takes place in the last contacting elements where the pressure is different from zero. Therefore, this source of instability shouldn't disturb the following analyses.

As explained in Chapter 2, several critical distance equations have been used in this work to estimate the fatigue life. The driving stresses have been calculated over depth,

from the contact surface (0mm) to -1.5mm. This is convenient as the critical distances could depend on the obtained lives, as proposed in Eq. (3.24), but also on the calibration method, as in Eq's. (3.25), (3.26) and (3.27). Results are presented in Figure 5.6 and lives are estimated using the values of the curves at the desired critical distances.
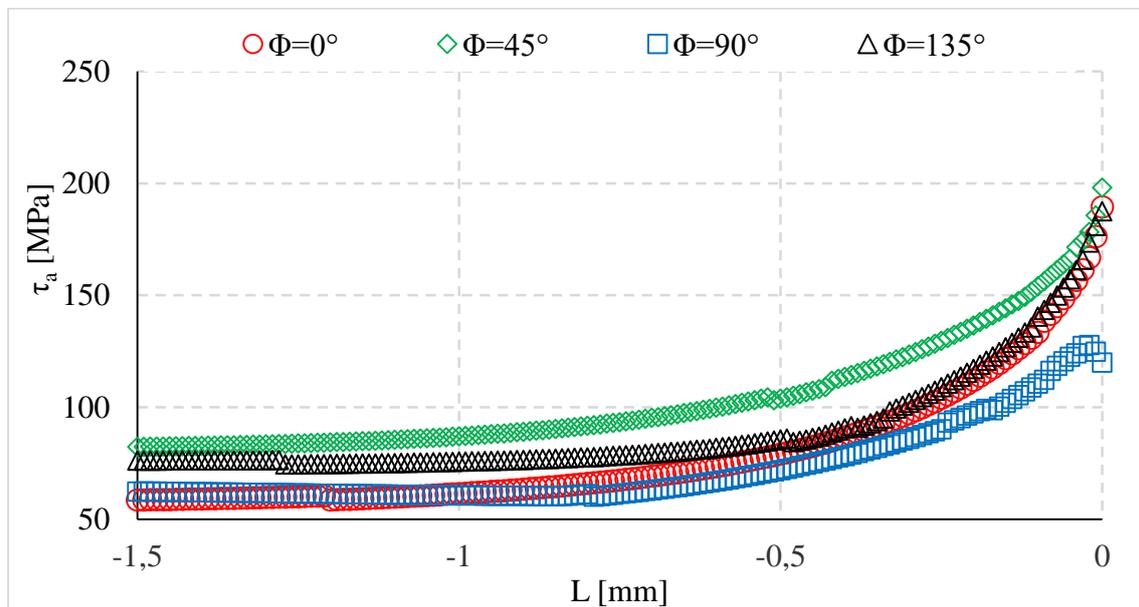
a)   Shear stress amplitude along depth.
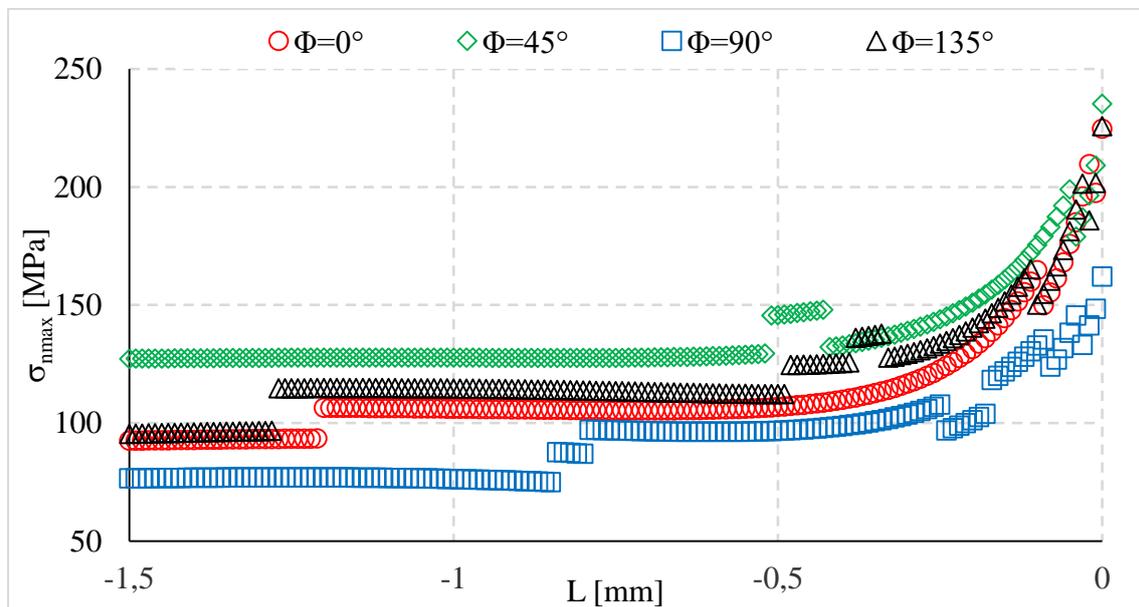
b)   Maximal normal stress along depth.

Figure 5.6. Calculation of driving stresses along depth, for different phase angles.

Note that this curves are only relevant when using the MWCM, as for others criteria, the critical plane has been defined otherwise. According to previous results, the stresses have been calculated at the trailing edge for $\Phi=0°$, $\Phi=45°$ and $\Phi=90°$, and at the leading edge

for Φ=135°, using the last contacting element with pressure as beginning of the straight line. Mesh is defined using 10μm elements to obtain a better accuracy for life estimations, as commented in Section 5.2.1.

5.2.5 Phase angles with mirrored pattern

It has been noted during the stress analysis that the phase angles Φ=45° and Φ=135° have a mirrored pattern. The same can be stated for the phases Φ=0° and Φ=180°. Looking to the forces signals, when the fretting load reaches its maximal value, it appears that the fatigue load has a value in traction for Φ=45° that is equal to the value in compression for Φ=135°. However, these values are smaller than those obtained for the in-phase and the opposition-of-phase loadings, which nevertheless, provide longer lives. Therefore, it is recommended to investigate two others mirrored phase angles surrounding Φ=90°, such as Φ=70° and Φ=105° (as depicted in Fig. 5.7) to verify this trend, and see if these new loadings still damageable for in comparison to the conventional loading.
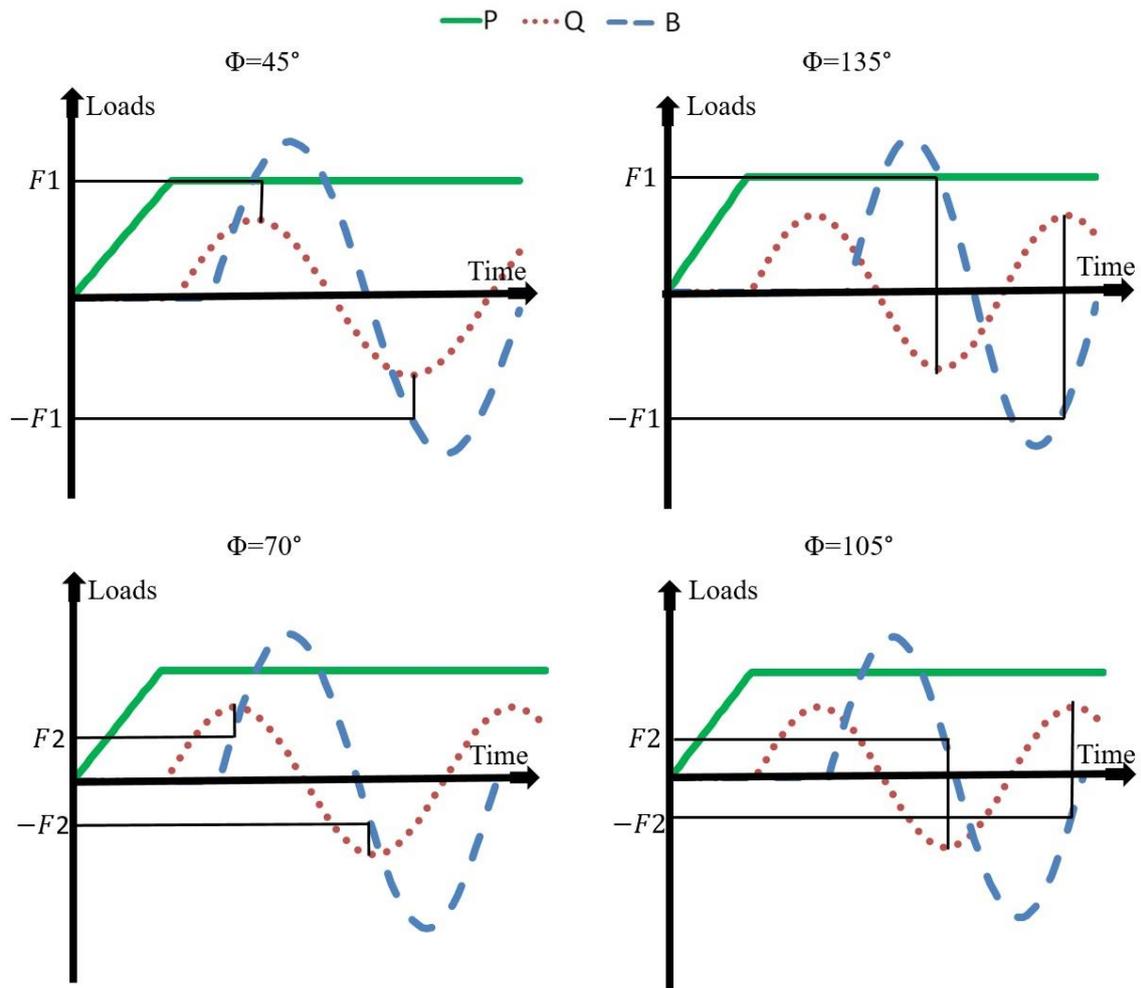
Figure 5.7 Phase angles with mirrored pattern.

5.3 Al7050 fatigue life estimation

The *LvsN* equations used in this study were developed using notched specimens made of Al7050 (see section 3.3.3). Therefore, it is possible to calibrate a curve for one loading condition by testing two specimens submitted to two different stress levels. However, in a work produced at the University of Brasilia [71], 14 fully reversed uniaxial, and 11 fully reversed torsional tests were conducted on V notched specimens, to properly calibrate two *LvsN* equations representative of the two different loading conditions. Six stress levels were investigated for each loading condition to get accurate power law parameters. Furthermore, tests have been repeated. Figure 5.8 presents the *LvsN* curves obtained with these data, that are used to estimate fatigue lives in this study.
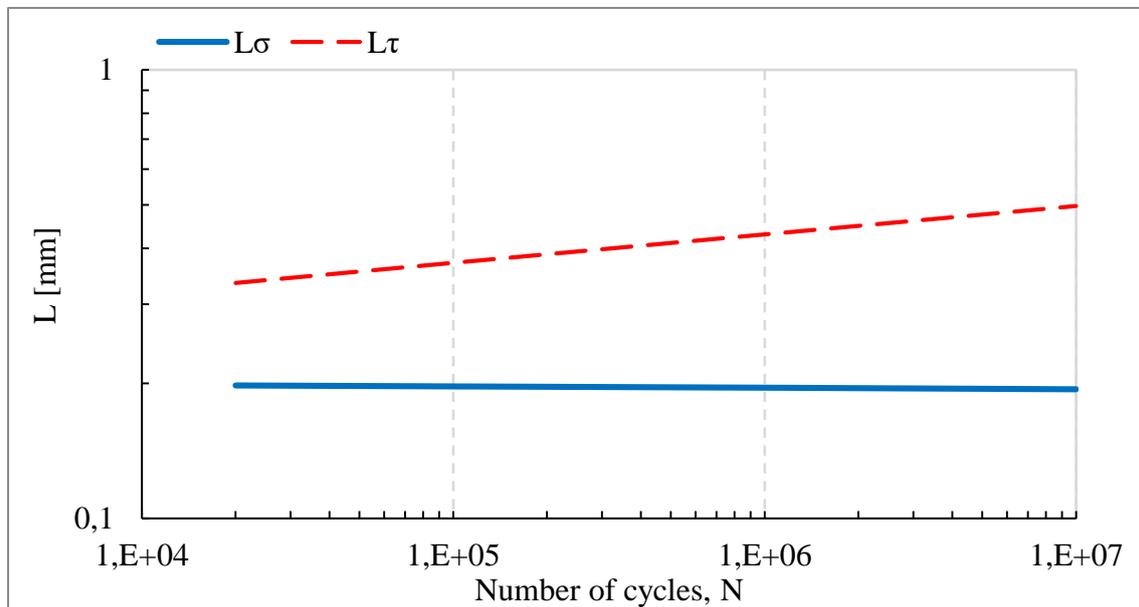
Figure 5.8. *LvsN* calibration using V-notch experimental/numerical data.

The material parameters obtained for application of Eq's. (3.25) and (3.26) were found out to be: $A_\sigma = 0.2041$, $b_\sigma = -0.00314$, $A_\tau = 0.1784$ and $b_\tau = 0,06359$ according to Sá's works [83]. The values of N will be set as the averaged value of experimental lives of Tab. 4.1). that are 94000, 156000, 209000 and 80000 respectively for $\Phi=0°$, $\Phi=45°$, $\Phi=90°$ and $\Phi=135°$. The values of the different critical distances, as function of the phase angle, are given in Tab. 5.5. Note that a third critical distance formulation, which allows the balance of the torsional and uniaxial loadings has been used (see section 3.3.3) setting the parameter w_σ and w_τ initially to 0.5. The stresses values and parameters calculated at these distances for life estimations, are also summarized in Tab. 5.6

Table 5.6 – Critical distances in function of phase angles for the LvsN equation calibrated with V-notched specimens, and associated driving stresses/parameters.

Phase angle	Critical distance[mm]	τ_a [MPa]	$\sigma_{n,max}$ [MPa]	ρ	SWT parameter	FS parameter
$\Phi=0°$	$L_\sigma=0.2$	114	133	1.17	0.297	$5.48*10^{-2}$
	$L_\tau=0.36$	91	112	1.24	0.175	$4.20*10^{-2}$
	$L_{eq}=0.28$	100	119	1.19	0.220	$4.69*10^{-2}$
$\Phi=45°$	$L_\sigma=0.2$	138	153	1.11	0.435	$6.88*10^{-2}$
	$L_\tau=0.38$	115	134	1.16	0.311	$5.60*10^{-2}$
	$L_{eq}=0.29$	126	141	1.12	0.362	$6.19*10^{-2}$
$\Phi=90°$	$L_\sigma = 0.2$	98	103	1.04	0.185	$4.48*10^{-2}$
	$L_\tau = 0.39$	80	100	1.25	0.129	$3.61*10^{-2}$
	$L_{eq} = 0.29$	87	104	1.20	0.149	$3.97*10^{-2}$
$\Phi=135°$	$L_\sigma = 0.2$	119	142	1.20	0.322	$5.81*10^{-2}$
	$L_\tau = 0.37$	93	137	1.47	0.206	$4.50*10^{-2}$
	$L_{eq} = 0.28$	105	131	1.25	0.239	$5.01*10^{-2}$

5.3.1 Al 7050 life estimation using the SWT criterion

The first attempt to estimate fatigue life were done using the SWT criterion, for which the critical plane is defined as the one that possesses the maximal product of $\sigma_{n,max}$ and $\sigma_{n,a}$. Estimated lives were obtained using Eq. (3.10) and setting parameters A_{swt} and b_{SWT} to respectively 4.5 and -0.75 [71]. Results are presented in Fig. (5.9) showing the experimental life against the estimated life in a *log-log* graph.

In figures presenting experimental against estimated life, the central thick line represents an ideal estimation (m=1), the external thin lines represent a difference of factor 2 (m=2) between estimations and experiments, and the dash lines denote a factor 4 (m=4). Note that the same nomenclature has been used for each phase angle for clearness reasons, but referring to experimental lives depict by the ordinate axe, results for $\Phi=135°$ can be find at the bottom of the graph, for $\Phi=0°$ points are encountered very close to the 10^5 horizontal line, then comes the points for $\Phi=45°$, while the highest points represent results for $\Phi=90°$. However, regarding the estimations obtained with the SWT method

(Fig. 5.9), every prediction was highly overestimated for all conditions making this criterion unfitted to this type of analysis.
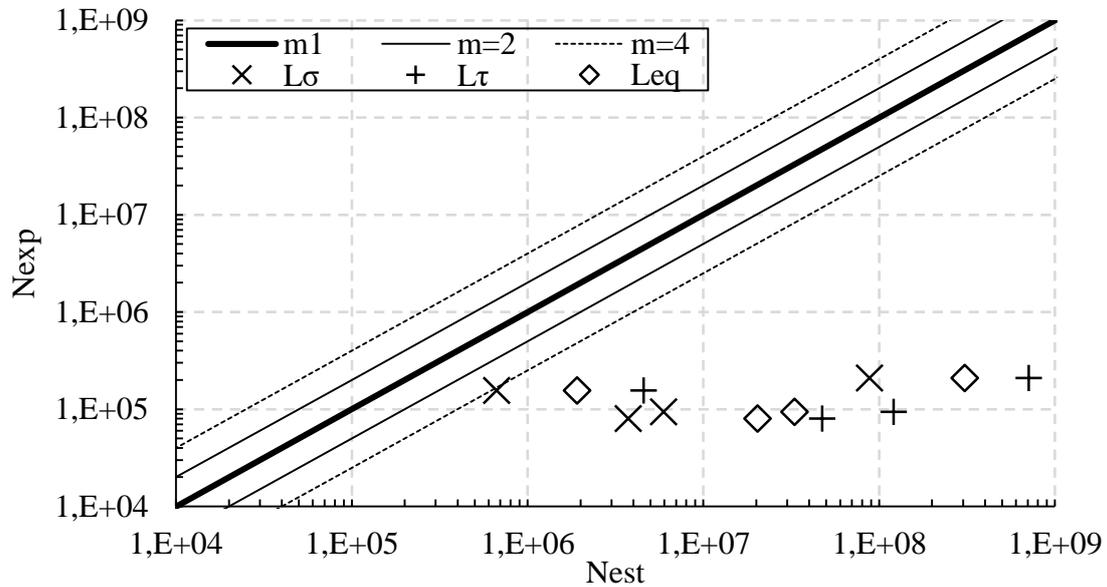
Figure 5.9. Fatigue life estimation according to SWT criterion.

5.3.2 Al 7050 life estimation using FS criterion

The second criterion used to estimate fatigue life is the Fatemi-Socie criterion which considers the critical plane as the one where the FS parameters, Eq. (3.12), is maximal. This formulation clearly assumes that τ_a is the main driving parameter. Estimated lives were obtained using Eq. (3.14) and setting parameters A_{swt} and b_{SWT} to 0.0226 and -0.137 respectively [71]. Results are given in Fig. (5.10).
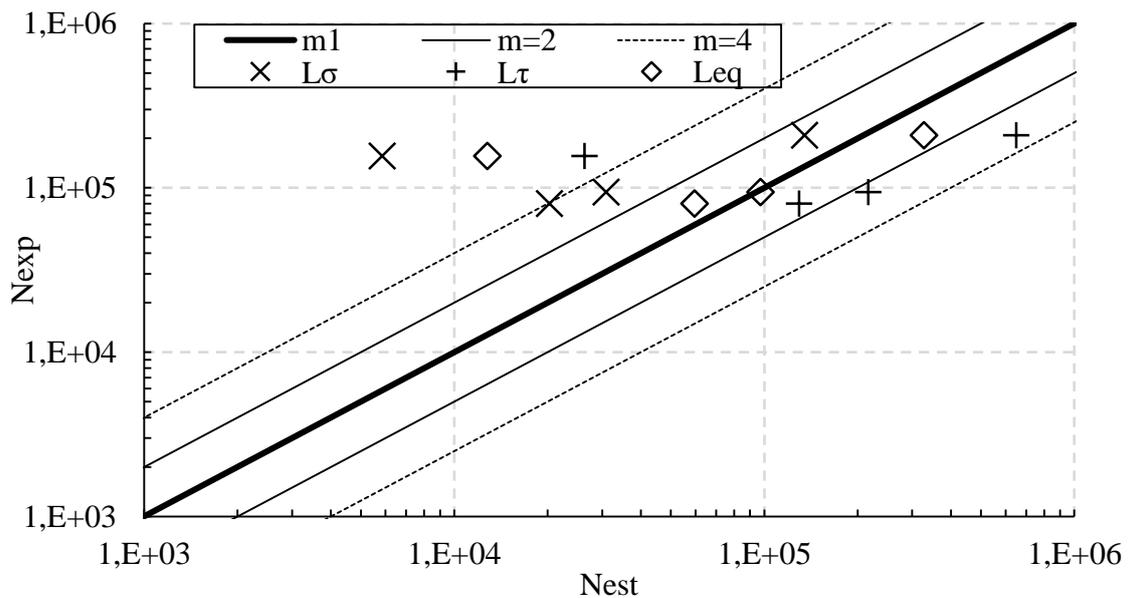
Figure 5.10. Fatigue life estimation according to FS criterion.

The experimental data and estimations with the FS criterion are in excellent agreement for $\Phi= 0°$, $\Phi= 90°$, and $\Phi= 135°$. Indeed, for those loading configurations, the critical distance formulation with torsional calibration shortly overestimates the prediction while the traction calibration shortly underestimates the prediction. Adjusting the weight coefficient of traction, w_σ, in Eq. (3.27) allows a precise estimation. For instance, setting $w_\sigma = 0.5$ for $\Phi= 0°$, $w_\sigma = 0.75$ for $\Phi= 90°$ and $w_\sigma = 0.3$ for $\Phi= 135°$ gives an exact prediction. The numerical results for the loading configuration $\Phi= 45°$ still give underestimated lives, however, it remains coherent with the stresses analysis of section 5.2. Indeed, the stresses concentrated at the trailing edge for this loading configuration are the highest, very close in value to those obtained at the leading edge for $\Phi= 135°$. The fatigue lives of specimens tested with a phase angle of $\Phi= 45°$ should be, in general, like the ones obtained with $\Phi= 135°$ (see Figs 5.5 and 5.6). Corrective estimations, adjusting the weight parameters w_σ and w_τ of Eq. (3.27), are given in Fig. (5.11).
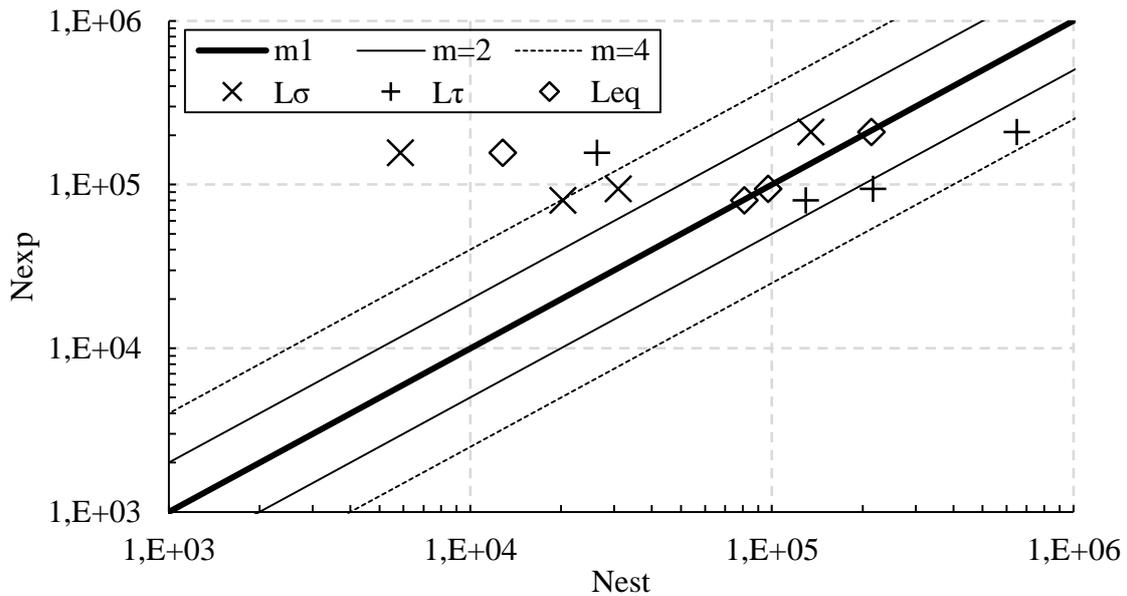
Figure 5.11. Fatigue life estimation according to FS criterion, after adjustment of w_σ and w_τ in the L_{eq} equation.

5.3.3 Al 7050 life estimation using the MWCM

The last criterion used for fatigue life estimation is the MWMC. The critical plane is defined as the one possessing the higher value of the maximal normal stress in between those where the shear stress amplitude is close to its maximal value ($\tau_a = \tau_{amax} \pm 1MPa$). In other words, this method assumes that the shear stress amplitude is the main driving parameter for crack nucleation, but that the maximal normal stress must also been

taken into account. Estimated lives were calculated according to Eq. (3.20). The fatigue curves of the Al7050, obtained under fully reversed torsional and fully reversed uniaxial loadings (see Section 4.1.1), were use as references curves, to obtain the shear stress and the negative inverse slope values for the stress ratios encountered at the critical distances. The modified Wöhler curve diagram build for this work is presented in Fig 5.12, and the coming out estimated lives are given in Fig 5.13.
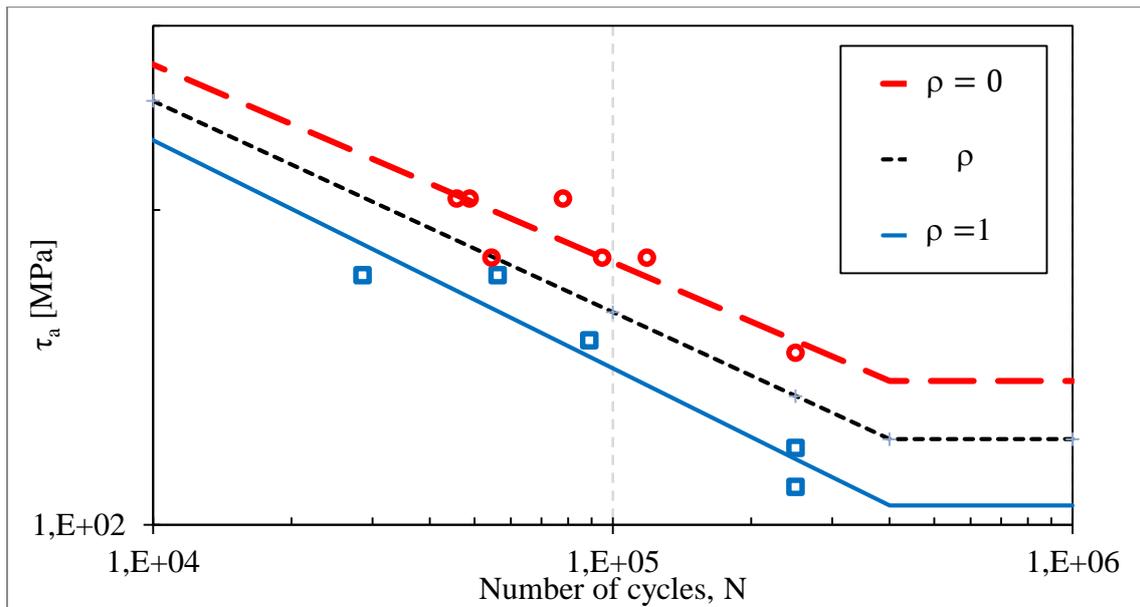
Figure 5.12. Modified Wöhler Curve diagram using the fatigue curves obtained under fully reversed torsional and fully reversed uniaxial loadings as reference curves.
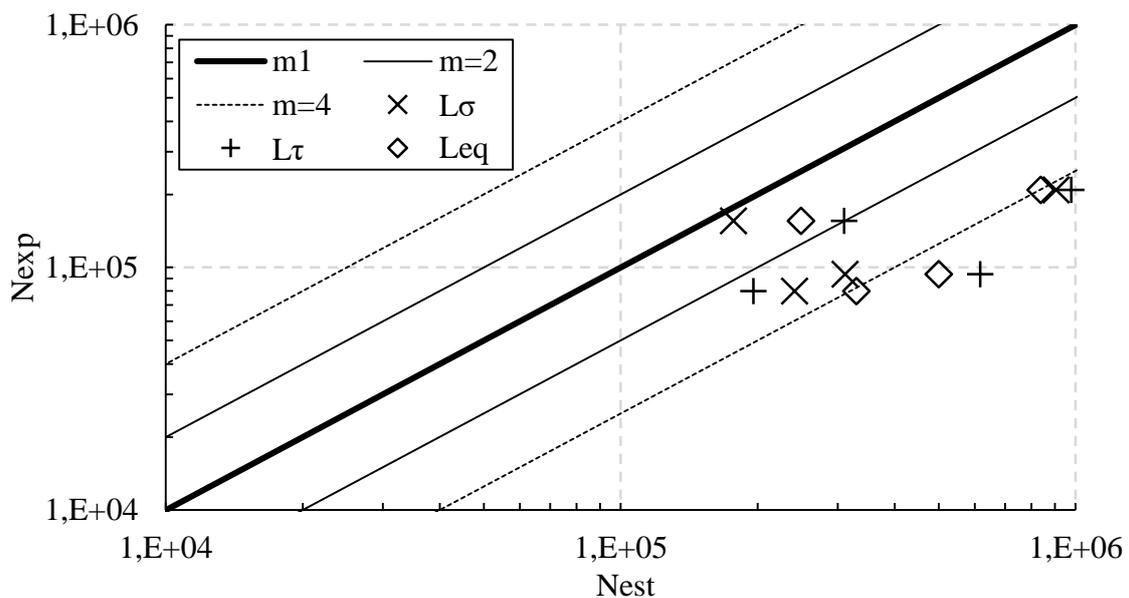
Figure 5.13. Fatigue life estimation according to the MWC method.

Results obtained with MWCM show life predictions that are shortly overestimated for all investigated phases. Estimations for $\Phi= 45°$ are the best ones as they are in between the m=1 and the m=2 lines for the three formulations of the critical distance. The predictions still acceptable even when loads are applied with $\Phi=135°$ as the estimations remain between the m=2 and m=4. However, with the current formulation of the critical distances, the MWMC is not able to satisfactory predict every situation.

In her works, Rossino [85] attempts to estimate the fatigue life of the Al7050 under fretting fatigue loadings using the theory of critical distances with the point formulation. The calibration of the *LvsN* was based on the dynamic material properties (see section 3.3.2). As values of ΔK_{th} are often difficult to encounter in the literature, she formulated two critical distances considering a minimal and maximal value of $\Delta K_{th}(5.5\sqrt{m}$ and $2.0\sqrt{m}$, respectively). It has been chosen to name the associated critical distance L_{min} (0.008mm) and L_{max}(0.056mm) in this analysis. Figure 5.14 shows the estimated fatigue lives calculated for these critical distances.
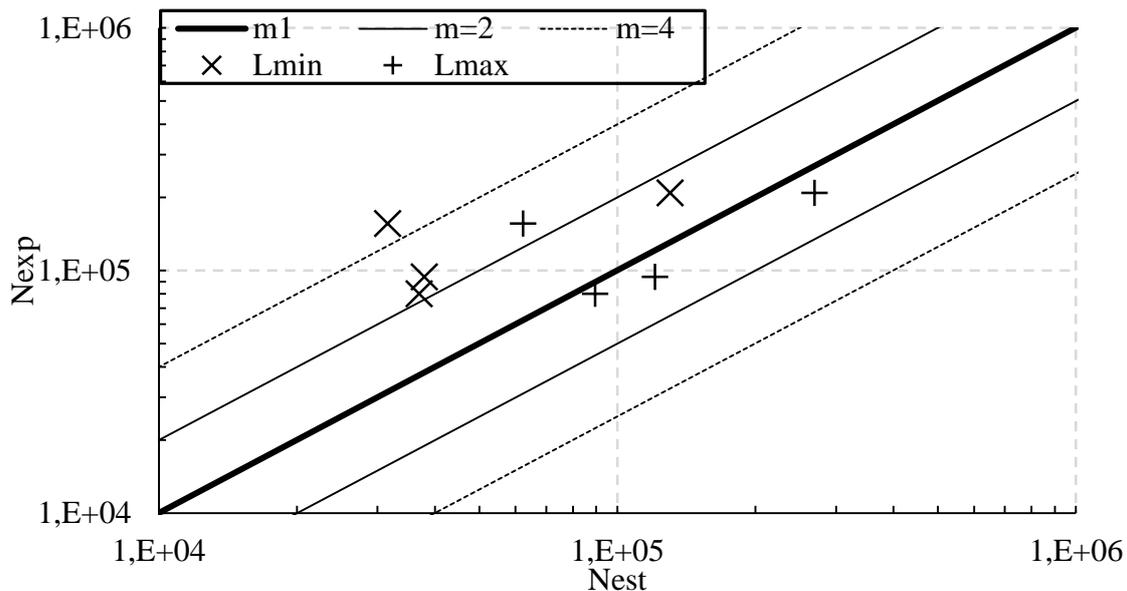
Figure 5.14. MWCM estimations with critical distances based on the material parameters.

Results using the static and dynamic material parameters for the calibration of the critical distances for the MWCM estimations show a good agreement. *Lmin* shortly underestimates the fatigue life, while the *Lmax* value used yields shortly overestimated results. The critical distances leading to the true experimental lives are presented in Table 5.7.

Table 5.7 – Correct critical distances (MWCM) according to simulation, for different phase angles.

	$\Phi=0°$	$\Phi=45°$	$\Phi=90°$	$\Phi=135°$
Critical distance [mm]	0.05	0.165	0.015	0.05

The critical distances are well framed by the minimal (L=0.008mm) and maximal (L=0.056mm) critical distances values calculated in [85] for every phase angle except, $\Phi= 45°$. However, as already discussed in the previous section the experimental lives for this loading condition are in disagreement with the stresses analysis. Furthermore, this critical distance formulation also improves the SWT estimations, giving adequate predictions for $\Phi= 0°$ and $\Phi= 135°$, even for the over-estimated lives obtained for $\Phi= 90°$. On the other hand, this methodology does not fit with the FS criterion, leading to strongly under-estimated results. Note that only Eq. (3.21) has been used for these analyses, so that they remain valid only considering that the material characteristic length L does not vary with life [81].

5.3.4 Comparisons of the Al7050 life estimation results

Three stress-based criteria have been applied in order to estimate the fatigue life. In fact, the Smith-Watson-Topper criterion, governed by the normal stress, gives good predictions for material points located at very short distances from the surface (0.05mm to less than 0.01mm as shown in Fig. 5.15.a), while the Fatemi-Socie criterion, governed by the shear stress amplitude, gives good predictions at quite long distances from the surface (0.25 to 0.3mm as shown in Fig.5.15.b). The Modified Wöhler Curve Method, which employs a combination of the normal stress and the shear stress amplitude to estimate life, gives, naturally, good predictions for intermediate distances, as shown in Fig. (5.15.c).

However, it is vital to correctly guess the fatigue life target before conducting the analyses, and in this way, the critical distance that will provide good estimations must be known in advance. In this work, it has been shown that when the critical distance is calibrated using static and dynamic material parameters, results are very accurate for the MWCM criterion. The combination of this critical distance formulation and this multiaxial stress-based criterion for the life estimations, guarantees an adequate prediction for the materials and phase angles investigated.

In this work, a new formulation of the critical distance has been evaluated. Two LvsN equations were provided by earlier studies developed at the University of Brasilia testing and simulating Al7050 V-Notched specimens, in torsion and in bending. This methodology provided higher values for the critical distances and is incompatible with the SWT and the MWCM criteria. Nevertheless, coupling this formulation with the Fatemi-Socie multiaxial criterion, leads to good predictions for the loading configurations investigated (apart from the controversy lives obtained for the Al7050 with the phase angle Φ=45°). Furthermore, taking advantage of the two different developed equations, that well framed the perfect estimation, this methodology permits to introduce a parameter which vary in function of the phase angle. Indeed, the bending weight parameter ω_σ can be set to 0.5, 0.75 and 0.25 respectively for Φ=0°, Φ=90° and Φ=135°, which is equivalent to set the torsional weight parameter ω_τ to 0.5, 0.25 and 0.75 respectively for Φ=0°, Φ=90° and Φ=135°.
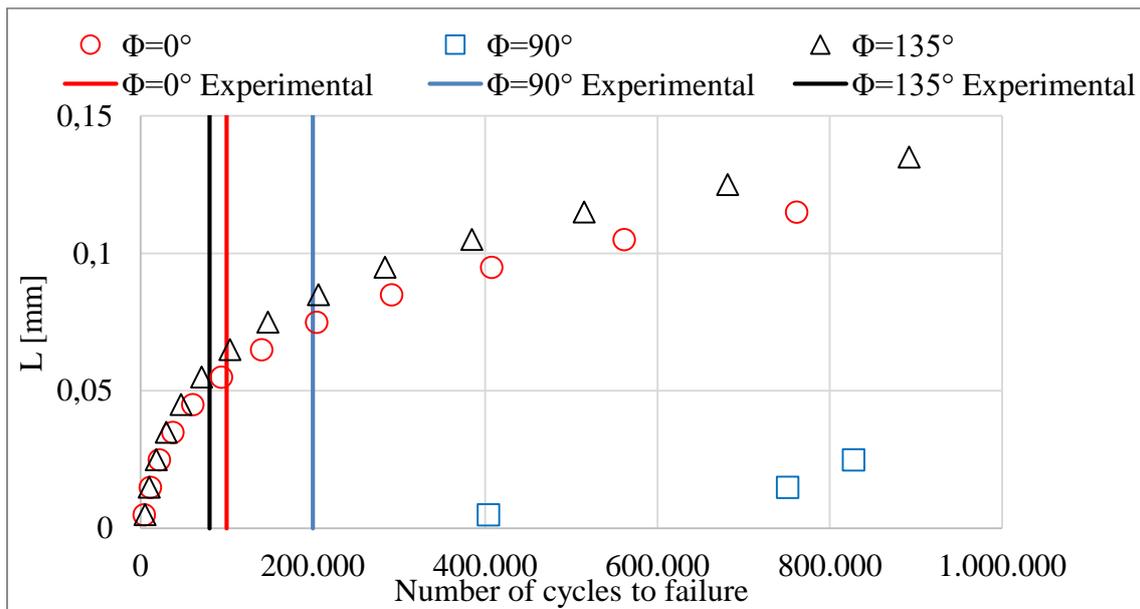
a) SWT life estimations over depth
Figure 5.15 Life estimation over depth: experimental versus numerical results.
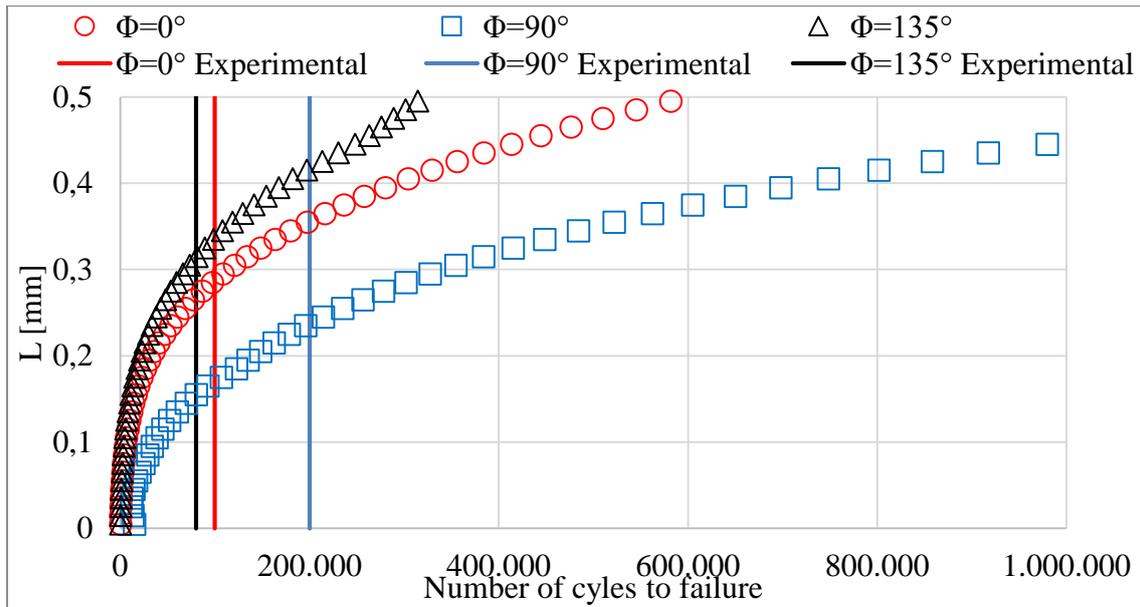
b) FS life estimations over depth
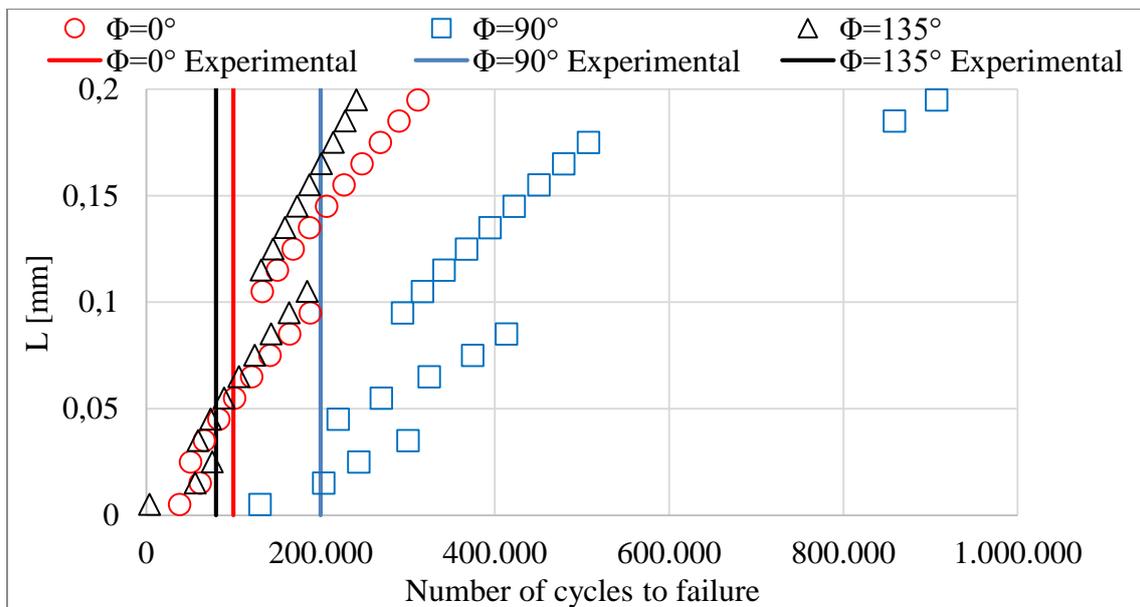
c) MWCM life estimations over depth

Figure 5.15 Life estimation over depth: experimental versus numerical results.

5.4 Al7050 fracture analysis

The experimental results shown that fatigue lives significantly vary in relation to the phase angle, while stress analysis shown that a phase angle of 45° should have given lives similar to those observed phase angle of 135°. The lives estimations for Φ=45° were also rather inconsistent. Therefore, some microscopic observations have been conducted in order to provide additional information regarding these two-phase angles. Observations will focus on the phase angle Φ=45°, establishing comparisons with its mirror

configuration Φ=135°, to find an explanation for the different lives observed between these loading conditions.

5.4.1 Fretted zone analysis

The specimens tested can be separated into two categories. For the first group, the friction marks are located at the top of the failure, while for the second group, they are located at the bottom. These positions correspond to the extremities of the contact, $x/a = -1$ and $x/a = +1$, respectively called trailing edge and leading edge. It is interesting to note that the edge where the failure occurs can directly be correlated to the phase angle. Indeed, for the specimens tested in phase or with a phase angle of 45° the crack initiates at the trailing edge, while for the specimens tested with a phase angle of 135°, the crack initiates at the leading edge (see Fig.5.16). Concerning the specimens tested under the condition of Φ=90° the failure occurs once in the position $x/a = -1$, and once in the position $x/a = 1$. These observations are in good agreement with the stresses analysis.
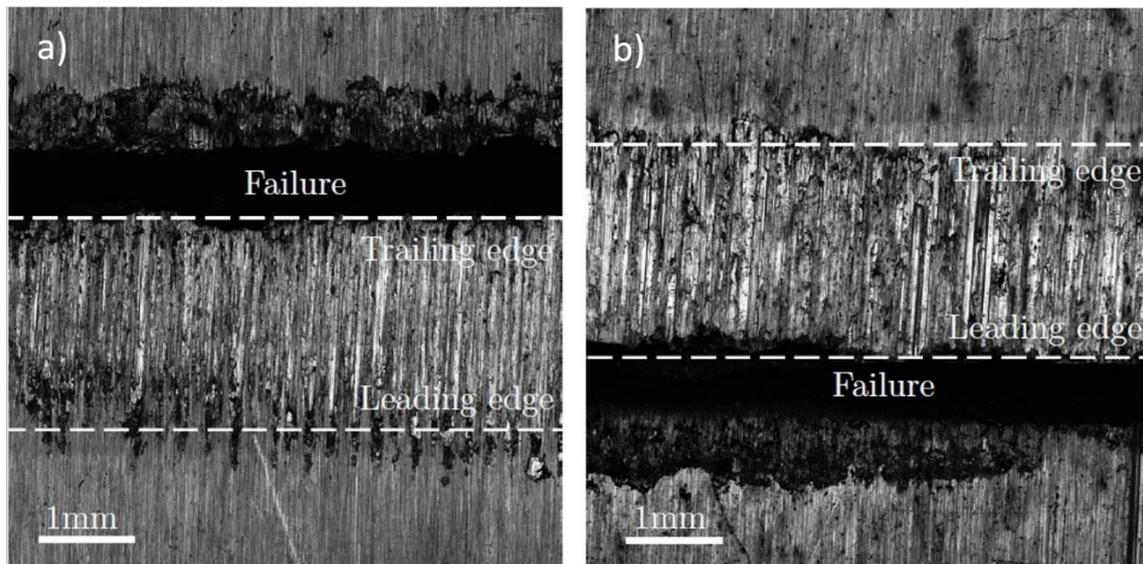
Figure 5.16. Visualization of a) failure occurring at the trailing for Φ=45° and b) at the leading edge for Φ=135°.

Table 5.8 – Failure location.

Phase	Trailing edge	Leading edge
Φ=0°	XX	
Φ=45°	XX	
Φ=90°	X	X
Φ=135°		XX

5.4.2 Cracks profile analysis

As described in Fig. 4.23, the crack profile has been analyzed, looking at the sides of the samples cut from the specimens, and measuring the crack angle of both sides using the confocal laser microscope. Two representative crack profiles with measurement lines are depicted in Fig. 5.15. The evaluation of the crack angles was performed as follows:

1) The crack width, c_w, between the front face of the specimen and the end of the ductile fracture zone is measured 5 times for each specimen and an average value is computed (see representative profile depicted in Fig. 5.17 and Tab 5.9);

2) The average crack width is divided into three equally spaced zones which are used as references for the angle measurements (Fig. 5.18 and Tab 5.9);

3) The average crack angle, c_α, for each side of the sample is computed (Tab.5.9).
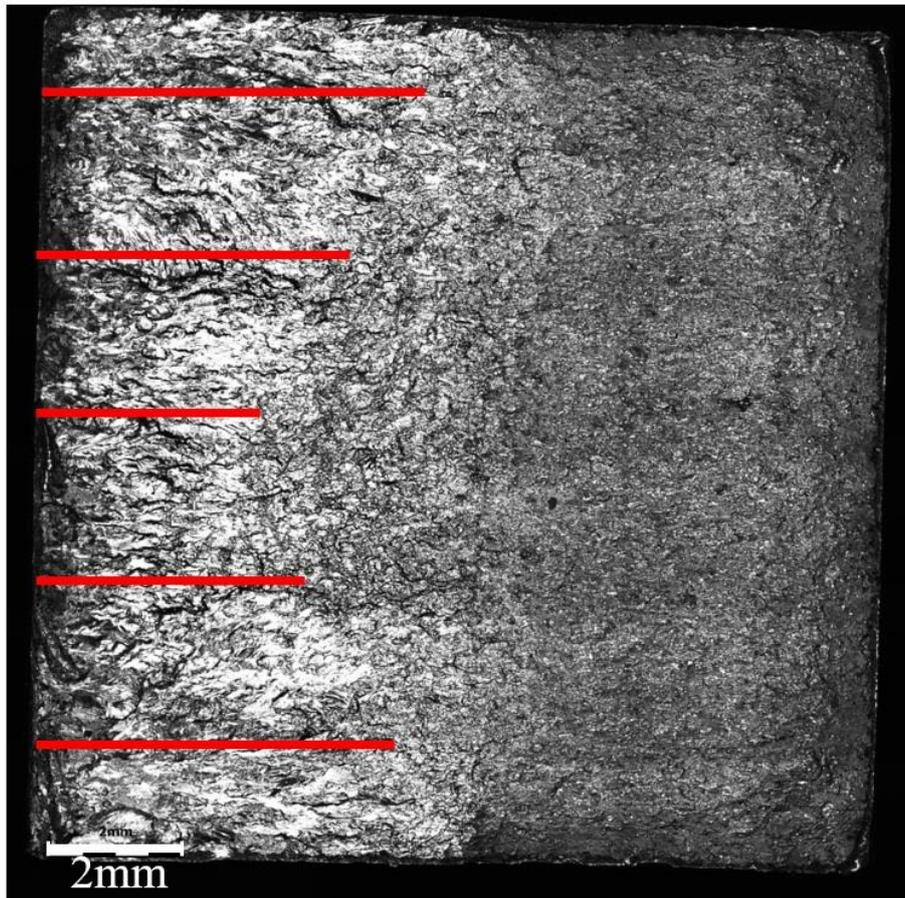
Figure 5.17. Procedure for C_w calculation.
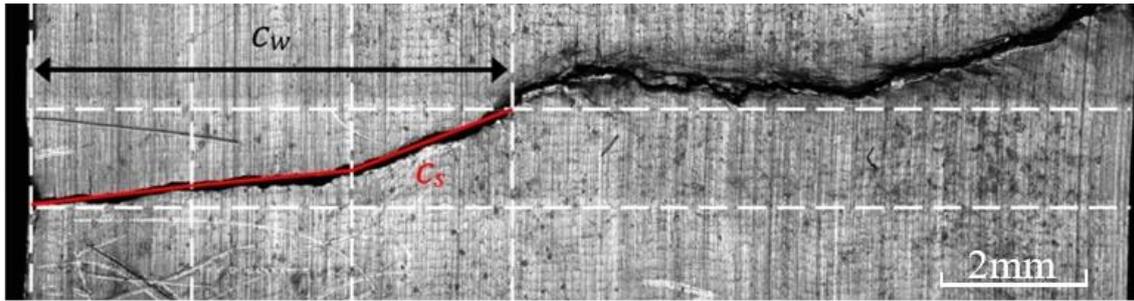
a) $\Phi=45°$, right side measurement of series 1 samples.
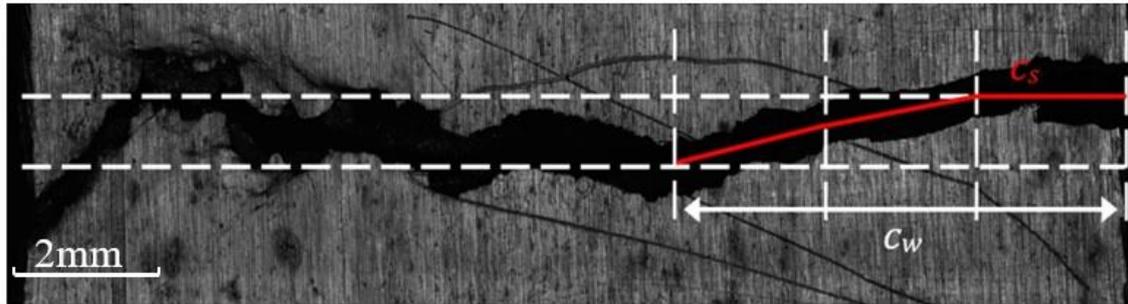
b) $\Phi=135°$, left side measurement of series 2 samples.

Figure 5.18 Procedure for the evaluation of crack angles.

The angles measured at each side of the samples as well as the crack sizes are listed in Table 5.9.

Table 5.9 – Crack profile angles.

Series	Side	c_α (°)		c_w(mm)	
		$\Phi=45°$	$\Phi=135°$	$\Phi=45°$	$\Phi=135°$
1	Right	6.65	1.32	5.94	6.82
	Left	7.48	4.73	5.97	6.85
2	Right	11.25	9.82	5.77	5.47
	Left	-0.34	-6.38	5.62	5.47

It can be observed that the crack angles obtained for $\Phi=45°$ are significantly more pronounced than the ones given by $\Phi=135°$. In fact, the average crack angle for $\Phi=45°$ is equal to 6.26° which is 262% of the value observed for the $\Phi=135°$ (2.37°). Furthermore, only a small difference in the crack size, c_w, is observed. Therefore, since the distance transverse by the cracks is similar for both phase angles and the life of the specimens tested in $\Phi=45°$ is much higher, it can be assumed that the path traversed by the crack when a phase angle of 45° is employed is less damaging to the specimen.

The surface roughness of the fracture zone, seen in Fig. 5.19, was analyzed using the arithmetic mean height parameter, Sa. Results are presented in Table 5.10.

a) 3D reconstruction.   b) Height/Depth analysis.
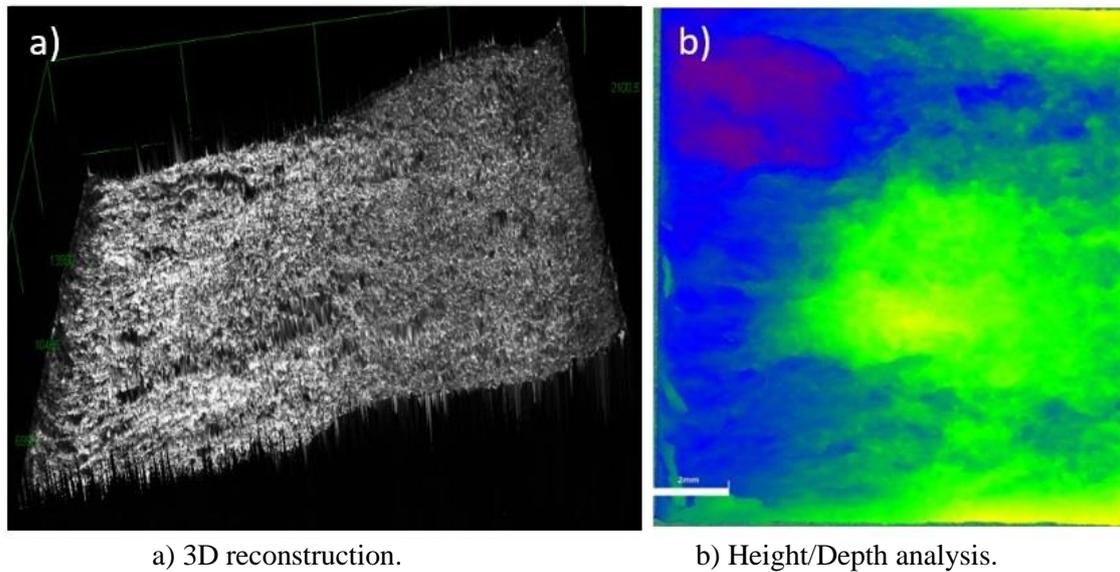
Figure 5.19. Visualization of a sample surface roughness.

Table 5.10 – Surface roughness of the sample using the arithmetic height parameter Sa.

Series	$\Phi=0°$	$\Phi=45°$	$\Phi=90°$	$\Phi=135°$
1	180	195	177	205
2	221	247	194	161

It was observed that the Sa roughness of the fractured surface is insensible to the phase angle, remaining around 200.

SEM images are often useful for failure analysis, as they provide clear indication of the crack initiation zone which can reveal important features of the failure process. The inspected images, Fig. 5.20, were taken on the bottom part of a specimen tested in $\Phi=45°$, and on the top of a specimen tested in $\Phi=135°$ condition. Some crack initiation sites have been identified in both samples, and the fretted zone is clearly detailed on the $\Phi=45°$ sample and slightly less evident on the $\Phi=135°$ sample. As mentioned previously, the Sa roughness of all fractured specimens were alike. However, it can be observed, in Fig. 5.18a, that the surface of the region next to the crack initiation zones is much more intricate. These lumps and ridges are signs of additional resistance to the propagation of cracks, which reinforce the hypothesis that cracks for $\Phi=45°$ configuration traversed a more unyielding path during its propagation.
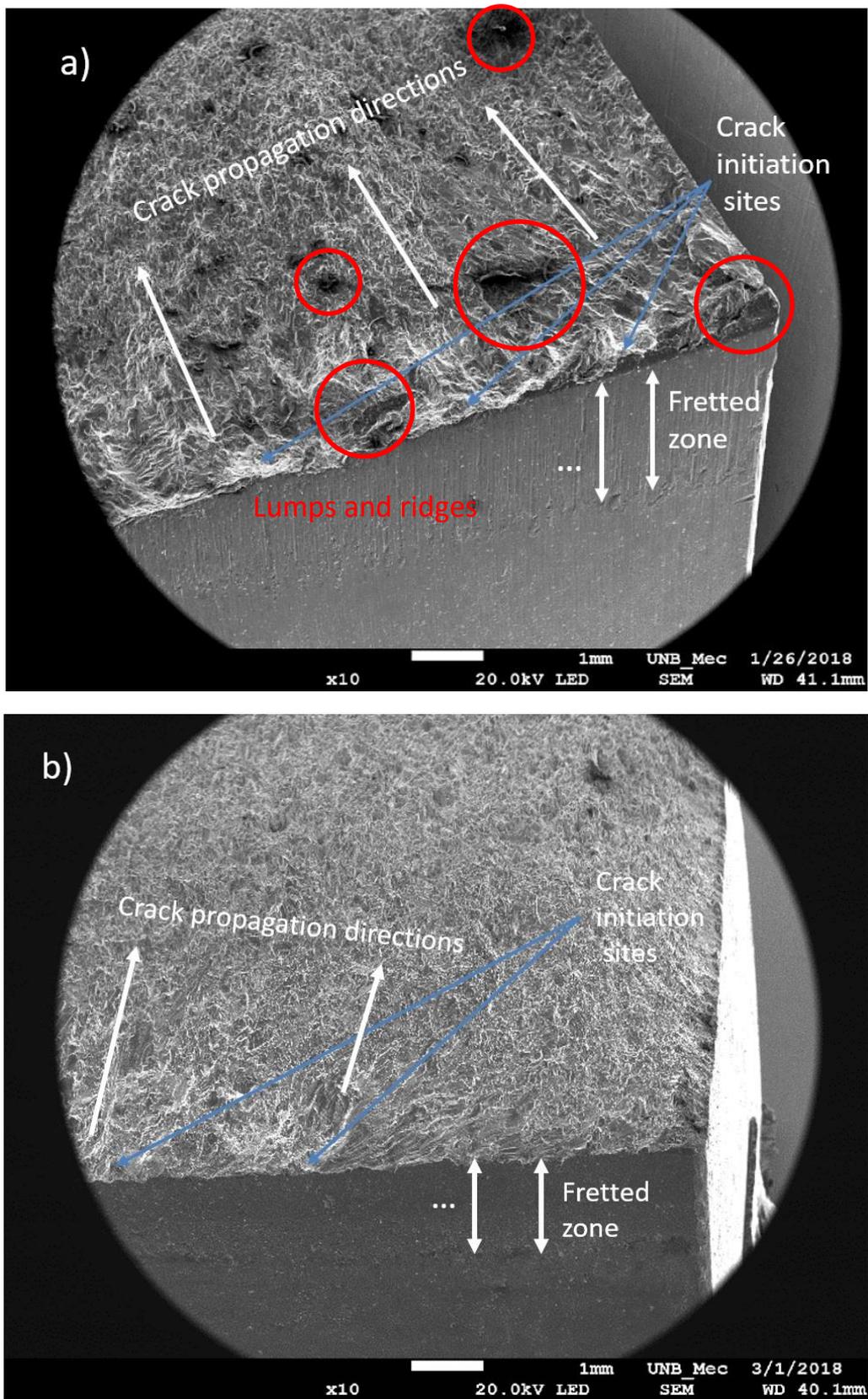
Figure 5.20. SEM observation of a) bottom sample failed under the condition Φ=45° and b) upper sample failed under condition Φ=135°.

Chapter 6. Phase angle effect on the CA6NM

This chapter aims to verify if the long experimental lives observed for the Al7050 using $\Phi=45°$ are intrinsic to that material or if another material, the CA6NM, also presents such behavior. This is motivated by the lack of correspondence between numerical e experimental results concerning this phase angle. The mirror loading configuration, $\Phi=135°$, is also studied.

6.1 CA6NM numerical results

The numerical model employed for the analysis of the CA6NM was discretized with second order quadrilateral elements, of 10μm size, in the contact zone. The loads values applied to the model were listed in Tab. 4.6. The values of the shear stress amplitude τ_a, and the maximal normal stress $\sigma_{n,max}$, acting in the critical plane were evaluated over depth (Fig. 6.2). These analyses have been conducted at the trailing edge for $\Phi=45°$ and at the leading edge for $\Phi=135°$, according to the results obtained in the previous chapter. It is important to emphasize that the numerical model was also validated for the CA6NM, observing a good agreement between the model and the analytical solution looking to the distributions of normal pressure and the shear traction.
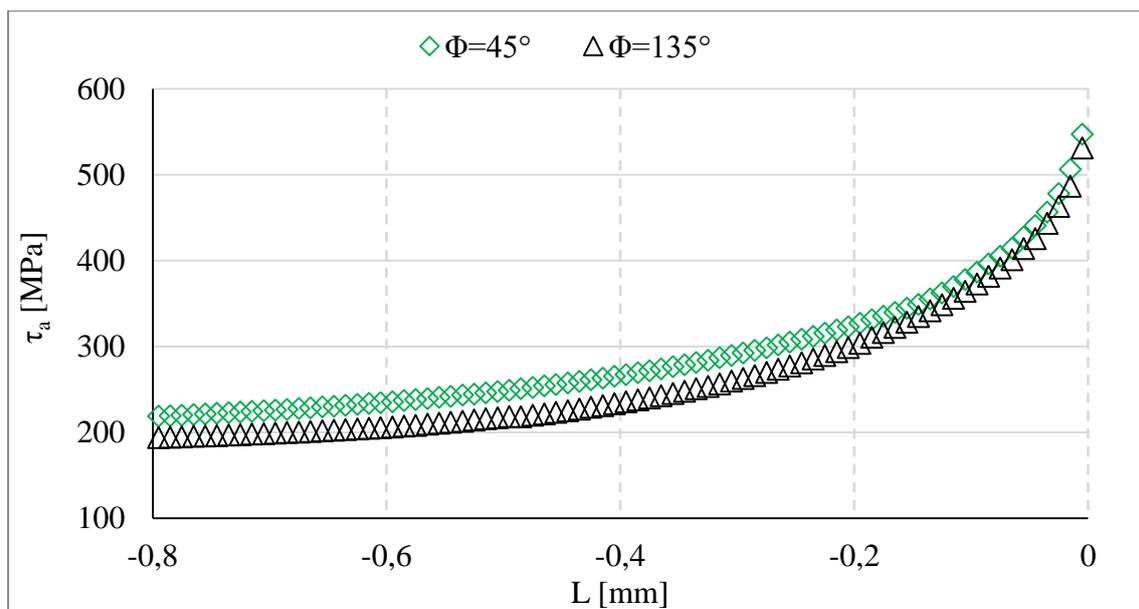
a) Shear stress amplitude over depth.

Figure 6.1. Numerical analysis of the driving stresses for the CA6NM.
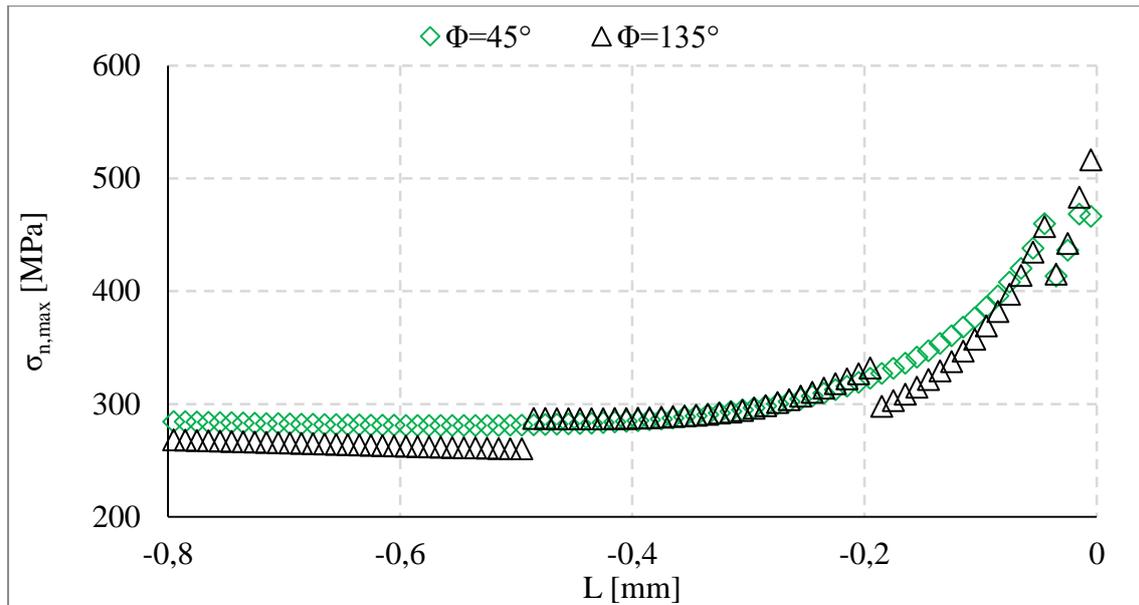
b) Maximal normal stress over depth.

Figure 6.1. Numerical analysis of the driving stresses for the CA6NM.

As results for the Al7050 numerical analysis, the driving stresses calculated at the trailing edge for Φ=45° provide similar behavior than those calculated at the leading edge for Φ=135°. Note that, once again, values of normal stress have been taken has the maximal ones encountered in the material plane where the shear stress amplitude was close to its maximal value. It is then convenient to use the obtained curves for predictions based on the modified Wöhler curve method.

6.2 CA6NM fatigue life prediction

The fatigue lives have been predicted before conducting tests, using the iterative method described in section 3.3.4. The same range of lives that the ones obtained for the Al7050 was targeted for the CA6NM. *LvsN* calibration was conducted using static and dynamic parameters of the material as no data regarding notched specimens could be found in literature. The ultimate yield stress (755MPa) and the fracture toughness ($50\text{MPa}\sqrt{m}$) have been set as static parameters, according to ASTM [88]. Concerning the dynamic parameters, the fatigue limit (10^6) has been set 385 MPa while the threshold intensity factor ΔK_{th} has been set to 7.7 according to Silva [93] and De Souza works [98]. Figure 6.1 shows the *LvsN* log-log graph calibrated using the methodology described in section 3.3.2.
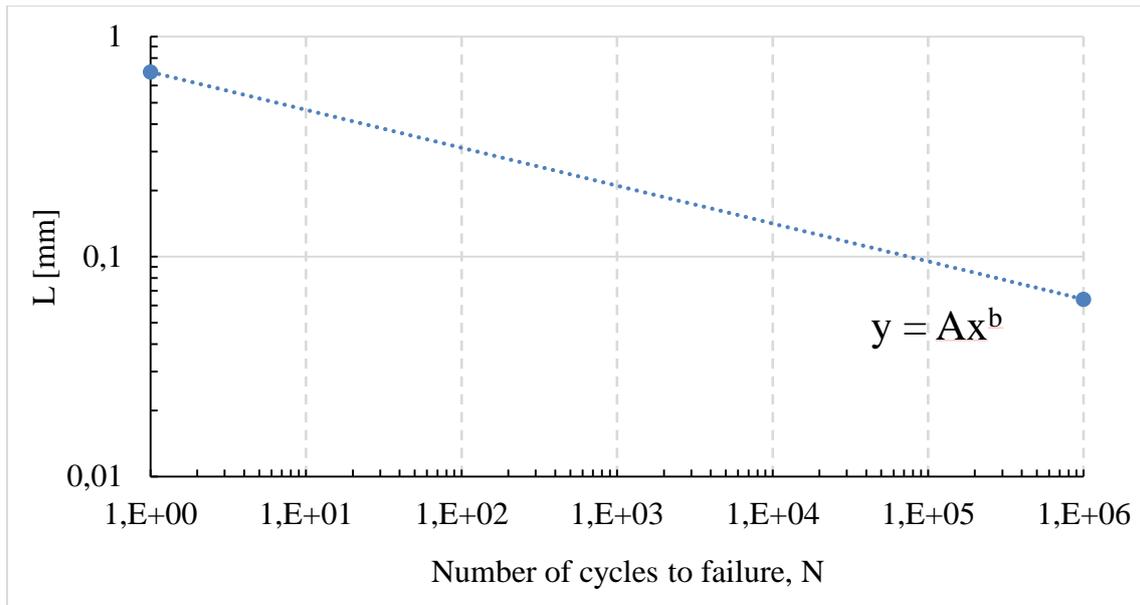
Figure 6.2. CA6NM *LvsN* behavior (A=0.69 and b=-0.172).

The modified Wöhler curve diagram (depicted in Fig. 6.3) has been built according to the uniaxial fatigue curves presented in Fig. (4.5). The stress ratios given by Eq. (3.18) are equal to $\rho = 2$ and $\rho = 1$ for the load ratios $R = 0$ and $R = -1$, respectively. The number of cycles to failure N_a that corresponds to the shear stress reference has been fixed to 10^6, and the values of $\tau_{a,ref}$ and κ have been identified for both curves. A linear interpolation of these values for the stress ratio ($\rho = \sigma_{n,max}/\tau_a$) calculated in the process zone, allows the estimation of the fatigue life according to Eq. (3.20).
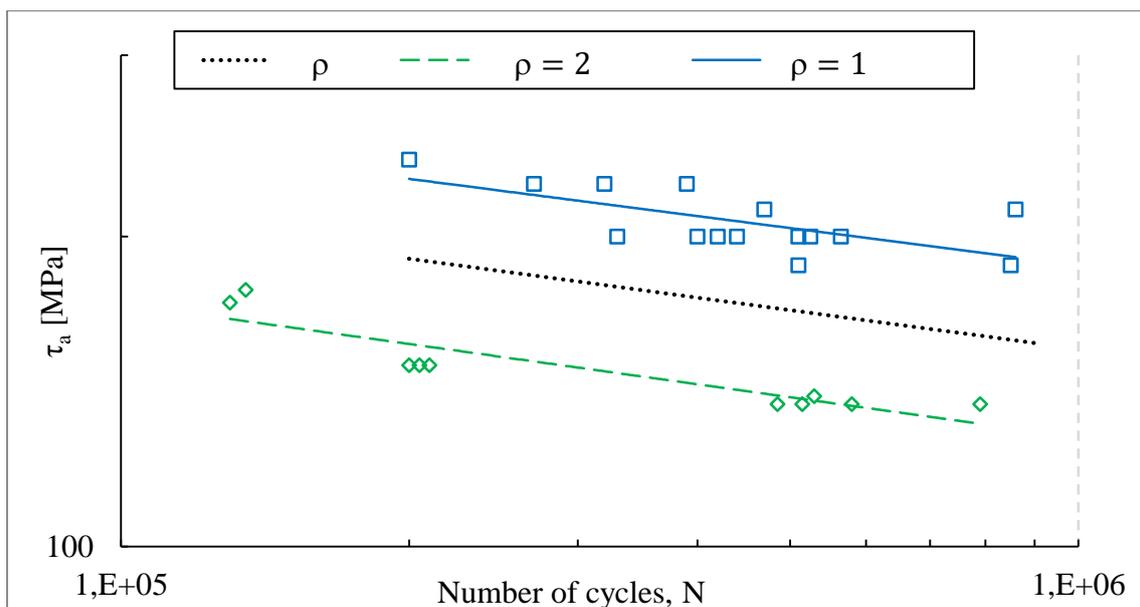
Figure 6.3. MWMC diagram for the CA6NM.

Once the driving stresses and the stress ratio known for each point over depth, the iterative process described in Section 3.3.4 has been applied. In between every iteration, the *LvsN* equation provided in Fig 6.1 has been used to calculate the critical distance where the fatigue life must be estimated. The predictions obtained with this method yielded lives of 132000 cycles and 111000 cycles for $\Phi=45°$ and $\Phi=135°$, respectively, which correspond to the range of life targeted.

6.3 CA6NM experimental fatigue life

Two series of tests were conducted for $\Phi=45°$ and $\Phi=135°$. Herein, the loads values listed in Tab. 4.5 were applied, and the procedure described in Section 4.2 was rigorously followed. All experiments with the CA6NM were conducted using a frequency of 2Hz. Note that, for the CA6NM, more cycles are required for the "pre-test" to establish a stable friction coefficient when compared to the Al7050. For the pre-test of this material, 25000 cycles are necessary, and these cycles are disregarded during the experimental life analysis. The lives obtained for the CA6NM are depicted in Fig. 6.4 and listed in Tab. 6.1.
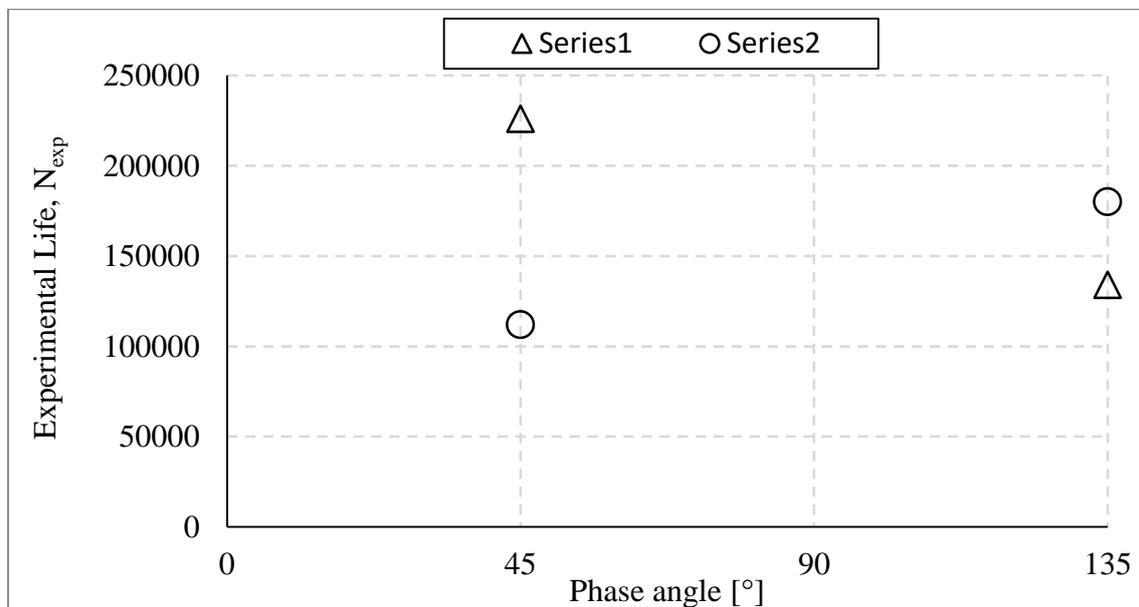
Figure 6.4. Experimental lives behavior of the CA6NM for $\Phi=45°$ and $\Phi=135°$.

Table 6.1 – Experimental lives data of the CA6NM for Φ=45° and Φ=135°.

Series	Φ=45°	Φ=135°
1	112000	180000
2	226000	134000
Average	169000	157000
Standard deviation	57000	23000

Higher deviation was observed than for the Al7050, but however it remains very acceptable for fatigue data. Furthermore, the average lives for this condition fall in a close agreement with its mirror loading (Φ=45°), and are also in accordance with the numerical estimations. Such results indicate that both the iterative method combined with the MWCM [74] and the *LvsN* equation calibrated with material parameters can provide precise estimations for fretting fatigue tests with a phase angle between fretting and bulk loads. More important, the experimental lives of the two mirrored loading conditions match with the stress analysis developed during this study. Nevertheless, it is important to conduct additional tests, in Φ=45° for a better assessment of its behavior, and in the remaining loading conditions Φ=0° and Φ=90 for a complete analysis.

6.4 CA6NM failure analysis

Observation of the CA6NM fractures confirmed, once again, that the phase angle of Φ=45° leads to a failure at the trailing edge while Φ=135° provokes a failure at the leading edge, as can be seen in Fig. 6.5.
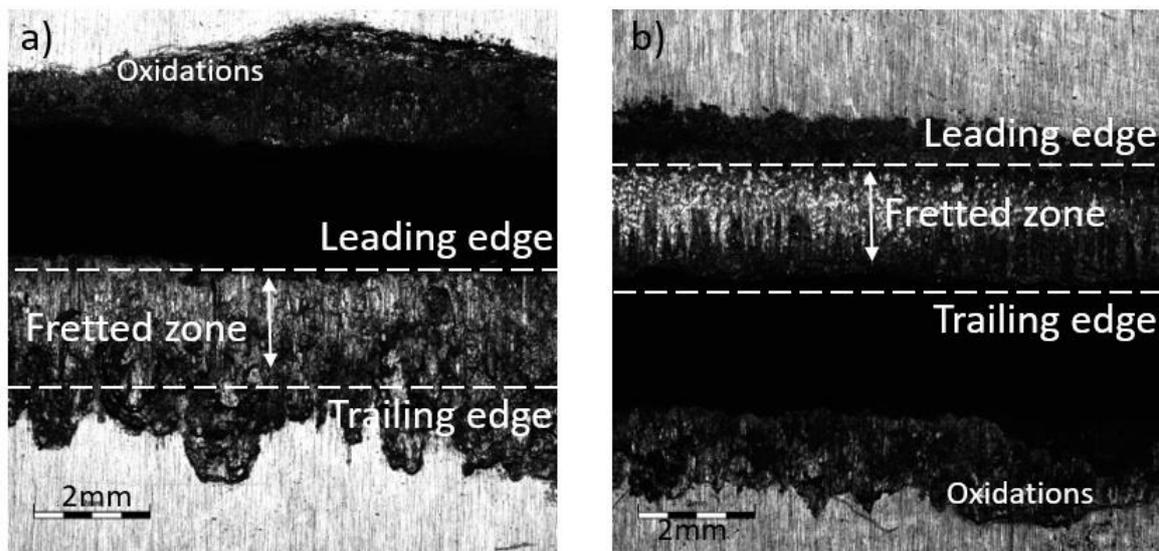
Figure 6.5. Visualization of the failure for a) specimen tested under the condition Φ=45° and b) specimen tested under the condition Φ=135°.

Overall, the crack propagation width for the CA6NM was longer than the ones observed on the Al7050 specimens, measuring in average 8.4±1.4mm for every broken specimen (Fig.6.6. a). Moreover, the pattern of the failure was much more pronounced, as shown in Figure 6.6. b.
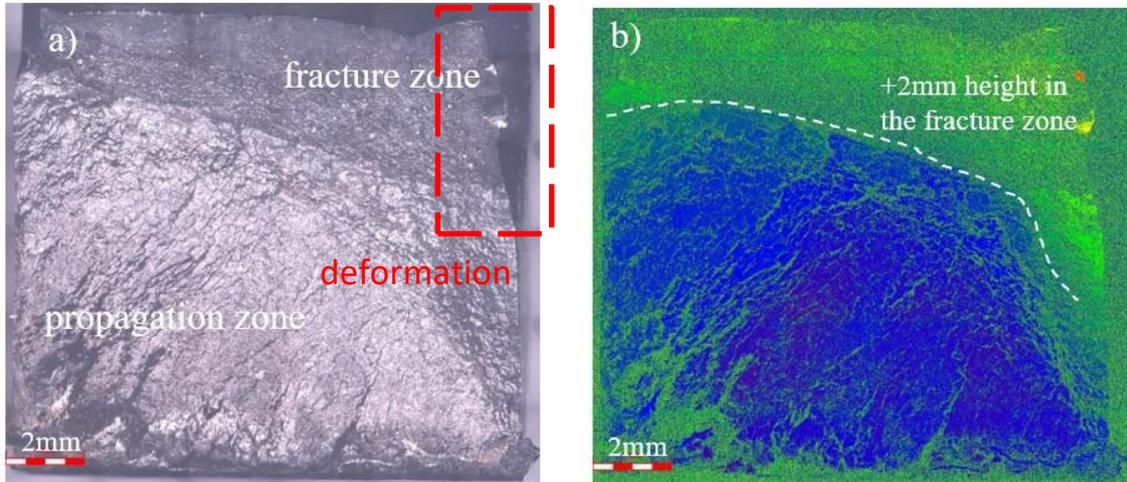
Figure 6.6. Visualization of a) propagation and fracture zones and b) height/depth analysis.

The propagation zone is large while the fracture zone is much smaller and shows signs of severe plastic deformation on its right side (Fig. 6.6a). This drastic failure mechanism lead to a difference of approximately 2mm in the height of the profile, between propagation and fracture zones. Furthermore, the microscopic analysis of the side of the specimens show higher crack angles than those observed for the Al7050, see Fig. 6.7. However, they remained the same for both phase angles, around 24° and nothing else indicates a difference in fracture morphology in this context. Furthermore, the higher orientations of the crack angle observed with this material (25°) are in agreement with Pereira [99] predictions (22°), which reinforce the hypothesis that the lamination process of the Al7050 can influence the experimental results and that the response of this CA6NM is more adequate for this study.
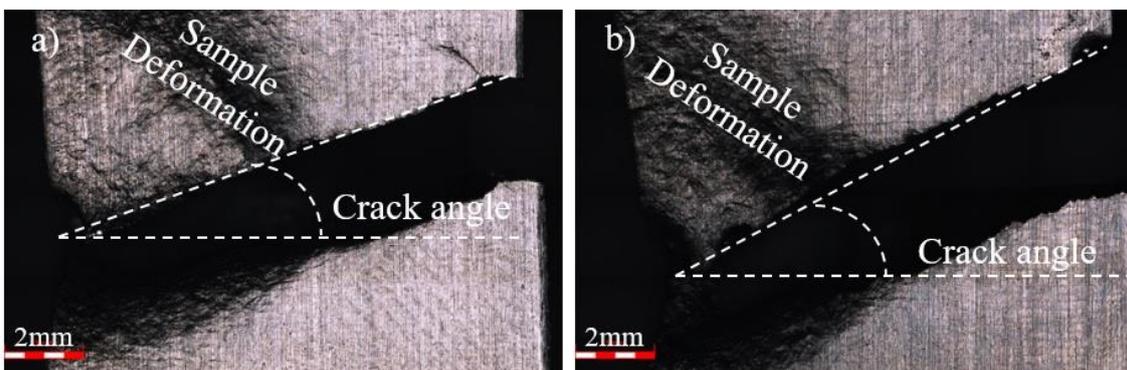
Figure 6.7. Side view of CA6NM fractured specimens. a) Φ=45, and b) Φ=135°.

SEM analysis of the fractures were also conducted for the CA6NM, revealing a concentration of matter in the crack initiation zone, sliding towards the fracture zone and making impossible to visualize the initial crack striations. The high normal load applied to this material, which is the likely cause of the lateral deformation of the specimens, and the more brittle behavior of this material could be responsible for this phenomenon. In a final note, the overall behavior of the CA6NM seems more consistent than the one of Al7050, since a good correlation between the stress analysis, numerical estimation, experimental data and fracture analysis for both the $\Phi=45°$ and $\Phi=135°$ is observed.
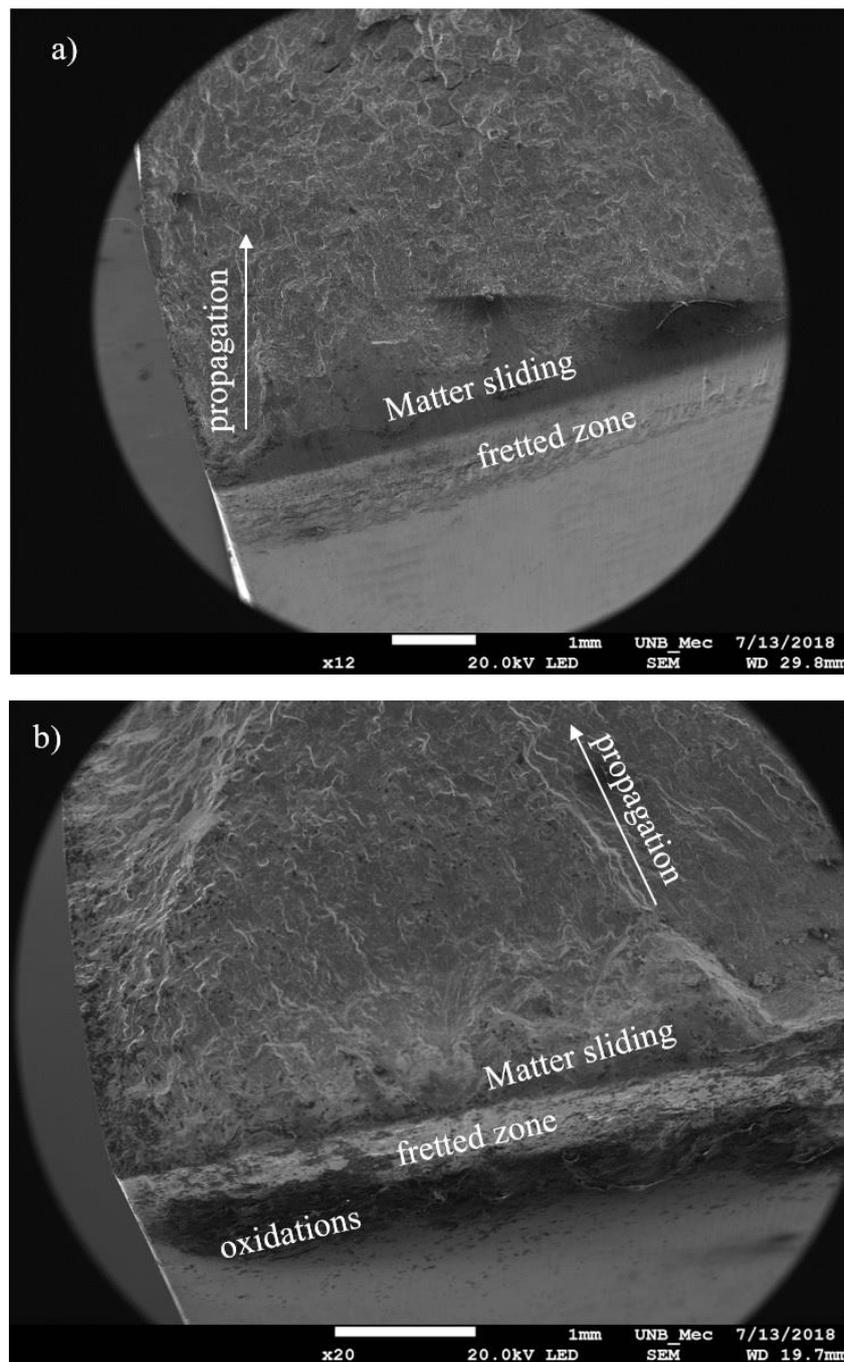
Figure 6.8. SEM failure observation of a) $\Phi=45°$ and b) $\Phi=135°$, broken specimens.

Chapter 7. Conclusion

An overview of the work followed by some final remarks and a brief discussion of recommended future studies is presented.

7.1 Overview

The goal of this work is to verify a potential influence of the introduction of a phase angle between the fretting load and the bulk fatigue load. Three different phase angles ($\Phi=45°$, $\Phi=90°$ and $\Phi=135°$) have been analyzed and results have been compared with the conventional in-phase loading condition ($\Phi=0°$). Complete stress analyses have been performed for these different loading configurations to understand the process induced by phase angles. Experimental tests have been conducted on two different materials, the 7050 T7451 Aluminum alloy and the ASTM 743 CA6NM steel to evaluate the influence of the phase angle on their fatigue lives. Life estimations have been attempt using three different multiaxial criteria (SWT, FS, and MWMC) and two critical distance formulation (one calibrated with an experimental/numerical campaign on V-notched specimens and the other calibrated with static and dynamic materials parameters) to identify the most appropriated method to predict the behavior of specimen submitted to out-of-phase fretting fatigue loadings. Various observations were made during these studies.

7.2 Numerical observations

- Simulations carried out suggest that the phase angle must influence the fatigue life. On one hand, phase angles of $\Phi=45°$ and $\Phi=135°$ present higher stresses in comparison with the reference (in-phase condition). Therefore, it is presumed that their introduction should lead to a reduction of the fatigue life. On the other, a phase angle of $\Phi=90°$ lead to lower stresses and is supposed to exhibit a longer fatigue life.

- A second important observation of this work concerns the stress distribution over the contact zone. It has been shown that stresses are higher at the trailing edge for $\Phi=45°$ loading configuration (as for an in-phase loading), while they are higher at the leading edge for $\Phi=135°$ (as for an opposition of phase loading), which indicates that cracks must nucleate at the opposite side of the contact. Looking to a phase angle of $\Phi=90°$ stresses are well equilibrated at both contact edges so it is

not possible to predict where the crack will nucleate. Furthermore, looking to the center of the contact, the stress distributions are mirrored for the phase angles $\Phi=45°$ and $\Phi=135°$, as for $\Phi=0°$ and $\Phi=180°$.

- The bulk load affects the shear traction distribution on the left side of the contact for $\Phi=45°$ and on the right side for $\Phi=135°$, while for a phase angle of $\Phi=90°$ it seems to have no effect. In fact, when the fretting load reach its maximal loading time ($\pi/2$), the fatigue load is in a loading state for a phase angle of $\Phi=45°$, in an unloading state for a phase angle of $\Phi=135°$ and null for a phase angle of $\Phi=90°$. The different directions of the bulk load when the tangential load is maximal must be responsible for these "reversed" stresses. Moreover, at $\pi/2$, the fatigue load for both $\Phi=45°$ and $\Phi=135°$ phase angles has an equal magnitude.

7.3 Experimental observations

- Analysis of the experimental data for the Al7050 specimens shows that a phase angle of $\Phi=90°$ introduced on the bulk load improved the fatigue life on almost 100%, while a phase angle of $\Phi=135°$ reduced it of about 20% of the reference value. More surprising, a phase angle of $\Phi=45°$ brings the fatigue life from 100000 cycles to 150000 cycles which is incoherent with the numerical observations.

- Complementary tests conducted using CA6NM specimens showed fatigue lives similar in value for $\Phi=45°$ and $\Phi=135°$. The lamination process of the Al7050 could have influence the experimental results and the response of the CA6NM seems more appropriated for this kind of loadings.

- Another important result confirmed by the fracture analysis, is that cracks nucleate at the top of the fretting mark for every specimen tested in-phase or in $\Phi=45°$, and at the bottom of the fretting mark for $\Phi=135°$. These positions correspond respectively to the trailing and the leading edges of the contact. Concerning the phase angle $\Phi=90°$, failures occur at both sides of the contact. These observations are in good agreement with the numerical results and are valid for both materials investigated.

7.4 Fatigue life estimations

- In this work, a new formulation of the critical distance has been evaluated. Two LvsN equations were provided by earlier studies developed at the University of

Brasilia testing and simulating Al7050 V-Notched specimens, in torsion and in bending, providing high values for the critical distance. Coupling this formulation with the Fatemi-Socie multiaxial criterion, leads to good predictions for the loading configurations investigated. Furthermore, taking advantage of the two different developed equations, that well framed the perfect estimation, this methodology permits to introduce a parameter which vary in function of the phase angle.

- The Smith-Watson-Topper criterion, gives good prediction for materials points located at very short distances from the surface, even smaller than the mesh size used in this work and no critical distance formulation permit to correctly estimate the fatigue life using this criterion.

- The Modified Wöhler Curve Method, which employs a combination of the normal stress and the shear stress amplitude to estimate life, gives, naturally, good predictions for intermediate distances. It has been shown that results are very accurate for the MWCM criterion, when the critical distance is calibrated using static and dynamic material parameters.

7.5 Future works

It has been revealed that the stainless steel studied here provides results more coherent with the theory and the numerical model when compared to the aluminum alloy tested. Nevertheless, additional tests with this material as well new materials with high stiffness (to avoid the frequency issues observed with the Al7050) are highly recommended. It could be interesting to investigate intermediate phase angles, such as $\Phi=70°$ and $\Phi=105°$ to see if these loading configurations are also mirrored, and if they reduce or improve the fatigue life following the trends observed. This would enable a more precise depiction of the phase angle influence, especially around $\Phi=90$, which provided the highest fatigue lives. Finally, it will be interesting to bring the results to industrial applications, were parts fail due to fretting fatigue. Note that being able to introduce and maintain a phase angle of $90°$ between the bulk and the tangential loads could greatly improve the service life of mechanical components submitted to fretting fatigue.

REFERENCES

[1] Bellecave, Y., (2015), *Stress gradient in fretting fatigue*, University of Brasilia Thesis.

[2] Kalombo Badibanga R., (2017), *Evaluation of the fatigue resistance of power line conductors function of the H/w parameter*, University of Brasilia Thesis.

[3] Sá M.V.C., Ferreira J.L.A., Da Silva C.R.M., Araújo J.A., (2018), *The role of the shear and normal stress gradients on life estimation of notched Al7050-T7451 under multiaxial loadings*, Theoretical and Applied Fracture Mechanics, pp 38-47

[4] Winck L.B., Ferreira J.L.A., Araujo J.A., Manfrinato M.D., da Silva C.R.M., (2013) *Surface nitriding influence on the fatigue life behavior of ASTM A743 steel type CA6NM* Surface and coatings Technology, V. *A fatigue model for sensitive materials to non-proportional loadings* 232, pp 844-850.

[5] Eden, E.M., Rose, W.N., and Cumningham, F.L. (1911). *The endurance of metals,* Proceedings of the Institute of Mechanical Engineers, V.4, pp. 839-974.

[6] Gillet H.M. Mack E.L., *Notes on some endurance tests of metals*, Proc. Am Soc. Testing Materials, V.24, p. 476.

[7] Tomlinson G.A., (1927), *The rusting of steel surfaces in contact*, Proc. R. Soc. Lond. Ser A, V.115, pp. 472-483.

[8] Warlow-Davies E.J., (1941), *Fretting corrosion and fatigue strength*: Brief results of preliminary experiments, Proc. Instn mech Engrs, pp. 146,32.

[9] Mcdowell J.R. (1953), *in Fretting Corrosion*, STP V.144, pp.24-39, Philadelphia, PA, American Society for Testing and Materials.

[10] Fenner A.J and Field J.E (1960), *A study of the onset of fatigue damage due to fretting*, Proc. N.E. Coast Inst. Of Engs. And Shipbuilders, V.76, pp. 183

[11] Nitishhioka K., and Hirakawa, (1969), *Fundamental investigation of fretting fatigue*, part1. On the relative amplitudes of press-fitted axle assemblies, Bull. JSME, V. 11, pp. 437-445.

[12] Waterhouse R.B, (1972), *Fretting Corrosion*, Pergamon Press, USA.

[13] Mindlin, R.D., (1949*) Compliance of elastic bodies in contact*, Journal Application Mechanic V. 16, pp 259-268

[14] Johnson, K.L., (1955) *Surface interaction between elastically loaded bodies under tangential forces*, Proc. Roy. Soc., Serie A, V. 230, pp 531-548.

[15] Wright G.P., (1970), *Studies in fretting fatigue*, D. Phil Thesis, Oxford University.

[16] Bramhall R., (1973), *Studies in fretting fatigue*, D. Phil Thesis, Oxford University.

[17] Waterhouse R.B, (1981), *Fretting fatigue,* Applied Science Publishers Ltd., London.

[18] Hills D.A., and Nowell D., (1994), *Mechanics of fretting fatigue*, Kluwer Academic Publishers Dordrecht.

References

[19] Petiot C., Vincent L., Vang K. D., Moauche N., Foulquier J., Journet B., (1995), *An analysis of fretting-fatigue failure combined with numerical calculations to predict crack nucleation*, Wear, vol. 185, pp. 101–111.

[20] Szolwinski M., Farris T., (1996), *Mechanics of fretting fatigue crack formation,* Wear, vol. 198, pp. 93–107.

[21] Araújo, J.A. (2000). "*On the Initiation and Arrest of the Fretting Fatigue Cracks*". PhD thesis of the University of Oxford.

[22] Nowell D., (1988), *An analysis of fretting fatigue*, PhD thesis of Oxford University.

[23] Fouvry S., Kapsa P., Sidoroff F., Vincent L., (1998), *Identification of the characteristic length scale for fatigue cracking in fretting contacts*, J. Phys. IV France, vol. 8, pp. 159–166.

[24] Bernardo A. T., Araujo J. A., Mamiya E. N., (2004), *Proposition of a finite element based approach to compute the size effect in fretting fatigue*, Proceedings of the 4th International Symposium on Fretting Fatigue, Lyon.

[25] Ciavarella M., Macina G., (2003), *New results for the fretting-induced stress concentration on hertzian and flat rounded contacts,* International Journal of Mechanical Sciences, 2003, vol. 45, pp. 449–467.

[26] Abbasi F., Majzoobi G. H., (2018), *Effect of out-of-phase loading on fretting fatigue response of Al7075-T6 under cyclic normal loading using a new testing apparatus*, Engng. Fract. Mech. In press.

[27] Bhatti N. A., Wahab. M. A, (2017), *Finite element analysis of fretting fatigue under out of phase loading conditions*, Trib. Int. 109 pp. 552-62.

[28] Bhatti N. A., Pereira K.,. Wahab M. A, (2018), *A continuum mechanics approach for fretting fatigue under out of phase loading*, Trib. Int. 117 pp 39-51.

[29] Vingsbö O., Söderberg S., (1988), *On Fretting Maps*. Wear, 126, pp. 131-147.

[30] Rossino L., (2008), *Estudo do comportamento em fadiga por fretting da liga de AL 7050-T7451*, São Carlos-SP Thesis.

[31] Buciumeanu, M., (2009), *Prediction of fretting fatigue life.* PhD thesis of Minho University.

[32] Hertz, H. (1882) *Über die Berhrung fester elastischer Körper* , J. Reine Angew. Math. 29, pp. 156–171.

[33] Ciavarella, M., Macina, G. (2003), *New results for the fretting-induced stress concentration on Hertzian and flat rounded contacts*, International Journal of Mechanical Science, 45(3), pp. 449-467.

[34] Jonhson K., (1987), *Contact Mechanics*. Cambridge University Press.

[35] Cattaneo C., (1938) *Sul contatto di due corpi elastici: distribuzione locale degli sforzi.* Rend.Accad. Naz. Lincei, V. 27, n. 6, pp. 342–348.

References

[36] Muskhelishvili, (1953), *Some Basic problems of mathematical theory of elasticity*, Noordhoff, Groningen.

[37] Albert, W. A. J. (1837) *Über treibseile am Harz*. Archiv für Mineralogie, Geognosie, Bergbau und Hüttenkunde, V. 10, pp. 215–234.

[38] Poncelet, J. V. (1839) *Introduction à la mécanique industrielle, physique ou expérimentale*. Thiel.

[39] Campbel, F.C. (2008). *Elements of Metallurgy and Engineering Alloys*. ASM International.

[40] Schütz, W. (1996) *A history of fatigue. Engineering fracture mechanics*, V. 54, n. 2, pp. 263–300.

[41] Suresh, S. (1998) *Fatigue of materials*. Cambridge university press.

[42] Roebben, G. et al. (1996) *Mechanical fatigue in monolithic non-transforming ceramics*. Progress in materials science, v. 40, n. 4, pp. 265–331

[43] Hertzberg, R. W. (1996) *Deformation and fracture mechanics of engineering materials*. 122 Wiley.

[44] Manson, W. (1917) *Alternating Stress Experiments*. Proc. I. Mech. E., pp 121-196.

[45] Lagace, P.A. (1989) *Composite Materials: Fatigue and Fracture, Second Volume*. ASTM International

[46] Fei Cao, Pankaj Kumar, Mark Koopman, Chenluh Lin, Z.Zak Fang, K.S. Ravi Chandran. (2015), *Understanding competing fatigue mechanisms in powder metallurgy Ti-6Al-4V alloy: Role of crack initiation and duality of fatigue response*, Material Science and engineering, V.630 pp139-145.

[47] Zhiliang Pan, Timothy J.Rupert, (2014), *Damage nucleation from repeated dislocation absorption at a grain boundary*, Computational Material Science, V.93, pp 206-209.

[48] Yoshikazu Nakai, Sheiichirou Fukuharat and Kenji Ohnishit, (1997) *Observation of fatigue damage in structural steel by scanning atomic force microscopy*, International journal of Fatigue, V.19, pp 223-236

[49] Frost N.E, Phillips C.E, (1956), *Studies in the formation and propagation of cracks in fatigue specimens*, International Confrence on Fatigue of Metals, London, 520-526.

[50] Irwin, G.R, (1957), *Analysis of stresses and strains near the end of a crack traversing a plate*, Journal of Applied Mechanics vol 24, 361-364.

[51] Paris P.C., Erdogan F., (1963), *A critical analysis of crack propagation laws*, Trans. ASME, Series D, vol 85, 528-535.

[52] Wöhler, A., (1960). *Versuche über die festiykeit eisenbahnwagenuchsen*. Z. Bauwesen 10.

References

[53] Lanza, G. (1886), *Strength of Shafting Subject to Both Twisting and Bending, Transactions* ASME , Vol. 8, pp. 130-144.

[54] Gough, H. J. (1926) *The fatigue of metals*. E. Benn.

[55] Sumsel L., Lazzarin P, (2002), *A bi-parametric Wholer curve for high cycle multiaxial fatigue assessment*, Fatigue Fract. Eng. Mater Struct V. 25, pp. 63-68.

[56] McDiarmid D.L, (1991*), A general criterion for high cycle multiaxial fatigue failure*, Fatigue Fract. Eng. Mater. Struc. V.14, pp. 429-53.

[57] Dang Van K., (1973), *Sur la resistance a la fatigue des metaux*. Sci Tech L'armement V.47, pp. 429-53

[58] Socie DF., (1987), *Multiaxial fatigue ddamage models*, J. Eng. Mater. Techno. V.109, pp. 288-93

[59] Socie D.F., Shield T.W., (1984), *Mean stress effects in biaxial fatigue of Inconel 718*. J Eng. Mater. Tech. 106, 227-232.

[60] Fatemi A., Kurath P., (1988), *Multiaxial fatigue life prediction under the influence of mean stresses*, J. Eng. Mater. Tech., 380-388

[61] Susmel L., Tovo R., Lazzarin P., (2005), *The mean stress effect on the high-cycle fatigue strength from a multiaxial fatigue point of view*, Int. J. Fatigue V.27, pp. 928-43.

[62] Papadopoulos, I. (1998) *Critical Plane Approaches in High-Cycle Fatigue: on the Definition of the Amplitude and Mean Value of the Shear Stress Acting on the Critical Plane*. Fatigue & Fracture of Engineering Materials & Structures, V. 21, n. 3, pp. 269–285.

[63] Lemaitre, J.; Chaboche, J. L. (1985) *Mecanique des materiaux solides*. Dunod, Paris.

[64] Li, B.; Santos, J. L. T.; Freitas, M. De. A (2000) *unified numerical approach for multiaxial fatigue limit evaluation*. Mechanics of Structures and Machines, V. 28, pp. 85-103.

[65] Petrucci, G. (2015) *A critical assessment of methods for the determination of the shear stress amplitude in multiaxial fatigue, criteria belonging to critical plane class*. International Journal of Fatigue, V.74, pp. 119-131.

[66] Findley W.N., (1957), *Fatigue of metals under combinations of stresses*, Transaction of the American Society of Mechanical Engineers Vol. 19, pp. 1337-1348.

[67] Matake T., (1977), *An explanation on fatigue limit under combined stress*. Bulletin of Japan Society of Mechanical Engineers Vol 20, pp. 257-263.

[68] Matake T., (1980), *Fatigue strength of notched specimen under combined stress*, Bulletin of the Japan Society of Mechanical Engineers Vol 23, 623-629.

[69] Smith, KN.; Topper, T. H.; Watson, P. (1970) *A stress-strain function for the fatigue of metals (Stress-strain function for metal fatigue including mean stress effect)*. Journal of materials, V. 5, pp. 767–778.

References

[70] Szolwinski, M. P.; Farris, T. N. (1996) *Mechanics of fretting fatigue crack formation*. Wear, V. 198, n. 1, pp. 93–107.

[71] Sa, M.V.C, (2017) *Um estudo sobre o comportamento da liga AL 7050-T7451 na presença de entalhe e condições de carregamento multiaxiais*. University of brasilia Thesis.

[72] Fatemi, A.; Socie, D. F. (1988) A *Critical Plane Approach To Multiaxial Fatigue Damage Including Out of Phase Loading*. Fatigue & Fracture of Engineering Materials & Structures, V. 11, n. 3, pp. 149–165.

[73] Brown, M. W.; Miller, K. J. A. (1973) *Theory for Fatigue Failure under Multiaxial Stress-Strain Conditions*. Proceedings of the Institution of Mechanical Engineers, V. 187, n. 1, pp. 745–755.

[74] Susmel, L., (2009) *Multiaxial Notch Fatigue: from nominal to local stress-strain quantities*. Woodhead & CRC, Cambridge,UK.

[75] Susmel, L., Lazzarin, P. (2002) *A bi-parametric Wöhler curve for high cycle multiaxial fatigue assessment*, Fatigue Fract Eng Mater Struct, V. 25, pp. 63–78.

[76] Lazzarin, P., Susmel, L. (2003) *A stress-based method to predict lifetime under multiaxial fatigue loading,* Fatigue Fract Eng Mater Struct, V.26, pp. 1171–1187.

[77] Neuber, H. (1961) *Theory of notch stresses: principles for exact calculation of strength with reference to structural form and material*. USAEC Office of Technical Information. v. 4547.

[78] Peterson, R. E. (1959) *Notch sensitivity*. Metal fatigue, pp. 293–306.

[79] Taylor, D. (1999) *Geometrical effects in fatigue: a unifying theoretical model*. International Journal of Fatigue, V. 21, n. 5, pp. 413–420.

[80] Whitney, J. M.; Nuismer, R. J. (1974) *Stress fracture criteria for laminated composites containing stress concentrations*. Journal of composite materials, V. 8, n. 3, pp. 253–265.

[81] El Haddad M., Smith K., Topper T., (1979), *Prediction of non-propagating cracks*. Engineering Fracture Mechanics, V. 11, pp. 573-584

[82] Susmel, L.; Taylor, D., (2007), *A novel formulation of the theory of critical distances to estimate lifetime of notched components in the medium-cycle fatigue regime*. Fatigue and Fracture of Engineering Materials and Structures, V. 30, pp 567-581.

[83] Sa, M.V.C, Ferreira, J.L.A, Araujo, J.A. (2017), *Notched multiaxial fatigue of Al7050-T7451: on the need for an equivalent process zone size*. Frattura ed Integrita Strutturale, V. 41, pp. 90-97.

[84] Castro, F.C, Araujo, J.A., Pires, M.S.T, Susmel, L. (2015), *Estimation of fretting fatigue life using a multiaxial stress-based critical distance*, Frattura ed Integrita Strutturale, V.33, pp. 444-450.

References

[85] Rossino L.S., Castro F.C., Bose Filho W.W., Araujo J.A, (2009), *Issue on the mean stress effect in fretting fatigue of a 7050-T7451 Al Alloy posed by new experimental data*, International Journal of Fatigue V. 31, pp. 2041-2048

[86] Juvenal, G.M.A (2017) *Ensaios e avaliação da direção de iniciação de trinca sob condições de fretting.* University of Brasilia Thesis.

[87] ATME E 606-92 (1998) *Standard practice for strain-controlled fatigue testing.* ASTM International.

[88] ASTM International. *ASTM A 743 / A743M - 98A (1998) - Standard Specification for Castings, Iron-Chromium, Iron-Chromium-Nickel, Corrosion Resistent, for General Application*. West Conshohocken: ASTM International.

[89] Thibault D, Bocher P, Thomas M. (2011) *Reformed austenite transformation during fatigue crack propagation of 13Cr-4%NI stainless steel.* Materials Science and Engineering, V. 528(21): pp.6519-6526.

[90] Carrouge D, Bhadeshia HKDH, Woollin P. (2004) *Effect of d-ferrite on impact properties of supermartensitic stainless steel heat affected zones*. Science and Technology of Welding and Joining.; V. 9(5), pp. 377-389.

[91] Trudel A, Lévesque M, Brochu M. (2014) *Microstructural effects on the fatigue crack growth resistance of a stainless steel CA6NM weld. Engineering Fracture Mechanics.* V.115, pp.60-72.

[92] Espitia, L. Varela , C.E. Pinedo, A.P. Tschiptschin (2013) *Cavitation erosion resistance of low temperature plasma nitride martensitic stainless steel*. Wear pp. 449-456.

[93] Silva, B. L., Oliveira, J.L.A., F.Araújo, J.A (2009), *The effect of mean stress on the fatigue behavior of ASTM A743 CA6NM. Proceedings of the 20th International Congress on Mechanical Engineering*. Rio de Janeiro.

[94] Roberto C. Dante, (2016), *Handbook of Friction Materials and their applications*, Whoodhead Publishing.

[95] Italo, D.A. (2012) *Estudo sobre o domínio de aplicação de soluções analíticas para o problema de contato entre cilindros sob condições de fretting utilizando o Abaqus.* University of Brasilia Thesis.

[96] Doca T., Andrade Pires F.M., César Sá J.M.A., (2014), *A frictional mortar contact approach for the analysis of large inelastic deformation problems*. Int J Solids Struct V.51, pp. 1697–1715.

[97] Babai, S. Ghasemi-Ghalebahman, A., Hajighorbani, R. (2015) *A fatigue model for sensitive materials to non-proportional loadings.* International Journal of Fatigue, V.80, pp.266-277.

[98] De Souza, E. D. (2013), *Um modelo de análise de confiabilidade sob condições de falha por fadiga –Aplicação à pás de hidro turbinas kaplan.* University of Brasilia Thesis.

References

[99] Pereira, K., Wahab, M.A., (2017), *Fretting fatigue crack propagation lifetime prediction in cylindrical contact using an extended MTS criterion for non-proportional loading*. Tribology International V. 115 pp 525-534.

Appendix

$13 \, ^{+0.01}_{0}$

15 ± 0.01

60 ± 0.1

Ra 0,2

R70 ± 0.01

14	-	SAPATA 13x15 R70	Aluminio 7050	-	-
Item	Qde	Denominação	Material	Tratamento	Observações

Este desenho é de propriedade da UnB não podendo ser copiado ou reproduzido sem prévia autorização.

UnB	Faculdade de Tecnologia-FT	Departamento de Engenharia Mecânica-ENM

Laboratório de Ensaios Mecânicos

Testes de Fadiga sob condições de Fretting

TOLERÂNCIAS GERAIS						ESCALA	DATA	DESENHADOR	COORDENADOR
Dimensões	Fêmea	Macho	Largura	Rosca	Angulos	1:1	02/07/14	Miguel	Prof. Alex
<30	+ 0,2 + 0	+ 0 - 0,2	± 0,1	6 H	± 15'				
>30	H13	h13	Js13	6 g		A4	UnB	1011B14	